QUANTUM TRANSPORT IN TOPOLOGICAL SYSTEMS

YAP HAN HOE

(M.Sc. National University of Singapore)

A THESIS SUBMITTED FOR THE DEGREE OF

DOCTOR OF PHILOSOPHY

NUS GRADUATE SCHOOL FOR INTEGRATIVE SCIENCES AND ENGINEERING

NATIONAL UNIVERSITY OF SINGAPORE

2020

Supervisor:
Professor Gong Jiangbin and Wang Jian-Sheng

Examiners:
Associate Professor Zhang Chun
Assistant Professor Quek Su Ying
Professor Ma Tianxing, Beijing Normal University

Declaration

I hereby declare that this thesis is my original work and it has been written by me in its entirety. I have duly acknowledged all the sources of information which have been used in the thesis.

This thesis has also not been submitted for any degree in any university previously.

YAP Han Hoe

3 April 2020

Acknowledgments

First and foremost, I wish to address my gratitude to my supervisors, Professors Jiangbin Gong and Jian-Sheng Wang, for their invaluable guidance, constant support, kind words of encouragement, and very importantly, for showing me their passion for science that glows fervently as ever, even decades into their careers.

I would also like to thank Professor Yan Chen for his hospitality during my visit and for sharing with me his expertise in correlated systems. My sincere thanks go also to Gaomin, Linhu, Ching Hua, Jiebin, Patrick. Working with them had been very enjoyable and fruitful. I also benefited greatly from discussions with Derek, Ruofan, Zhun Yong, Dajian, Xizheng, Raditya, Mu Sen, Qi Fan, Hou Jie, Senmao, among many others.

The PhD journey wouldn't be as fulfilling without fellow friends Neo, Sim and Alex along the way. I wish also to thank Irene, Joan for their kind assistance in various administrative formalities. Last but not least, I am immensely grateful to my parents and family for their love and support, as well as Wang Qi for her faith in me.

Contents

Summary

Topological phases are states of matter characterized not by symmetry-breaking order parameters, but by topological numbers whose values remain invariant under smooth changes of the system parameters such as sample thickness and gate voltage. This robustness establishes topological matter as a candidate for next-generation devices such as low-dissipation spintronics components and far-infrared optical modulators. In this thesis, we study the quantum transport of various topological states. We first considered the Hofstadter model driven by a periodic field. Upon applying the Floquet sum rule, robust quantized conductance plateaus as large as $8e^2/h$ were found, and algorithms for the calculations of the local current and density of states were proposed. We then extended the method to tackle superconductivity to investigate the transport in several Floquet quantum anomalous Hall-topological superconductor heterostructures. Distinctive higher half-integer conductance plateaus were identified as signatures for the scattering between multiple chiral Majorana and Dirac modes. Next, we studied how topological phases as diverse as Weyl semimetals and second-order Chern insulators may arise from gapping a nodal loop semimetal. The corresponding transport signatures were also discussed. Lastly, motivated by the nonlinear response of graphene, we explored the possibility of high harmonic generation with nodal network semimetals, by means of the semiclassical Boltzmann equation.

List of Figures

List of Tables

Chapter 1

Introduction

Topology is the study of global properties that are insensitive to continuous deformation. If we have a Play-Doh of a coffee mug with a handle, we can remold it into a donut without having to tear the clay apart. Indeed, the genus, or the number of holes, of both objects is one. Hence, any two objects can be smoothly reshaped into one another so long as this number, a topological invariant, remains the same. From a sheet of graphene [1] to equatorial waves [2], the notion of topology is pervasive in nature. While its history traces back to defects in superfluid ^{3}He [3] and the Hall conductance in two-dimensional electron gas [4], topology has arguably been brought into the limelight of condensed matter physics following the advent of topological insulators (TI) [5, 6].

A striking consequence accompanying TIs is the existence of boundary modes guaranteed by topology. To get from a donut to a baguette, the dough will first have to be ripped apart. In this analogy, the donut represents a TI, the baguette corresponds to the vacuum, and the ripped dough the boundary modes separating these two breads. Often it is these boundary modes that are probed in experiments demonstrating nontrivial topologies of matter. Notable examples include tunneling spectroscopy [7] which probes the local density of states (LDOS), as well as multiterminal resistance measurements [8] which asserts the nonlocal transport properties of edge modes in quantum spin Hall insulators. Be it to design innovative devices or to demonstrate the bulk-edge correspondence, quantum transport is a key to decipher the intriguing properties of topological matter.

This thesis aims at investigating the transport of various topological phases. To that end, methods to study the transport of periodically driven systems are elaborated and extended to deal with heterostructures and superconductors. This allowed the identification of distinctive transport signatures of multiple Floquet topological edge modes. Insights on transport in heterostructures under periodic driving are also presented. For static models, an approach to generate different topological phases from a nodal loop semimetal is introduced, and the resulting transport signatures are examined. Lastly, the technological potential of topological metals with intricate linked and chained band-crossings are explored in connection to high harmonic generation.

In this chapter, we give an overview of the plethora of topological phases that has arguably spun off from the initial studies of TIs. Insulators bearing nontrivial topologies are first reviewed in Section 1.1.1, followed by the gapless states in Section 1.1.2 and the superconducting analogs in Section 1.1.3. The recurring theme of Floquet topological matter in this thesis is surveyed in Section 1.1.4, and the section on topological phases will be concluded by remarks on long-range entangled topological order in Section 1.1.5. As for transport, the semiclassical Boltzmann theory is discussed in Section 1.2.1. After a brief excursion into the Landauer-Büttiker formalism in Section 1.2.2, we present the non-equilibrium Green's function method in Section 1.2.3. Lastly, a synopsis of the thesis, presenting the motivations underlying each chapter, is given in Section 1.3.

1.1 Topological phases

1.1.1 Insulator

Preceding topological insulators is the quantum spin Hall (QSH) insulator, proposed by Kane and Mele [1] as a new state of matter that could arise in graphene and is topologically distinct from spin Hall insulators such as strained HgTe [9]. Specifically, Kane and Mele showed that the intrinsic spin-orbit interaction in a multivalley bandstructure yields two independent copies of the Haldane model for quantum anomalous Hall (QAH) insulators [10] with opposite TKNN invariants, which as a whole restore the time reversal symmetry (TRS) of the system. Shortly after, a $\mathbb{Z}_2$ topological invariant based on a Pfaffian constructed from the time reversal operator and the Bloch wavefunctions was proposed [11]. Considering the presence of inversion symmetry on top of TRS, Fu and Kane [12] gave a simpler expression for the $\mathbb{Z}_2$ index based on the parity of occupied bands at time-reversal invariant momenta (TRIM). The Fu-Kane invariant has become a practical tool for physicists to diagnose the topology of materials, even in apparently metallic systems such as the superconductor β-Bi_2Pd [13].

Apart from famously affirming the claim that all mathematics will find use in nature[1], topological insulator also owes its prominence to the dissipationless transport of its edge states. At the heart of such robust conduction channel lies the symmetry protecting the topology. For example, the propagation of QSH edge states will not be perturbed by weak interactions and disorder respecting TRS. This is because in presence of TRS, spin[2]-flipping transition cannot take place, and since the QSH edge states are

[1]"There is no branch of mathematics, however abstract, which may not some day be applied to phenomena of the real world."–Nikolai Ivanovich Lobachevsky, quoted in Mathematical Maxims and Minims (Raleigh N C 1988).

[2]Or pseudospin in the case of inversion symmetry breaking Rashba spin-orbit coupling in two-

spin-momentum locked, a spin-up, forward moving state will not be backscattered. The technological potential of such topologically protected transport amassed considerable funding. More than a decade after QSH was first realized [14], significant efforts continue to be dedicated to ameliorating its various aspects, such as the gap size and stability, in both monolayer materials such as bismuthene [7] and WTe_2 [15], as well as in the layered mineral jacutingaite [16]. The recent demonstration [17] of electric-field-induced toggling off of the topological edge states in ultrathin Na_3Bi via scanning electron microscope tip further marked an important milestone on the route towards topological field effect transistors.

In a laboratory, strong magnetic field can yield quantum Hall insulators with large Chern numbers, whose model Hamiltonian are studied in conjunction with a periodic driving field in Chapter 2. The insensitivity to microscopic details of the Hall resistance is of great interests for metrology [18], but its requirement of large magnetic fields is prohibitive for device applications. Historically, it was long known that ferromagnets can replace magnetic field to realize the anomalous Hall effect (AHE) [19]. Decades after Haldane's visionary work [10], interests on the quantized version of the AHE proliferated [20–22] with the advent of TIs. After the quantum anomalous Hall insulator (QAHI) was experimentally realized by magnetically doping TIs [23], the large Chern number proposals by structural distortion [24] and tuning sample thickness [25] soon followed. Interestingly, QAH state with Chern number larger than one was simulated in photonic crystals [26] as early as 2015 but only in 2018 does it find solid-state realizations in epitaxial $(Bi,Sb)_2Te_3$-CdSe magnetic TI-normal insulator superlattices [27] and more recently in the intrinsic magnetic TI $MnBi_2Te_4$ [28]. While the translation to marketable devices remains in its infancy, the emergence of QAH phase in multilayer graphene-

dimensional materials.

hexagonal boron nitride (hBN) moiré superlattices [29, 30] will surely fuel the already vigorous interests on this mother state of all topological insulators [31].

In 2011, Fu introduced the notion of topological crystalline insulator (TCI), in which one can dispense with spin-orbit coupling and still distinguish two topologically distinct classes of insulators, thanks to the discrete rotational symmetry in conjunction with TRS [32]. Soon afterwards, the rocksalt-structured SnTe was predicted [33] and verified [34] to be a TCI. The interplay between crystal symmetry and topology proves to have lasting impacts on the study of topological matter. An example can be given in the context of higher-order topology[3]. Shortly after this concept was proposed [35], elementary bismuth was shown to be a second-order TI [36]. Apparently contradicting the trivial Fu-Kane invariant $\nu = 1$, it was found that the trigonal symmetry of bismuth allows the topological index to be written as[4] $\nu = \nu^{(\pi)}\nu^{(\pi/3)}$, and that the second-order topology can be attributed to $\nu^{(\pi)} = \nu^{(\pi/3)} = -1$.

As mentioned, an attractive feature of topological edge modes is their robustness against disorder and interactions, which under ordinary circumstances are detrimental to device performances. In this sense, interesting counterexamples were given, where electron-electron [37] and electron-phonon [38] interactions were found to contribute positively to the trivial-to-topological phase transition. The finding of the so-called topological Anderson insulator is somewhat more serendipitous. While investigating the robustness against disorder of the Bernevig-Hughes-Zhang (BHZ) [39] model for the quantum spin Hall insulator (QSHI), Li et al [40] numerically discovered that disorder

[3]If one characterizes the band topology by the presence or absence of topological surface states, then an n-th order topology in d dimension means that the topological surface states exist on the $n-d$-dimensional surfaces of the system. In Chapter 3, an alternative perspective was proposed for a three-dimensional second-order Chern insulator, where it is considered as a descendant state from a nodal loop semimetal having a special gap

[4]Here, $\nu^{(\pi)}$ and $\nu^{(\pi/3)}$ are the parity of occupied eigenstates with $\hat{C}_3$ eigenvalues -1 and $\mathrm{e}^{\mathrm{i}\pi/3}$ respectively, whereas $\hat{C}_3$ is the threefold rotation operator.

can induce helical edge states with quantized conductance, even when the pristine sample is a trivial insulator. Groth et al [41] later analyzed the same model using an effective medium theory, where the effect of single-particle random disorder is embedded into a self-energy. They found that the self energy can conspire with the quadratic momentum dispersion in the BHZ model to induce band inversion, before Anderson transition occurs. This state was later realized in photonic crystals [42] and ultracold quantum gases [43].

1.1.2 Metal

That condensed matter systems admit eerily similar mathematical descriptions as certain high-energy physics phenomena is not a foreign concept [44, 45], but topological phases elevated this notion to newspaper columns [46, 47]. Often, such widespread attention can be accredited to the gapless states, be it on the boundary for insulators or in the bulk for metals. For instance, it was graphene [48, 49], a two-dimensional semimetal, that unlocked the door to (2+1)D relativistic physics which was once only of academic interests. Even though the spin-orbit gap in graphene is of the order of 10^{-3} meV [50] and therefore too small for the QSH effect, topology may still be considered as buried within it. This is because barring spin degeneracy, each fourfold degenerate Dirac point becomes twofold degenerate Weyl point with $\pm\pi$ Berry phases [51] and the two Weyl points behave like a monopole-antimonopole pair.

The observation above invoked the notion of Weyl semimetal, first popularized by Wan et al [52] when they studied the interplay between correlation and spin-orbit coupling in pyrochlore iridates using first-principle calculations. An antiferromagnetic ground state breaking TRS and harboring 24 twofold-degenerate band-crossing points was identified. At a time when interests on topological insulators expanded at a feverish rate, Wan et al realized the significance of the gapless states they found: In three dimensions, when spin degeneracy is lifted, the conduction and valence bands can touch without the need of symmetry, because it is generally possible to look for points $\boldsymbol{k}_0$ in a 3D BZ that can satisfy $d_i(\boldsymbol{k}_0) = 0$ for $i = 1, 2, 3$, where $\boldsymbol{d}(\boldsymbol{k}) \cdot \boldsymbol{\sigma}$ describes the low-energy Hamiltonian near any such possible $\boldsymbol{k}_0$, and $\boldsymbol{\sigma}$ are the three Pauli matrices describing the conduction and valence bands. Such band-crossings are called Weyl points. They act as sources or sinks of Berry curvature $\boldsymbol{\Omega}$, whose topological origins are evidenced by the quantized surface integrals of $\boldsymbol{\Omega}$ over a small sphere surrounding them, also known as the chirality or topological charge of Weyl nodes.

Equally compelling is the surface states of a Weyl semimetal. Consider a minimal Weyl semimetal with two Weyl points separated along the k_z direction, located at the Fermi energy. One may interpret the system as k_z-parameterized Chern insulators, whose mass gaps are a function of k_z. Then the Weyl points may be understood as topological phase transition points, partitioning the BZ into two regions, one in which the slices of insulators have zero Chern number, and the other non-zero. Under open boundary conditions (OBC), e.g. with (x, k_y, k_z), the surface at $x = 0$ will then exhibit a so-called Fermi arc, which arises from the chiral edge states of the Chern insulator slices pinned at the Fermi energy. Unlike ordinary 3D metals, Fermi arcs are not closed Fermi surfaces, but emanate and terminate at the two Weyl points projected on the surface BZ. In presence of a strong magnetic field, the bulk chiral Landau levels in a Weyl semimetal thin slab connect the open Fermi arcs on both surfaces, constituting a "Weyl orbit" which yields thickness-dependent quantum oscillations [53] and enables IQHE in 3D [54].

Incidentally, the aforementioned transport evidences were found not in a Weyl but a Dirac semimetal Cd_3As_2 [55, 56]. The simplest occurrence of the Dirac semimetal phase is at the critical point between a TI and a trivial insulator. Alternatively, as alluded to previously, a Dirac semimetal may be understood as two copies of Weyl semimetals with, e.g. opposite spins stacked together. Dirac semimetals from such simple constructions either require fine-tuning of parameters, or are unstable against SOC. Evidently, the Dirac semimetals that are experimentally realized belong to a more robust category. For example, the Dirac points in Cd_3As_2 are enforced by band inversion and protected by fourfold rotational symmetry [57]. A myriad of semimetal phases were subsequently predicted and verified, spurring considerable interests because of their violations of Lorentz symmetry which are only possible in condensed-matter but not high-energy physics. These include the type-II Weyl fermion in $MoTe_2$ (where electron and hole pockets coexist with Weyl points due to a tilting term) [58], three-component fermion in MoP (where two degenerate bands cross with a single nondegenerate band due to band inversion, protected by threefold rotational and mirror symmetries) [59], multifold fermion in AlPt (where the effective Hamiltonian near the symmetry-protected crossings, $h(\boldsymbol{k}) = \boldsymbol{k} \cdot \boldsymbol{S}$, has spin-1 or spin-$\frac{3}{2}$ generalizations for the spin operator $\boldsymbol{S}$, due to structural chirality) [60].

Another intriguing possibility with topological semimetal is where the band-crossings form not zero-dimensional points, but higher-dimensional objects such as 1D line (loops) [61] or 2D surfaces [62]. Fang et al [63] elaborated on the simplest nodal loop semimetal, $h(\boldsymbol{k}) = (m - \boldsymbol{k}^2)\sigma_x + k_z\sigma_z$, which constitutes the basis of Chapter 3 where we study how various topological states can be understood as its descendants. Although any 1D closed loop enclosing the band-crossings yields a π Berry phase, when the radius parameter m is decreased, the nodal loop shrinks and disappears. Hence, unlike Weyl points, such nodal loop can be annihilated locally under a continuous change of parameters. The authors of Ref. [63] were able to define a $\mathbb{Z}_2$ monopole charge from an orthogonal matrix given by the overlaps between occupied bands on the northern and southern hemispheres of a sphere enclosing the nodal loop. They then distinguished two types of nodal loops, one which can be annihilated locally, and another which cannot. Interestingly, regardless of the triviality of this $\mathbb{Z}_2$ monopole charge, both types of nodal loops exhibit weakly dispersive "drumhead" surface states [64], which are theoretically found to host unusual correlation effects, such as a ferromagnetic ordering coupling both bulk and surface excitations, with a quantum critical exponent different from conventional 2D or 3D metals [65]. Furthermore, their semimetallicity and nonvanishing density of states signal a propensity towards excitonic instability [66], which may explain the mass enhancement observed experimentally in ZrSiS [67]. A wealth of systematic studies ensued [68], and the concept was pushed to the extreme with the notions of double-helix semimetal [69] and Hopf-link semimetals [70], with the latter having found realization in the Heusler compound Co_2MnGa [71], whose propensity for nonlinear transport was argued to be advantageous for high harmonic generation in Chapter 5.

1.1.3 Superconductor

Long before the birth of TIs, studying the textures of order parameters in superfluid ^{3}He, physicists applied homotopy theory, i.e. the theory of continuous mappings, to classify and exhaust all possible topological defects in that quantum liquid [72, 73]. In 2001, chiral p-wave superconductors were investigated and topological properties such as half-quantum vortices and Majorana fermions were theoretically predicted [74]. Pursuing Wen's notion of topological order [75], it was found that, when viewed as charged superfluids with dynamic electromagnetism, gapped superconductors are topologically ordered [76].

The history of topological phases is therefore intimately intertwined with superfluidity and superconductivity. Considering also the parallels between the mean-field Hamiltonians of superconductors and that of non-interacting insulators, it is natural that most if not all topological phases, gapped or otherwise, are rapidly generalized to the case of superconductors.

Doped Bi_2Se_3 is one of the most important superconductors which closely resemble a TI. Soon after it was synthesized and shown to be superconducting [77], Fu and Berg [78] enumerated the possible pairings in $Cu_xBi_2Se_3$ on symmetry grounds. Analytically solving the linearized gap equation based on a multi-orbital Hubbard interaction model, they charted a phase diagram and singled out a pairing that exhibits TRS $\mathbb{Z}_2$ topology[5] like its parent compound Bi_2Se_3. On the experimental front, nuclear magnetic resonance (NMR) Knight shift measurements identified nematic superconductivity[6] in $Cu_xBi_2Se_3$ [83], which was also found in Nb-doped Bi_2Se_3 via torque magnetometry [84]. These findings narrowed down the superconducting pairing of doped TIs to the two-dimensional irreducible representation E_u of the point group D_{3h}, which has odd parity and is fully gapped, serving as a telltale sign for nontrivial $\mathbb{Z}_2$ topological superconductivity.

Prior to the dramatic turn of event in March 2019, strontium ruthenate (Sr_2RuO_4) was once hailed as a candidate for odd-parity chiral $p_x \pm \mathrm{i}p_y$ superconductivity[7] [86]. In

[5] A superconductor in three dimension with TRS $\mathcal{T}^2 = -1$ and particle-hole symmetry (PHS) $\mathcal{C}^2 = +1$ belongs to class DIII in the Altland-Zirnbauer (AZ) [79] classification, and is characterized by $n \in \mathbb{Z}$. The $\nu \in \mathbb{Z}_2$ invariant for doped Bi_2Se_3 is related to the $\mathbb{Z}$ invariant by $\nu = n \mod 2$ [78].

[6] In the context of topological superconductivity, by which is meant the superconductivity in doped TI [80], nematicity refers to the breaking of the threefold rotational symmetry in the superconducting state. Note however that theoretical analysis [81] argued for the case of vestigial nematicity, i.e. there exists a transition temperature T_n below which the threefold symmetry is broken, and $T_n > T_c$ where T_c is the superconducting transition temperature. This is also backed by thermal and magnetization measurements of Nb-doped Bi_2Se_3 [82].

[7] A preprint appeared in March 2019 [85], experimentally pointing out that the invariant NMR Knight shift upon entering the superconducting state of Sr_2RuO_4, a 1998 experimental finding which

the simplest case of a single band, such superconducting pairing gives a Chern number $|C| = 1$, which corresponds to an orbital angular momentum of $\pm\hbar$ carried by the superfluid. While the jury is out now on the pairing symmetry of Sr_2RuO_4, there has been attempts at engineering solid-state systems to realize superconductors with the much sought after topology from a chiral $p_x \pm \mathrm{i}p_y$ pairing. The first proposal was given by Fu and Kane [87], in which they studied the surface of a 3D TI proximitized by an s-wave superconductor. The spin-momentum-locked texture of the single Dirac cone synergizes with the ordinary s-wave pairing to yield a helical p-wave pairing, similar to the B phase of superfluid ^{3}He [88]. When a TRS-breaking Zeeman field is further considered, the resulting system harbors chiral Majorana edge states on the interfaces between the insulator and superconductor.

While the pioneering proposal of superconductor-TI-magnet heterostructure has yet to see the light of day, it paved the way for further studies [89, 90] both in thin films [91] and nanowires [92], which ultimately outpaced their predecessor in terms of experimental realizations [93, 94]. The realization of chiral Majorana fermions in magnetic TI thin film and superconductor heterostructures is particularly relevant to Chapter 4 of this thesis. It originated from the following consideration [95]: Just like magnetization can undo the band inversion of the spin-down band in the BHZ model to yield a QAHI with spin-up band [21], superconductivity can gap out half the degree of freedom in a complex Dirac edge fermion, turning a QWZ model [20] expressed in Nambu spinor basis into a chiral topological superconductor (TSC) with a single Majorana edge mode. Soon to follow were detailed analysis of the scattering between Dirac and Majorana modes in a QAHI-TSC-QAHI heterostructure [96], as well as

was widely taken to be an evidence for triplet superconductivity, was due to the heating effect due to the laser pulse. When the laser power was decreased to ensure that it would not destroy the superconducting state, a pronounced drop in the Knight shift measurements below T_c was observed.

model studies based on magnetically doped TI [91], culminating in the groundbreaking experiment in 2017 [94].

Attributing the half-quantized conductance plateaus at magnetization switching transition of the QAHI-TSC-QAHI heterostructure to chiral Majorana fermions is by no means unequivocal. A bone of contention is that at the magnetization reversal, the sample is highly inhomogeneous, populated by domains of a different Chern number. Casting the problem as a classical percolation model [97], it was found that $e^2/(2h)$ conductance plateaus can arise from QAH chiral edge states alone as a consequence of dephasing due to the random domains [98, 99]. A preprint with experimental results on QAHI-SC heterostructures by another group also appeared recently [100]. The authors reported (i) transparent electrical contacts between various magnetic TI films and the superconductor Nb, (ii) the observations that the two-terminal conductance above the upper critical field of Nb show no difference compared with its values at zero magnetic field, as well as (iii) the presence of an additional Nb strip gives a conductance of $e^2/(3h)$. With the above, it was argued that the superconducting portion shunted the QAH samples, so that the half-quantized plateaus are simply results of two QAH insulators connected in series, instead of the exotic chiral Majorana fermion. Further investigations, such as the proposal of ferromagnetically proximitizing an s-wave superconductor with Dirac-cone surface states [101], will be needed on this twisty route towards two-dimensional chiral topological superconductors.

Synthetic topological superconductors in one dimension are based on the Kitaev model [102], the celebrated superconducting analog to the Su-Schrieffer-Heeger (SSH) model [103] for semiconducting polymers. Motivated by the possibility of performing quantum information processing resilient against decoherence, Kitaev studied a one-dimensional superconducting wire with spin-triplet p-wave pairing and focused on a single spin sector. By working in the so-called Majorana basis[8], he found that the Hamiltonian can be specified by a real antisymmetric matrix A. Based on the Pfaffian of A, a $\mathbb{Z}_2$ invariant was given as a fermion parity signaling the presence or absence of an unpaired electron in the superconducting ground state. While the requirements [90] of (i) large spin-orbit coupling for band inversion, (ii) TRS breaking for spin-polarization, (iii) superconductivity for Bogoliubov quasiparticles, seemed too daunting to ask for in one go, physicists were able to circumvent the difficulties by proximitizing InSb nanowires with NbTiN contacts under a Zeeman field [93]. This approach was refined significantly, yielding a robust quantized Majorana plateau of $2e^2/h$ in 2018 [104]. An alternative solution where ferromagnetic Fe atomic chains are fabricated on top of strongly spin-orbit-coupled superconductor Pb was also realized [105], allowing high spatial and spectral resolution by STM of in-gap states, which can be evidence for Majorana zero modes.

The topological superconductors discussed thus far suffer from complications on the interfaces that inevitably accompany heterostructure engineering. Parallel to this development is the hunt for nontrivial topology in single-material superconductors, sometimes known as "connate topological superconductors" [106]. Surprisingly, superconductors with multiple topological features such as band inversion, Dirac semimetal [107] are often found in iron-based superconductors, which have rather high transition temperatures, e.g. $T_c = 14.5\,\mathrm{K}$ for $FeTe_{0.55}Se_{0.45}$ [108]. With systematic studies on the zero-bias peaks at vortex cores strongly favoring the presence of Majorana bound states [109], the future of this "amazing new field for Majorana" [110] with iron-based superconductors

[8]If the spin-polarized electron creation and annihilation operators at site i are denoted by $c_i^{(\dagger)}$, then the Majorana basis is obtained as a linear transformation given by $\gamma_{iA} = (c_i + c_i^\dagger)/2$ and $\gamma_{iB} = \mathrm{i}(c_i - c_i^\dagger)/2$.

is looking bright ahead.

1.1.4 Floquet topological phases

With the salient prospect of tuning material properties in a non-invasive manner, Floquet engineering has emerged as a promising research direction in solid-state and cold-atom physics [111]. With relevance to topological states of matter, it was realized as early as 2008 [112] that the double-kicked rotor, a prototypical quantum chaos model readily solved by the Floquet theorem, exhibits Hofstadter's butterfly, a hallmark of the integer quantum Hall effect (IQHE). Shortly after, the possibility to exploit the time reversal symmetry breaking property of circularly polarized light to realize the IQHE in graphene without magnetic field was investigated [113]. In a similar vein, following the realization of the quantum spin Hall state in HgTe/CdTe quantum well [14], the use of microwave irradiation to induce topological band inversion was proposed in 2011 [114]. These works arguably marked the birth of Floquet topological matter, a vibrant research area recently reviewed in [115].

Experimentally, angle-resolved photoemission spectroscopy demonstrated the apperance of Floquet-Bloch bands gapped from the surface Dirac cone of a TI in 2013 [116]. Another breakthrough followed a year later, when scientists demonstrated the coherent manipulations by light of valleys in monolayer transition metal dichalcogenides [117, 118]. The recent observation of transient anomalous Hall effect in graphene driven by femtosecond pulses [119] will decidedly propel the experimental advances after a hiatus of four years.

1.1.5 Topological order

Since the tunability of solid state materials is often no match for synthetic systems such as photonic crystal [120], acoustic metamaterial [121], and electrical circuit [122], the field of artificial topological phases has taken on a life of its own. With research agendas spanning from the identification of classical effective theories that mimic the Schrödinger equation [123], to the meticulous designs yielding nontrivial topology on classical tight-binding models [124], synthetic topological matter is an all-encompassing scientific venture that challenges both our creativity and mastery of the subject.

On the other hand, the simulatibility of topological phases by classical systems and the polynomial complexity of diagonalizing a topological bandstructure suggest that truly quantum-mechanical properties are absent in topological phases. Physically, such topological phases can be smoothly deformed into product states in the absence of the relevant symmetries. Therefore, they are widely known as SPT states, which stands for symmetry protected topological[9] [127] states. The models studied in this thesis belong by and large to the SPT phases[10]. The wider classes of topological phases, i.e. those with long-range entanglement, known as topological orders, such as the $\mathbb{Z}_2$ spin liquid [128] and the Laughlin states [129], are beyond the scopes of this thesis.

[9]Depending on one's definitions of "topological", SPT may also stand for symmetry protected trivial [125, 126], e.g. if one requires the topological property to be robust against *any* local perturbations.

[10]A notable exception is the class A topological phases according to the AZ classification, to which belong the IQHE and Chern/QAH insulators. By definition, class A has no internal symmetries, yet may be characterized by different Chern numbers. Furthermore, topological metals are gapless and hence strictly speaking not SPT phases.

1.2 Quantum transport

1.2.1 Semiclassical equations of motion

Originally written down for a kinetic theory of gas [130], the Boltzmann transport equation (BTE) was adopted by Lorentz, Sommerfeld and Bloch for the study of metallic conduction [131]. Let $f(\boldsymbol{r}, \boldsymbol{k}, t)$ be the distribution function of a single particle in a phase space with canonical variables $(\boldsymbol{r}, \boldsymbol{k})$ at time t. The Boltzmann equation is given by:

$$\frac{\partial f(\boldsymbol{r},\boldsymbol{k},t)}{\partial t} + \dot{\boldsymbol{k}} \cdot \frac{\partial f(\boldsymbol{r},\boldsymbol{k},t)}{\partial \boldsymbol{k}} + \dot{\boldsymbol{r}} \cdot \frac{\partial f(\boldsymbol{r},\boldsymbol{k},t)}{\partial \boldsymbol{r}} = I[f], \tag{1.1}$$

where $I[f]$ is the collision integral describing the change in the distribution function due to different scattering processes, e.g. electron-electron, electron-phonon, electron-impurity. It is complemented by a set of dynamical laws on position $\boldsymbol{r}$ and momentum (wavevector) $\boldsymbol{k}$, governed by the semiclassical equations of motion [132]:

$$\begin{aligned} \dot{\boldsymbol{r}} &= \frac{\partial \epsilon(\boldsymbol{k})}{\hbar \partial \boldsymbol{k}} - \dot{\boldsymbol{k}} \times \boldsymbol{\Omega}(\boldsymbol{k}), \\ \dot{\boldsymbol{k}} &= \frac{-e}{\hbar}\boldsymbol{E} + \frac{-e}{\hbar}\dot{\boldsymbol{r}} \times \boldsymbol{B} \end{aligned} \tag{1.2}$$

where $\epsilon(\boldsymbol{k}) = \epsilon_0(\boldsymbol{k}) - \boldsymbol{m}(\boldsymbol{k}) \cdot \boldsymbol{B}$ is the band dispersion ($\epsilon_0(\boldsymbol{k})$ satisfies $H(\boldsymbol{k})|u(\boldsymbol{k})\rangle = \epsilon_0(\boldsymbol{k})|u(\boldsymbol{k})\rangle$) corrected by the orbital magnetic moment $\boldsymbol{m}(\boldsymbol{k})$, which is given by:

$$\boldsymbol{m}(\boldsymbol{k}) = \frac{-e}{2\hbar}\mathrm{Im}\left[\left\langle \frac{\partial u(\boldsymbol{k})}{\partial \boldsymbol{k}} \right| \times (H(\boldsymbol{k}) - \epsilon_0(\boldsymbol{k})) \left| \frac{\partial u(\boldsymbol{k})}{\partial \boldsymbol{k}} \right\rangle\right], \tag{1.3}$$

the electron charge is $-e < 0$, the electric and magnetic field denoted by $\boldsymbol{E}$ and $\boldsymbol{B}$, and the Berry curvature

$$\boldsymbol{\Omega}(\boldsymbol{k}) = \mathrm{i}\left\langle \frac{\partial u(\boldsymbol{k})}{\partial \boldsymbol{k}} \right| \times \left| \frac{\partial u(\boldsymbol{k})}{\partial \boldsymbol{k}} \right\rangle. \tag{1.4}$$

The above equations of motion can be derived from a Lagrangian formalism [132]. Together with the BTE (Equation 1.1), they serve as the starting point for understanding various magnetotransport phenomena and Hall effects. Equation 1.2 can be simplified:

$$\begin{aligned}\dot{\boldsymbol{r}} &= \left[\frac{\partial\epsilon(\boldsymbol{k})}{\hbar\partial\boldsymbol{k}} - \frac{-e}{\hbar}\boldsymbol{E}\times\boldsymbol{\Omega}(\boldsymbol{k}) - \frac{-e}{\hbar}\left(\frac{\partial\epsilon(\boldsymbol{k})}{\hbar\partial\boldsymbol{k}}\cdot\boldsymbol{\Omega}(\boldsymbol{k})\right)\boldsymbol{B}\right]\Bigg/\left[1-\frac{-e}{\hbar}(\boldsymbol{B}\cdot\boldsymbol{\Omega}(\boldsymbol{k}))\right],\\ \dot{\boldsymbol{k}} &= \left[\frac{-e}{\hbar}\boldsymbol{E} + \frac{-e}{\hbar}\frac{\partial\epsilon(\boldsymbol{k})}{\hbar\partial\boldsymbol{k}}\times\boldsymbol{B} - \left(\frac{-e}{\hbar}\right)^2(\boldsymbol{E}\cdot\boldsymbol{B})\boldsymbol{\Omega}(\boldsymbol{k})\right]\Bigg/\left[1-\frac{-e}{\hbar}(\boldsymbol{B}\cdot\boldsymbol{\Omega}(\boldsymbol{k}))\right].\end{aligned} \tag{1.5}$$

Typically, one is interested in time-independent, translational-invariant transport with weak electric field. Furthermore, if the scattering processes are of secondary importance, one often invokes the relaxation time approximation, in which the collision integral $I[f]$ is taken to be:

$$I[f] = \frac{f_0(\boldsymbol{k}) - f(\boldsymbol{k})}{\tau}, \tag{1.6}$$

where τ is the relaxation time, assumed to be independent of $\boldsymbol{k}$, and $f_0(\boldsymbol{k})$ is the equilibrium Fermi distribution. Thus the BTE (Equation 1.1) simplifies:

$$\dot{\boldsymbol{k}}\cdot\frac{\partial f(\boldsymbol{k})}{\partial\boldsymbol{k}} = \frac{f_0(\boldsymbol{k}) - f(\boldsymbol{k})}{\tau(\boldsymbol{k})}, \tag{1.7}$$

which can be solved iteratively. With the above ingredients, one then proceeds to compute transport properties, e.g. electrical current, by[11]:

$$\boldsymbol{j} = -e\int\frac{\mathrm{d}^3\boldsymbol{k}}{(2\pi)^3}\left[1-\frac{-e}{\hbar}(\boldsymbol{B}\cdot\boldsymbol{\Omega}(\boldsymbol{k}))\right]\dot{\boldsymbol{r}}f(\boldsymbol{k}). \tag{1.8}$$

The presence of the factor $\left[1-\frac{-e}{\hbar}(\boldsymbol{B}\cdot\boldsymbol{\Omega}(\boldsymbol{k}))\right]$ is a consequence of the Liouville's theorem, mandating the conservation of phase-space volume under time evolution [133]. To linear

[11] In spatially nonuniform systems (where $\frac{\partial}{\partial\boldsymbol{r}}\neq 0$), there is a contribution of magnetization current $\frac{\partial}{\partial\boldsymbol{r}}\times[\boldsymbol{m}(\boldsymbol{k})f(\boldsymbol{r},\boldsymbol{k})]$ in the integrand [132].

order in the external fields $(\boldsymbol{E}, \boldsymbol{B})$, some insights can already be drawn:

$$\begin{aligned}
\boldsymbol{j} = &\left[e^2\tau \int \frac{\mathrm{d}^3\boldsymbol{k}}{(2\pi)^3}\left(-\frac{\partial f_0(\varepsilon(\boldsymbol{k}))}{\partial\varepsilon}\right)\boldsymbol{v}_{\boldsymbol{k}}\boldsymbol{v}_{\boldsymbol{k}}\right]\cdot\boldsymbol{E} \\
&+\left[\frac{e^2}{\hbar}\int \frac{\mathrm{d}^3\boldsymbol{k}}{(2\pi)^3} f_0(\varepsilon(\boldsymbol{k}))\boldsymbol{\Omega}_{\boldsymbol{k}}\right]\times\boldsymbol{E} \\
&+\left[-\frac{e^2}{\hbar}\int \frac{\mathrm{d}^3\boldsymbol{k}}{(2\pi)^3} f_0(\varepsilon(\boldsymbol{k}))\boldsymbol{v}_{\boldsymbol{k}}\cdot\boldsymbol{\Omega}_{\boldsymbol{k}}\right]\boldsymbol{B} \\
&+\left[-\frac{-e}{\hbar}\int \frac{\mathrm{d}^3\boldsymbol{k}}{(2\pi)^3} f_0(\varepsilon(\boldsymbol{k}))\frac{\partial\boldsymbol{m}_{\boldsymbol{k}}}{\partial\boldsymbol{k}}\right]\cdot\boldsymbol{B},
\end{aligned} \tag{1.9}$$

where the first two lines feature the dissipative linear conductivity, and nondissipative Hall conductivity, the third and fourth lines involve chiral magnetic effect and contribution to electrical current from orbital magnetic moment. Thorough order-by-order expansions were performed in Ref. [134] for magneto-optical properties and in Ref. [135] for the chiral charge pumping, both in Weyl metals. In the absence of magnetic field and Berry curvature, Equation 1.5 simplifies substantially. In Chapter 5, we work within this framework to study the nonlinear electrical response of a real Hamiltonian describing the bandstructures of Co_2MnGa [136], hosting peculiar nodal chains and Hopf links.

One may also construct microscopic models for the collision integral $I[f]$ or the relaxation time τ to evaluate transport properties. For instance, the BTE was employed to study the impacts of charged impurities and electron density on the electrical transport in graphene [137]. In fact, even interference can be accounted for, as demonstrated by the Altshuler-Aronov corrections on the conductivity of disordered conductors with strong electron-electron interactions [138]. With advances in sample fabrications paving the way for electron hydrodynamics[12] [141], the BTE remains the starting point to

[12] In the regime of electron hydrodynamics, the system is described by conserved quantities obeying Navier-Stokes-like equations [139], and boundary scattering (instead of lattice vibration) is the dominant momentum-relaxing mechanism [140].

explore this transport regime.

1.2.2 Landauer-Büttiker formalism

The Landauer approach [142] posits that electronic transport is dictated by the phase coherence of electrons. It is particularly pertinent to samples whose dimensions are much smaller than the electron mean free path at low temperatures and low electron density. In this approach, the wave character of electrons is manifest, since the calculation of conductance is formulated as a scattering problem with the Schrödinger equation, which for most sample geometries admit the same form as the Helmholtz equation for electromagnetic propagation in a waveguide. The transport is nonlocal, in that the conductance is independent of the length of the sample, unlike an Ohmic conductor which dissipates locally. When scattering is absent, e.g. in sufficiently clean or small samples, electrons enter the ballistic regime, where each mode contributes a conductance quantum of $2e^2/h$ with spin degeneracy.

Nontrivial band topology can also provide ballistic channels to make way for electrical conduction along edges. To demonstrate such nondissipative transport, it is customary to add voltage probes to the sample to verify zero voltage drops on the edges. The voltage probes were once thought to couple weakly to the sample, possibly because they draw no current. In a seminal work [143] discussing the symmetry of electrical conduction in a four-terminal sample, Büttiker provided grounds for treating the voltage probes and current leads on equal footing. The Landauer aspect of coherent transport combined with the Büttiker perspective on voltage probe constitute the Landauer-Büttiker formalism. It is the basis of interpretations and predictions of a multiterminal mesoscopic transport experiment: The current entering terminal p is given by:

$$I_p = \sum_q G_{p\leftarrow q}(V_q - V_p), \tag{1.10}$$

where V_q denotes the voltage at terminal q, the sum is over all terminals, and $G_{p\leftarrow q}$ is the transmission from terminal q to terminal p. The Landauer-Büttiker formalism is especially handy for topological matter which features quantized conductances insensitive to symmetry-preserving scatterings $G_{p\leftarrow q}$ in Equation 1.10. It was applied to make predictions on the detection of dissipative nonchiral edge modes [144], and to interpret transport measurements of edge modes along the domain walls of magnetic TIs [145]. Variants are proposed for spinful systems such as the QSHI [8].

As an aside, that the voltage probes play the same role as the source and drain is not exclusive to electronic systems. In fluctuation electrodynamics [146], it was shown in Ref. [147], that given two three-dimensional slabs terminated with surfaces which also radiate thermally, the same Landauer-Büttiker form as Equation 1.10 holds for the energy balance, with the surfaces mirroring the voltage probes in the electronic case.

1.2.3 Non-equilibrium Green's functions

While its history traces back to the 1960s by great minds like Kadanoff and Baym [148], five decades on, the non-equilibrium Green's function (NEGF) method remains the state-of-the-art technique for transport calculations. For non-interacting systems, NEGF is used for large-scale simulations [149] such as the QSHI bismuthene on SiC substrate, with a sample of 10^6 lattice sites, each with four internel degrees of freedom. For interacting systems, NEGF can deal with the interaction terms diagrammatically, such as in a driven polaronic system where a single electron level is coupled to a single phonon mode in an Anderson-Holstein model under a time-periodic driving field [150].

NEGF has also been extended to electron-phonon systems to study thermoelectricity [151] and to electron-photon systems to study thermal radiation [152]. With relevance to the latter, we note another strength of NEGF: Its field-theoretic approach allows a transparent understanding *à la* Hubbard-Stratonovich [153], that in thermal radiation, the Coulomb interactions in a purely electronic system play the same role as an auxiliary photon field in an electron-photon system [154], as demonstrated in Ref. [155]. In terms of device modeling, NEGF is about as first-principle as it gets when interfaced with density-functional calculations [156], finding use in fields as diverse as molecular electronics [157] and spintronics [158].

In this thesis, the "plain vanilla" NEGF for tight-binding Hamiltonians is used in Chapter 3 to identify distinct transport signatures from different descendant topological states from a 3D nodal loop. An extension of NEGF dealing with time-periodic driving fields will be needed in Chapter 2 to study Floquet quantum Hall insulators. In Chapter 4 it is further promoted to address superconducting samples where additional scattering processes such as local and crossed Andreev reflections are possible. Here, we give a derivation for the electrical current in a two-terminal setting, closely following the canon by Haug and Jauho [159]. The relevant generalizations will be presented in the respective chapters.

Consider a sample with Hamiltonian

$$\mathcal{H}_C = \sum_i \epsilon_i c_i^\dagger c_i, \tag{1.11}$$

and a left lead with Hamiltonian

$$\mathcal{H}_L = \sum_j \epsilon_j a_j^\dagger a_j, \tag{1.12}$$

and analogously for the right lead (with electron operators $b^{(\dagger)}$). The sample-lead coupling is given by:

$$\mathcal{V}_{LC} = \sum_{m,n} V_{mn} a_m^\dagger c_n + \text{h.c.} \tag{1.13}$$

The total Hamiltonian is thus given by:

$$\mathcal{H} = \mathcal{H}_L + \mathcal{V}_{LC} + \mathcal{H}_C + \mathcal{V}_{CR} + \mathcal{H}_R. \tag{1.14}$$

The current is defined as the rate of change of the number of particles in the left lead:

$$\begin{aligned} I_L &= -\left\langle \frac{\mathrm{d}\mathcal{N}_L}{\mathrm{d}t} \right\rangle \\ &= -\frac{1}{\mathrm{i}\hbar} \left\langle [\mathcal{N}_L, \mathcal{V}_{LC}] \right\rangle \\ &= -\frac{1}{\mathrm{i}\hbar} \sum_{j,i} \left\langle V_{ji} a_j^\dagger c_i - V_{ji}^* c_i^\dagger a_j \right\rangle \end{aligned} \tag{1.15}$$

where the minus sign in the first line indicates that a current leaving the left reservoir is taken to have a positive sign. Consider now the mixed Green's function in contour time[13,14]

$$\boldsymbol{G}_{a_j c_i^\dagger}(\tau) = -\frac{\mathrm{i}}{\hbar} \left\langle \mathcal{T}_\tau a_j(\tau) c_i^\dagger \right\rangle, \tag{1.17}$$

where $\tau = (t, \sigma)$ is a contour time, with $t \in \mathbb{R}$ and $\sigma = \pm$ denoting the upper or lower contour branch, $\mathcal{T}_\tau$ indicates contour ordering. $\mathcal{T}_\tau$ arranges operators with later contour

[13] The contour-time Green's function differs from its ground-state and equilibrium counterparts by the choice of contour, as discussed pedagogically in the treatise of Stefanucci and van Leeuwen [160]. For practical purposes one can treat it as a variable with respect to which differentiation and integration are possible. A Green's function with two contour times succintly encodes four possible functions when resolved to real times, depending on the branches of the two contour times:

$$\boldsymbol{G}(\tau_1, \tau_2) = \begin{cases} G^t(t_1, t_2), & \text{if } \sigma_1 = \sigma_2 = +, \\ G^{\bar{t}}(t_1, t_2), & \text{if } \sigma_1 = \sigma_2 = -, \\ G^<(t_1, t_2), & \text{if } \sigma_1 = +, \sigma_2 = -, \\ G^>(t_1, t_2), & \text{if } \sigma_1 = -, \sigma_2 = +. \end{cases} \tag{1.16}$$

[14] In this chapter, contour-time Green's functions will be written in bold, and real-time Green's functions in normal font.

times to the left, incurring a minus sign for each swap, if the operators are fermionic. With the help of this Green's function, the current (Equation 1.15) can be expressed as:

$$I_L = -2\mathrm{Re}\sum_{j,i} V_{ij}^* \int_{-\infty}^{\infty} \frac{\mathrm{d}\omega}{2\pi} G^<_{a_j c_i^\dagger}(\omega), \tag{1.18}$$

where $[\dots]^<$ means taking the lesser component of a contour-time Green's function. The equation of motion of Equation 1.17 is:

$$\mathrm{i}\hbar\frac{\partial}{\partial\tau}\boldsymbol{G}_{a_j c_i^\dagger}(\tau) = \sum_l \left(-\frac{\mathrm{i}}{\hbar}\right) V_{jl}\left\langle \mathcal{T}_\tau c_l(\tau) c_i^\dagger\right\rangle + \epsilon_j\left(-\frac{\mathrm{i}}{\hbar}\right)\left\langle \mathcal{T}_\tau a_j(\tau) c_i^\dagger\right\rangle, \tag{1.19}$$

or

$$\left(\mathrm{i}\hbar\frac{\partial}{\partial\tau} - \epsilon_j\right)\boldsymbol{G}_{a_j c_i^\dagger}(\tau) = \sum_l V_{jl}\boldsymbol{G}_{li}(\tau), \tag{1.20}$$

where the device Green's function is:

$$\boldsymbol{G}_{li}(\tau) = -\frac{\mathrm{i}}{\hbar}\left\langle \mathcal{T}_\tau c_l(\tau) c_i^\dagger\right\rangle. \tag{1.21}$$

Equation 1.20 can be formally solved as follows:

$$\boldsymbol{G}_{a_j c_i^\dagger}(\tau) = \sum_l \int_C \mathrm{d}\tau' \boldsymbol{g}_{a_j a_j^\dagger}(\tau-\tau') V_{jl}\boldsymbol{G}_{li}(\tau'), \tag{1.22}$$

so that the current expression, Equation 1.18 becomes:

$$I_L = -2\mathrm{Re}\int_{-\infty}^{\infty}\frac{\mathrm{d}\omega}{2\pi}\sum_{j,l,i}\left[\int_C \mathrm{d}\tau'\left(V_{ij}^*\boldsymbol{g}_{a_j a_j^\dagger}(\tau-\tau')V_{jl}\right)\boldsymbol{G}_{li}(\tau')\right]^<(\omega) \tag{1.23}$$

Now we introduce the left lead self energy:

$$[\boldsymbol{\Sigma}_L]_{il}(\tau) = \sum_j V_{ij}^*\boldsymbol{g}_{a_j a_j^\dagger}(\tau)V_{jl}^*. \tag{1.24}$$

The Langreth rule [159] for the lesser projection of the following type of product

$$\boldsymbol{C}(\tau_1,\tau_2) = \int_C \mathrm{d}\tau_3 \boldsymbol{A}(\tau_1,\tau_3)\boldsymbol{B}(\tau_3,\tau_2) \tag{1.25}$$

is given by:

$$C^{<}(t_1,t_2)=\int_{-\infty}^{\infty}\mathrm{d}t_3\left[A^{<}(t_1,t_3)B^{a}(t_3,t_2)+A^{r}(t_1,t_3)B^{<}(t_3,t_2)\right], \tag{1.26}$$

where the retarded $(\dots)^r$ and advanced $(\cdots)^a$ components of a contour Green's function A are defined as:

$$\begin{aligned} A^{r}(t_1,t_2)&=A^{t}(t_1,t_2)-A^{<}(t_1,t_2),\\ A^{a}(t_1,t_2)&=A^{t}(t_1,t_2)-A^{>}(t_1,t_2). \end{aligned} \tag{1.27}$$

Resuming the derivation for current, from Equation 1.23 one finds:

$$I_L=-2\mathrm{Re}\int_{-\infty}^{\infty}\frac{\mathrm{d}\omega}{2\pi}\mathrm{Tr}\left[\Sigma_L^{<}(\omega)G^{a}(\omega)+\Sigma_L^{r}(\omega)G^{<}(\omega)\right], \tag{1.28}$$

where the summation over modes in the sample and leads are written as a trace by considering the device Green's function and self energy as matrices. The device Green's function satisfies the following EOM:

$$\begin{aligned} \mathrm{i}\hbar\frac{\partial}{\partial\tau}\boldsymbol{G}_{ij}(\tau)=\delta_{ij}\boldsymbol{\delta}(\tau)+\int_C \mathrm{d}\tau'\sum_k[\boldsymbol{\Sigma}_L+\boldsymbol{\Sigma}_R]_{ik}(\tau-\tau')\left(-\frac{\mathrm{i}}{\hbar}\right)\langle\mathcal{T}_\tau c_k(\tau')c_j\rangle\\ +\sum_k[\mathcal{H}_C]_{ik}\boldsymbol{G}_{kj}(\tau). \end{aligned} \tag{1.29}$$

From the definition of a retarded Green's function, Equation 1.27, as well as the action of the contour-ordering operator $\mathcal{T}_\tau$, one obtains:

$$G_{ij}^{r}(t)=-\frac{\mathrm{i}}{\hbar}\theta(t)\left\langle\{c_i(t),c_j^\dagger\}\right\rangle, \tag{1.30}$$

where $\{\cdot,\cdot\}$ is the anticommutator. Then it can be shown that an equation similar to Equation 1.29 holds for the retarded component. Below we suppress the mode indices i,j to not encumber notation. Going to the Fourier domain ω, one finds:

$$G^{r/a}(\omega)=[\hbar\omega\pm\mathrm{i}\eta-H_C-\{\Sigma_L^{r/a}(\omega)+\Sigma_R^{r/a}(\omega)\}]^{-1}, \tag{1.31}$$

where $\eta \to 0^+$ is a positive infinitesimal number. The above can also be cast in the form of a Dyson equation:

$$G^{r/a}(\omega) = g^{r/a}(\omega) + g^{r/a}(\omega)\Sigma^{r/a}(\omega)G^{r/a}(\omega), \tag{1.32}$$

where $g^{r/a}$ is the retarded/advanced component of the sample Green's function (i.e. the Green's function for $\mathcal{H}_C$ alone).

Next, it is convenient to expand the real part, and to invoke cyclicity of matrix products under trace:

$$\begin{aligned} 2\mathrm{ReTr}\left[\Sigma_L^<(\omega)G^a(\omega) + \Sigma_L^r(\omega)G^<(\omega)\right] = \mathrm{Tr}[&\Sigma_L^<(\omega)G^a(\omega) - \Sigma_L^<(\omega)G^r(\omega) \\ &+ \Sigma_L^r(\omega)G^<(\omega) - \Sigma_L^a(\omega)G^<(\omega)] \end{aligned} \tag{1.33}$$

where we used the identities

$$\begin{aligned} (A^<)^\dagger(\omega) &= -A^<(\omega), \\ (A^r)^\dagger(\omega) &= A^a(\omega), \end{aligned} \tag{1.34}$$

as can be shown for $\boldsymbol{A} = \boldsymbol{G}, \boldsymbol{\Sigma}$ from their definitions. Furthermore, from Equation 1.27, one has:

$$A^r(\omega) - A^a(\omega) = A^>(\omega) - A^<(\omega). \tag{1.35}$$

Hence, the integrand in the current expression is simplified:

$$\begin{aligned} &2\mathrm{ReTr}\left[\Sigma_L^<(\omega)G^a(\omega) + \Sigma_L^r(\omega)G^<(\omega)\right] \\ &= \mathrm{Tr}[\{\Sigma_L^>(\omega) - \Sigma_L^<(\omega)\}G^<(\omega) + \Sigma_L^<(\omega)\{G^<(\omega) - G^>(\omega)\}] \\ &= \mathrm{Tr}[\Sigma_L^>(\omega)G^<(\omega) - \Sigma_L^<(\omega)G^>(\omega)]. \end{aligned} \tag{1.36}$$

Now the missing ingredient for the current integrand, Equation 1.36, is the lesser component of the device Green's function. For that, we first derive a Dyson equation for the contour device Green's function from the EOM, Equation 1.29:

$$\boldsymbol{G}(\tau) = \boldsymbol{g}(\tau) + \int_C \mathrm{d}\tau'' \boldsymbol{g}(\tau - \tau'') \int_C \mathrm{d}\tau' \boldsymbol{\Sigma}(\tau'' - \tau')\boldsymbol{G}(\tau'). \tag{1.37}$$

From the above, by iterating the Langreth rule for the lesser components (Equation 1.26) twice, one finds:

$$G^< = g^< + g^r * \Sigma^< * G^a + g^< * \Sigma^a * G^a + g^r * \Sigma^r * G^<, \tag{1.38}$$

where $*$ denotes a convolution in real time:

$$(A * B)(t) = \int_{-\infty}^{\infty} \mathrm{d}t' A(t - t')B(t'). \tag{1.39}$$

By the convolution theorem, from Equation 1.38 one finds an equivalent equation in frequency:

$$G^< = g^< + g^r \Sigma^< G^a + g^< \Sigma^a G^a + g^r \Sigma^r G^<, \tag{1.40}$$

where the frequency dependences $\cdot(\omega)$ are suppressed. Reorganizing the terms, one finds:

$$(1 - g^r \Sigma^r)G^< = g^<(1 + \Sigma^a G^a) + g^r \Sigma^< G^a. \tag{1.41}$$

Using the Dyson equation for the retarded and advanced components, Equation 1.27, we have:

$$g^r (G^r)^{-1} G^< = g^< (g^a)^{-1} G^a + g^r \Sigma^< G^a. \tag{1.42}$$

The resulting equation:

$$G^< = G^r (g^r)^{-1} g^< (g^a)^{-1} G^a + G^r \Sigma^< G^a \tag{1.43}$$

is known as the Keldysh equation. For noninteracting systems, the lesser sample Green's function can be calculated:

$$g^< = (g^a - g^r)f, \tag{1.44}$$

where f is the equilibrium Fermi function. Thus, the first term in the RHS of Equation 1.43 becomes:

$$\begin{aligned}
G^r(g^r)^{-1}g^<(g^a)^{-1}G^a &= G^r(g^r)^{-1}\Big[(g^a-g^r)f\Big](g^a)^{-1}G^a \\
&= G^r\Big[\{(g^r)^{-1}-(g^a)^{-1}\}f\Big]G^a \\
&= G^r\Big[\{(\hbar\omega+\mathrm{i}\eta-\mathcal{H}_C)-(\hbar\omega-\mathrm{i}\eta-\mathcal{H}_C)\}f\Big]G^a \\
&= G^r(2\mathrm{i}\eta)G^a,
\end{aligned} \tag{1.45}$$

which vanishes since $\eta \to 0^+$ is infinitesimal. Now define the lead spectral functions, $\Gamma_{L/R} = \mathrm{i}(\Sigma^r_{L/R} - \Sigma^a_{L/R})$. With the advanced and lesser device Green's functions, we can pursue the derivation from Equation 1.36 for the current:

$$\begin{aligned}
\mathrm{Tr}[\Sigma^>_L G^< - \Sigma^<_L G^>] &= \mathrm{Tr}\left[\Sigma^>_L\Big\{G^r(\Sigma^<_L+\Sigma^<_R)G^a\Big\} - \Sigma^<_L\Big\{G^r(\Sigma^>_L+\Sigma^>_R)G^a\Big\}\right] \\
&= \mathrm{Tr}\left[\Gamma_L G^r \Gamma_R G^a\right]\{(1-f_L)f_R - f_L(1-f_R)\} \\
&= \mathrm{Tr}\left[\Gamma_L G^r \Gamma_R G^a\right]\{f_R - f_L\}.
\end{aligned} \tag{1.46}$$

We have thus reproduced the derivations of Meir and Wingreen [161] to recover the Landauer formula for current in a noninteracting sample:

$$I_L = -e\int_{-\infty}^{\infty}\frac{\mathrm{d}\omega}{2\pi}\mathrm{Tr}\left[G^r(\omega)\Gamma_R(\omega)G^a(\omega)\Gamma_L(\omega)\right]\{f_L(\omega)-f_R(\omega)\}. \tag{1.47}$$

Lastly, we note that the equally popular boundary-condition-matching approach was shown for the electronic case [162] and for the phononic case [163] to be consistent with the NEGF method, reminiscent of the Fisher-Lee relation [164] connecting the transmission from scattering matrix and the conductance from Kubo formula.

1.3 Thesis Synopsis

In this section, we give an outline of the thesis by providing contexts from which each chapter sprung.

Studying the topology of the Floquet bands in a ratchet-accelerator model [165], Ho and Gong found system parameters yielding a Chern number as large as 32 with merely three bands. A periodically quenched Haldane model for QAHI was analyzed in Ref. [166], and Chern numbers that are substantially larger than their static counterparts were found. Importantly, this topological invariant corresponds to the number of robust edge states in OBC. Thus, to extend the tradition of designing useful quantum control protocols, we embarked on a study of the transport properties of periodically driven topological systems, which is presented in Chapter 2.

In Ref. [167], Li et al realized that the minimal model for 3D TI [168] may be interpreted as a $\mathcal{PT}$-symmetric (a combination of inversion and time-reversal symmetries) nodal loop semimetal gapped by two anticommuting Dirac matrices serving as mass terms. Such a model TI may be called a chiral insulator, since as a whole its Hamiltonian obeys $SH(\boldsymbol{k})S^{-1} = -H(\boldsymbol{k})$, where S is identified as the chiral symmetry operator. In Chapter 3, we ask: What if more general mass terms, such as those breaking the chiral symmetry, are allowed? Various topological phases that may be considered as descendants of a 3D nodal loop semimetal are examined, as well as their corresponding transport signatures.

The ingenious application of Floquet driving to restore time reversal symmetry in one-dimensional Kitaev chains, thereby generating multiple Majorana zero modes[15] was proposed in Ref. [169]. Together with the groundbreaking observation of half-quantized conductance plateaus as a signature for chiral Majorana edge modes (CMEM) in QAH-TSC-QAH heterostructures [94], we were motivated to investigate whether

[15]The Kitaev model for spinless p-wave superconductors belongs to class D and is marked by an absence of TRS. In one dimension, the topological invariant is the Majorana number $\mathcal{M} \in \mathbb{Z}_2$, representing the presence or absence of an unpaired electron in the superconducting ground state. In the presence of TRS, this model is promoted to class BDI, whose topological invariant $n \in \mathbb{Z}$ counts the number of Majorana zero modes.

similar transport signatures could arise in presence of multiple CMEMs induced by Floquet driving. Our findings are presented in Chapter 4.

One of the multitude of applications of graphene is as a nonlinear optical material [170] for purposes such as parametric amplification and frequency doubling [171]. As the Dirac cone physics is identical in both graphene and the surface of a TI, proposals on TI-based optoelectronic devices, such as terahertz detectors and transparent electrodes were similarly put forward [172]. Hence it is interesting to explore whether the same technological promises hold, upon generalizing the concept of nodal point semimetals to loops and even chains or links. Such a study is performed using the Boltzmann equation in Chapter 5.

Chapter 2

Computational study of the two-terminal transport of Floquet quantum Hall insulators

2.1 Preliminaries

The long-time behavior of a quantum system subject to time-periodic modulations is governed by its Floquet states. With recourse to the Floquet theorem, one may compute the Floquet bandstructures in analogy to the case when periodic drive is absent. While the Floquet bandstructures under periodic boundary conditions may look superficially similar to an equilibrium spectrum, the impression that periodically driven systems are not much different from their static counterparts is deceptive. For example, as evidenced by the works of Ho and Gong [165], a Floquet system in the form of a quantum ratchet-accelerator model may exhibit Chern numbers that are significantly larger than those carefully designed in a static Haldane model for the quantum anomalous Hall effect [173]. Equally impressive is the amendment of bulk-edge correspondence [174].

Historically, Floquet topological phases were first anticipated in the context of quantum chaos and nonlinear dynamics, back in 1990 [175] and more recently in 2008 [112]. It took off in the condensed matter community, arguably following the works on photoinduced Hall effect in graphene [113] and on light-induced band inversion in HgTe/CdTe quantum wells [114]. A wide variety of Floquet topological matter has since then been proposed, from Weyl [176] to Hopf-link [177] semimetals, from insulator [178] to superconductor [169].

As alluded to in the first paragraph, an attractive feature of Floquet topological phases is their large topological invariants in the case of class A under the Altland-Zirnbauer classification [179]. This suggests that one may harness the unusually large number of edge state channels in Floquet topological matter to realize multiple lanes of "electron superhighway", to quote S. C. Zhang's vision for electronics of the future [180]. At the time of publication, few studies have investigated this possibility in the context of two-terminal transport, even though in the community of molecular electronics, many efforts have been devoted to the study of driven transport at the nanoscale [181–183]. Conventionally, it is known and lauded aesthetically that in the quantum Hall regime, the Hall conductance is quantized at plateaus of e^2/h times the number of chiral edge modes lying between Landau levels [184]. For a similar sample subject to time-periodic drive, since the system is described stroboscopically by the Floquet operator and its eigenstates, its transport properties may deviate significantly from the case without periodic modulation. For instance, consider electromagnetic waves as the driving field. Since electrons interact with these waves, they can absorb or emit photons, thereby accessing states that would not have been possible without the periodic drive. Hence, the two-terminal transport in Floquet topological matter is not exactly straightforward.

With regards to the potential of Floquet topological matter as useful devices, we can formulate the following questions: (i) Are Floquet topological phases indeed useful in achieving tunable, appreciable and robust conductance? (ii) How is the Floquet edge state conductance related to the symmetry and the topological invariants of the system? (iii) Is the conductance of Floquet edge states quantized? If not, why and when? Answers to these questions are of both theoretical and experimental interest.

In the literature, several studies had been dedicated to the edge state transport in time-reversal symmetric Floquet topological states. It was shown in Ref. [185] that the DC conductance of a Floquet topological insulator is not quantized because it is not directly linked to the topological invariants of the full Floquet bands. By employing a Floquet sum rule proposed in the context of one-dimensional topological superconductor [186], a way to recover quantized condutance in Floquet quantum spin Hall insulators was found [187]. This was further confirmed in a simple Floquet Chern insulator model [188]. Introducing a scattering matrix invariant, the authors in Ref. [189] studied the conductance of Floquet edge states, which only assumes integer values. Generalizing the boundary-condition matching approach to Floquet systems, the conductance scaling in an irradiated graphene nanoribbon was investigated in Ref. [190]. The effects of reservoirs on the transport of Floquet edge states were also explored in Ref. [191]. With these interesting findings as well as the lack of experimental realization of Floquet topological states in electronic systems, the transport properties of Floquet edge states clearly deserve additional studies, in the hope that on-demand, non-invasive tuning of electronic transport may one day be realized.

In this chapter, we apply the Keldysh nonequilibrium Green's function (NEGF) approach and the recursive Floquet-Green's function method to explore the transport of Floquet edge states in a two-terminal setup. As a concrete example, we choose the Hofstadter lattice model in view of its rich topological bands even without periodic drive, but our methods and conclusions are completely general. We consider such a sample subject to a harmonic driving and coupled to two metallic leads. The effective magnetic flux in the Hofstadter model breaks time reversal symmetry, giving rise to a model system even simpler than the driven quantum spin Hall system studied in Refs. [187]. We present intriguing transport properties for different types of Floquet edge states by calculating the DC conductance, DC profile and time-averaged local density of states (LDOS) in both pristine and disordered samples. In particular, we answer affirmatively that Floquet edge states indeed give rise to robust and tunable edge current as we change the system parameters and the driving field. Remarkably, quantized DC conductance as large as $8e^2/h$ is found in certain parameter regimes after applying the Floquet sum rule. Possible experimental observations of such theoretical observations are also discussed. Furthermore, we evaluate the robustness of three types of Floquet edge states by introducing disorder and defects to the driven sample. It is found that co-propagating Floquet chiral edge states are more robust than counter-propagating and symmetry-restricted ones. Finally, we study how the transport property of Floquet edge modes is modified if the leads have a finite bandwidth. All these detailed results constitute a necessary guide towards the potential use of Floquet topological matter in designing novel transport devices.

This chapter is organized as follows. In Section 2.2 we outline the theoretical framework and introduce the transport quantities studied in this work. Readers not interested in technical details may skip this section. In Section 2.5, we introduce the harmonically-driven Hofstadter model in a two-terminal setup. In Section 2.7, we analyze the two-terminal transport via Floquet edge states in pristine samples. In Section 2.8, we study the response of Floquet edge states to disorder and defect. We then investigate the implications of finite-bandwidth leads on the quantization of DC conductance in Section 2.9.

2.2 Theory

In this section, we first outline the Keldysh framework for quantum transport. Next, we introduce the Floquet representation of Green's functions [192]. This then leads us to three transport quantities: (1) DC conductance, (2) local DC profile, and (3) time-averaged local density of states (T-LDOS), which we use to investigate edge state transport. Lastly, we discuss how to compute the Floquet-Green's functions of interest. Throughout this chapter, we use the following notations: $\mathcal{T}$ for the period of the driving field, $\Omega = 2\pi/\mathcal{T}$ for the driving frequency, ϵ for quasienergy and E for energy. Note that although the central system is under periodic driving and hence what matters is its quasienergy, the leads are however not driven and its energy must be specified in a theory of quantum transport.

2.2.1 Transport within the Keldysh-NEGF framework

The Hamiltonian of noninteracting electrons in a tight-binding lattice subject to driving fields is written as $H(t) = \sum_{\langle i,j\rangle} J_{ij}(t) c_i^\dagger c_j + \text{h.c.}$, where $c_i^\dagger$ (c_i) is the creation (annihilation) operator on lattice site i, $J_{ij}(t)$ is a time-dependent hopping amplitude or onsite potential, and $\langle i,j\rangle$ indicates summation over nearest neighbors. Following Ref. [193], we consider the driving fields to be switched on in the distant past, but not switched off throughout the duration of our interest. In a two-terminal device, the central system $H(t)$ is connected to a left and a right electronic lead, which are kept in equilibrium with chemical potentials μ_L and μ_R, respectively. The electronic current from the left lead to the central system is given by $I^L(t) = e\langle \mathrm{d}N_L/\mathrm{d}t\rangle$, where the electron charge is $-e$, and N_L is the particle number operator of the left lead. The explicit time dependence of the current is due to the driving field applied to the center.

In the Keldysh-NEGF framework, the contour-ordered Green's function is defined as $G(\tau,\tau') = -\frac{\mathrm{i}}{\hbar}\left\langle \mathcal{T} c(\tau) c^\dagger(\tau') \right\rangle$, where $\mathcal{T}$ orders contour time variables τ, τ' along the Keldysh contour [159, 194]. Following the Meir-Wingreen prescription, the expression of the current reads [193]:

$$I^L(t) = e\left[\int_{\mathcal{C}} \mathrm{Tr}_\Lambda\Big[\Sigma_L(\tau,\tilde{\tau})G(\tilde{\tau},\tau')\Big]\mathrm{d}\tilde{\tau}\right]^<_{\tau=\tau'\mapsto t} + \text{c.c.}, \tag{2.1}$$

where $\Sigma_L(\tau,\tilde{\tau})$ is the self-energy of the left lead. $\int_{\mathcal{C}} \mathrm{d}\tilde{\tau}\cdots$ is an integral over the Keldysh contour [194]. $\mathrm{Tr}_\Lambda[\cdots]$ is a trace over the central lattice system. $[\cdots]^<$ means resolving a contour function into its lesser component, which can be done following the Langreth's rules [159]. The notation $\cdots|_{\tau=\tau'\mapsto t}$ means setting the two contour times τ, τ' at equal time t.

2.2.2 Green's functions in Floquet representation

Under a periodic driving field, even if a periodic steady state is achieved, the Green's functions no longer depend on just one single variable (i.e. the relative time). Thus both the average and relative time need to be treated. Consider the Wigner representation [195] of a two-point correlation function $g(t,t')$, given by $\bar{g}(T=\frac{t+t'}{2}, \tau = t-t') = g(t,t')$, where T (τ) is the average (relative) time variable. Its Floquet representation is obtained by the following transformation [195]:

$$\boldsymbol{g}_{mn}(E) = \frac{1}{\mathfrak{T}}\int_0^{\mathfrak{T}} \mathrm{d}T\ \mathrm{e}^{\mathrm{i}(m-n)\Omega t}\int_{\mathbb{R}} \mathrm{d}\tau\ \mathrm{e}^{\mathrm{i}(E+\frac{m+n}{2}\hbar\Omega)\frac{\tau}{\hbar}}\ \bar{g}(T,\tau). \tag{2.2}$$

The Floquet representation is especially convenient when manipulating convolution integrals, because it turns them into (infinite) matrix product [195]:

$$[\int_{\mathbb{R}} \mathrm{d}\tilde{t}\ f(t,\tilde{t})g(\tilde{t},t')]_{mn}(E) = \sum_{k\in\mathbb{Z}} \boldsymbol{f}_{mk}(E)\boldsymbol{g}_{kn}(E). \tag{2.3}$$

The following convention for Floquet representation of Green's functions will be used. If the spatial components of a Green's function in the Floquet representation need to be specified, we write $\boldsymbol{g}_{(i,j;m,n)}(E)$, with the first two indices of the subscript $(i, j; m, n)$ corresponding to lattice site indices i, j, and the last two indices m, n corresponding to Floquet indices as in Equation 2.2.

2.3 Transport quantities

If a periodic steady state is attained, the correlation functions in the Wigner representation are also periodic with respect to the average time T, i.e., $\bar{g}(T, \tau) = \bar{g}(T + \mathfrak{T}, \tau)$. This allows for the Floquet decomposition and it can be shown that the DC component of the current is given by [183, 196]:

$$I_{\mathrm{DC}}^{L} = e \int_{\mathbb{R}} \frac{\mathrm{d}E}{2\pi\hbar} \sum_{k\in\mathbb{Z}} \left\{ \mathrm{Tr}_{\Lambda} \left[\boldsymbol{G}_{k0}^{r} \boldsymbol{\Gamma}_{00}^{L} \boldsymbol{G}_{0k}^{a} \boldsymbol{\Gamma}_{kk}^{R} \right] f^{L} - \mathrm{Tr}_{\Lambda} \left[\boldsymbol{G}_{k0}^{r} \boldsymbol{\Gamma}_{00}^{R} \boldsymbol{G}_{0k}^{a} \boldsymbol{\Gamma}_{kk}^{L} \right] f^{R} \right\}, \tag{2.4}$$

where $\boldsymbol{G}_{k0}^{r(a)}(E)$ is the Floquet representation of retarded (advanced) Green's functions $G^{r(a)}(t, t')$, defined by:

$$\begin{aligned} G^{r}(t, t') &= -\frac{\mathrm{i}}{\hbar}\theta\left(t - t'\right) \left\langle \{c(t), c^{\dagger}(t')\} \right\rangle, \\ G^{a}(t, t') &= \frac{\mathrm{i}}{\hbar}\theta\left(t' - t\right) \left\langle \{c(t), c^{\dagger}(t')\} \right\rangle, \end{aligned} \tag{2.5}$$

and $f^{L(R)}$ is the Fermi function of the left (right) lead. $\Gamma^{L(R)} = \mathrm{i}\{\Sigma_{L(R)}^{r} - [\Sigma_{L(R)}^{r}]^{\dagger}\}$ is the level width function of the left (right) lead, with $\boldsymbol{\Gamma}_{kk}^{L(R)}$ being the corresponding matrix in the Floquet representation. In general, all these functions depend explicitly on energy E.

2.3.1 DC Conductance

We now define the *transmission coefficient* at an energy E from the left to right lead as $T_{LR}(E) = \sum_{k\in\mathbb{Z}} \mathrm{Tr}_{\Lambda} \left[\boldsymbol{G}_{k0}^{r} \boldsymbol{\Gamma}_{00}^{L} \boldsymbol{G}_{0k}^{a} \boldsymbol{\Gamma}_{kk}^{R} \right]$ [and analogously for $T_{RL}(E)$ with $L \leftrightarrow R$].

When a bias voltage V is applied between the two reservoirs, the chemical potentials of the leads become $\mu_{L/R} = \mu_0 \pm eV/2$. At zero temperature and to first order in V, one can linearize the Fermi function as: $f_{L/R}(E) = \theta(\mu_0 \pm eV/2 - E) \approx \theta(\mu_0 - E) \mp \delta(\mu_0 - E)eV/2$. Under this condition, Equation 2.4 simplifies to:

$$I^L_{\mathrm{DC}} = e \int_{-\infty}^{\mu_0} \frac{\mathrm{d}E}{2\pi\hbar} \left[T_{LR}(E) - T_{RL}(E)\right] + \frac{e^2}{h} \frac{T_{LR}(\mu_0) + T_{RL}(\mu_0)}{2} V. \tag{2.6}$$

When there is an inversion symmetry between left and right leads (which is the case in all our numerical calculations), we have $T_{LR}(E) = T_{RL}(E)$ [185]. Under this condition, the DC conductance $\mathrm{d}I^L_{\mathrm{DC}}/\mathrm{d}V$ *at a given energy* E is simply given by e^2/h times the transmission coefficient $T(E) = T_{LR}(E) = T_{RL}(E)$, which reads

$$T(E) = \sum_{k \in \mathbb{Z}} \mathrm{Tr}_\Lambda \left[\boldsymbol{G}^r_{k0}(E) \boldsymbol{\Gamma}^L_{00}(E) \boldsymbol{G}^a_{0k}(E) \boldsymbol{\Gamma}^R_{kk}(E) \right]. \tag{2.7}$$

2.3.2 Local DC Profile

The Heisenberg equation for the particle number operator $n_i = c_i^\dagger c_i$ at lattice site i is given by [1]:

$$\begin{aligned} \langle \dot{n}_i(t) \rangle = {} & J_{i+\hat{\mathbf{x}},i}(t) G^<_{i,i+\hat{\mathbf{x}}}(t,t) + J_{i-\hat{\mathbf{x}},i}(t) G^<_{i,i-\hat{\mathbf{x}}}(t,t) \\ & + J_{i+\hat{\mathbf{y}},i}(t) G^<_{i,i+\hat{\mathbf{y}}}(t,t) + J_{i-\hat{\mathbf{y}},i}(t) G^<_{i,i-\hat{\mathbf{y}}}(t,t) + \text{c.c.}, \end{aligned} \tag{2.8}$$

which is similar to the case without a driving field [197], apart from the explicit time dependences of the hopping terms. We may then define the local current from site $i + \hat{\mathbf{x}}$ to site i as: $I_{i \leftarrow i+\hat{\mathbf{x}}}(t) = J_{i+\hat{\mathbf{x}},i}(t) G^<_{i,i+\hat{\mathbf{x}}}(t,t) + \text{c.c.} = -I_{i+\hat{\mathbf{x}} \leftarrow i}$, and analogously for all

[1] This equation (continuity equation for local particle number) remains valid on the edges of the central system, with the understanding that, on the top and bottom edges, Dirichlet boundary condition is used, e.g.: $J_{i,i-\hat{\mathbf{y}}} = 0$ if $y_i = 0$, whereas on the left and right edges, scattering boundary condition is used, e.g.: $J_{i,i-\hat{\mathbf{x}}} = t_x$ (the left-center coupling) and $G^<_{i,i-\hat{\mathbf{x}}} = -\frac{\mathrm{i}}{\hbar} \langle a^\dagger_{i-\hat{\mathbf{x}}} c_i \rangle$ if $x_i = 0$, where we recall that $a^\dagger$ is the creation operator of the left lead.

other neighbors of i. From this one defines the time-averaged local current vector:

$$\vec{I}_i = \frac{1}{\mathcal{T}} \int_0^{\mathcal{T}} \mathrm{d}t \Big\{ \hat{\mathbf{x}} [I_{i \leftarrow i-\hat{\mathbf{x}}}(t) + I_{i+\hat{\mathbf{x}} \leftarrow i}(t)] + \hat{\mathbf{y}} [I_{i \leftarrow i-\hat{\mathbf{y}}}(t) + I_{i+\hat{\mathbf{y}} \leftarrow i}(t)] \Big\}, \tag{2.9}$$

which represents both the magnitude and direction of the local current at site i. Numerically, the time-averaged local current, e.g., $\frac{1}{\mathcal{T}} \int_0^{\mathcal{T}} \mathrm{d}t \; I_{i \leftarrow i-\hat{\mathbf{x}}}(t)$, is given in the Floquet representation by:

$$\frac{1}{\mathcal{T}} \int_0^{\mathcal{T}} \mathrm{d}t \; I_{i \leftarrow i-\hat{\mathbf{x}}}(t) = \sum_{m \in \mathbb{Z}} \int_{\mathbb{R}} \frac{\mathrm{d}E}{2\pi\hbar} \tilde{J}_{i-\hat{\mathbf{x}},i}(m) \boldsymbol{G}^{<}_{(i,i-\hat{\mathbf{x}};0,m)}(E), \tag{2.10}$$

where $\tilde{J}_{i-\hat{\mathbf{x}},i}(m) = \frac{1}{\mathcal{T}} \int_0^{\mathcal{T}} \mathrm{d}t \, \mathrm{e}^{\mathrm{i}m\Omega t} J_{i-\hat{\mathbf{x}},i}(t)$ is the mth Fourier component of the $\mathcal{T}$-periodic function $J_{i-\hat{\mathbf{x}},i}(t)$. Furthermore, at a particular energy E, the *energy-resolved* time-averaged local current is defined as: $I_{i \leftarrow i-\hat{\mathbf{x}}}(E) = \sum_{m \in \mathbb{Z}} \tilde{J}_{i-\hat{\mathbf{x}},i}(m) \boldsymbol{G}^{<}_{(i,i-\hat{\mathbf{x}};0,m)}(E)$. Correspondingly, the energy-resolved local DC component of current vector at site i reads:

$$\begin{aligned} \vec{I}_i(E) = \sum_{m \in \mathbb{Z}} & \hat{\mathbf{x}} \Big[\tilde{J}_{i-\hat{\mathbf{x}},i}(m) \boldsymbol{G}^{<}_{(i,i-\hat{\mathbf{x}};0,m)}(E) + \tilde{J}_{i,i+\hat{\mathbf{x}}}(m) \boldsymbol{G}^{<}_{(i+\hat{\mathbf{x}},i;0,m)}(E) \Big] \\ & + \hat{\mathbf{y}} \Big[\tilde{J}_{i-\hat{\mathbf{y}},i}(m) \boldsymbol{G}^{<}_{(i,i-\hat{\mathbf{y}};0,m)}(E) + \tilde{J}_{i,i+\hat{\mathbf{y}}}(m) \boldsymbol{G}^{<}_{(i+\hat{\mathbf{y}},i;0,m)}(E) \Big] + \text{c.c.} \end{aligned} \tag{2.11}$$

The DC profile is constructed by plotting this quantity at every site i of the central system.

2.3.3 Time-averaged LDOS

The time-averaged LDOS describes the spatial distribution of states, thus allowing us to inspect whether edge states are present at a certain energy E. For static systems, the LDOS is defined by $\mathrm{LDOS}_i(E) = -\frac{1}{\pi} \mathrm{Im} G^r_{ii}(E)$. To extend this notion to Floquet systems, we need to decompose the dynamics into two parts, corresponding to the average time T and relative time τ in the Wigner representation of Green's functions [198]. When a periodic steady state is achieved, it is natural to average the

Green's function over a driving period, yielding the following expression of time-averaged LDOS: $\text{T-LDOS}_i(E) = -\frac{1}{\pi}\text{Im}\frac{1}{\mathcal{T}}\int_0^{\mathcal{T}} \mathrm{d}T\ \bar{G}^r_{ii}(T,E)$. In the Floquet representation, it has the following expression:

$$\text{T-LDOS}_i(E) = -\frac{1}{\pi}\text{Im}\boldsymbol{G}^r_{(i,i;0,0)}(E), \tag{2.12}$$

which is used in our numerical studies.

2.4 Floquet-Green's function

Thus far, we have expressed physical quantities in terms of the Green's functions and self-energies. We also have the following relations to help simplify algebraic manipulations: (i) causality, i.e., $[\boldsymbol{G}^r_{(i,j;m,n)}]^\dagger(E) = \boldsymbol{G}^a_{j,i;n,m}(E)$, and (ii) fluctuation-dissipation relations for leads, i.e., $\boldsymbol{\Sigma}^<_{L/R} = -[\boldsymbol{\Sigma}^r_{L/R} - (\boldsymbol{\Sigma}^r_{L/R})^\dagger] f^{L/R}$ [159, 194]. As shown in Equations 2.7, 2.11 and 2.12, for the calculations of physical quantities, it all boils down to two Green's functions: the retarded and lesser. Hence, we give here their governing equations, which can be calculated with the center Hamiltonian and lead self-energies as input.

The retarded Green's function satisfies the Dyson equation, which in the Floquet representation is given by [199]:

$$\sum_{k\in\mathbb{Z}} \Big[(E + m\hbar\Omega)\delta_{mk} - H_{m-k} - (\boldsymbol{\Sigma}^r_L + \boldsymbol{\Sigma}^r_R)_{mk}\Big]\boldsymbol{G}^r_{kn}(E) = \delta_{mn}. \tag{2.13}$$

The solution of this equation is found by truncating over the Fourier components, followed by a matrix inversion. In practice, if we need to deal with large system sizes and large number of harmonics, direct inversion is not feasible, since its complexity scales like $(N_x N_y n_\text{F})^3$, where N_x (N_y) is the number of lattice sites along x (y) direction, and n_F is the truncated number of harmonics in frequency space. To surmount this

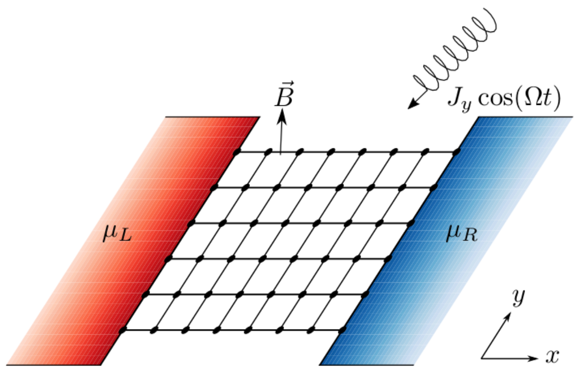

Figure 2.1: Schematic of the system studied in this chapter. The left (right) lead has chemical potential μ_L (μ_R). The central system is a square tight-binding lattice subject to a perpendicular magnetic field $\vec{B}$ and a harmonic driving field with driving amplitude $J_y \cos(\Omega t)$.

difficulty, we adapt the recursive Green's function method [197] to Floquet systems (see Appendix A). The lesser Green's function is related to the retarded Green's function through the Keldysh equation [159, 194]. In the Floquet representation, it reads:

$$\boldsymbol{G}^{<}_{mn}(E) = \sum_{p,q\in\mathbb{Z}} \boldsymbol{G}^{r}_{mp}(E)(\boldsymbol{\Sigma}^{<}_{L} + \boldsymbol{\Sigma}^{<}_{R})_{pq}(E)\boldsymbol{G}^{a}_{qn}(E). \tag{2.14}$$

2.5 Model

We consider a two-terminal device as illustrated in Figure 2.1. The central system is a quantum well heterostructure described by the harmonically driven Hofstadter model (HDHM). This model has been studied before and features many interesting Floquet topological phases, e.g. with nearly flat bands, large Chern numbers, and counter-propagating edge states [200]. In this work, we put this model in a two-terminal transport setup: the central system is coupled to two metallic leads, which are kept separately in thermal equilibrium with chemical potentials μ_L and μ_R. The total

Hamiltonian $\mathcal{H}(t)$ describing the central system, leads and their couplings is given by:

$$\mathcal{H}(t) = H_L + V_L + H(t) + V_R + H_R, \tag{2.15}$$

where

$$H(t) = \sum_i \{ J_x c_i^\dagger c_{i+\hat{\mathbf{x}}} + J_y \left[s + \cos(\Omega t) \right] \mathrm{e}^{\mathrm{i}2\pi\alpha x_i} c_i^\dagger c_{i+\hat{\mathbf{y}}} + \text{h.c.} \} \tag{2.16}$$

is the Hamiltonian of HDHM at the center, with a magnetic flux $\alpha = p/q \in \mathbb{Q}$ per unit area. $q \in \mathbb{N}$ is the number of sublattices in each magnetic unit cell, and Ω is the frequency of the driving field. We abbreviate the lattice coordinates as $i \equiv (x_i, y_i)$. The leads are modeled as two semi-infinite (along x) square lattices, with nearest-neighbor hopping amplitudes $t_{x/y}$ along x/y directions and a uniform onsite potential v:

$$H_{L/R} = \sum_i \left[\left(t_x a_i^\dagger a_{i+\hat{\mathbf{x}}} + t_y a_i^\dagger a_{i+\hat{\mathbf{y}}} + \text{h.c.} \right) + v a_i^\dagger a_i \right]. \tag{2.17}$$

In our transport calculations, we take the tunneling amplitude between the leads and central system along x-direction to be the same as t_x. Under this choice, the Hamiltonian describing the coupling between the left (right) lead and the central system is give by:

$$V_{L(R)} = t_x \sum_{\ell, i : [x_\ell = -1(+1), x_i = 0]} \left(a_\ell^\dagger c_i + \text{h.c.} \right). \tag{2.18}$$

Along y-direction, we take open boundary condition for the central system in all our transport calculations below.

2.6 Floquet spectrum

Taking periodic boundary conditions along x/y-direction and open boundary condition for the other direction, we can Fourier transform the coordinate x/y in Equation 2.16

into a quasimomentum k_x/k_y. The resulting Hamiltonian is given by either of the following:

$$\begin{aligned}
H_{k_y}(t) = & \sum_{x=0}^{N_x-1} \{ J_x \Big(c^\dagger_{x,k_y} c_{x+1,k_y} + \text{h.c.} \Big) \\
& + 2J_y \left[s + \cos(\Omega t) \right] \cos(2\pi\alpha x + k_y) c^\dagger_{x,k_y} c_{x,k_y} \}, \\
H_{k_x}(t) = & \sum_{y=0}^{N_y-1} \Bigg\{ J_x \Bigg(c^\dagger_{q-1,y} c_{0,y} \mathrm{e}^{\mathrm{i}k_x q} + \sum_{j=0}^{q-2} c^\dagger_{j,y} c_{j+1,y} \Bigg) \\
& + J_y \left[s + \cos(\Omega t) \right] \sum_{j=0}^{q-1} \Big(c^\dagger_{j,y} c_{j,y+1} \mathrm{e}^{\mathrm{i}2\pi\alpha j} + \text{h.c.} \Big) \Bigg\}.
\end{aligned} \tag{2.19}$$

These are just 1D descendants of the HDHM, also called the driven Harper model [201]. One can then obtain the Floquet spectrum with respect to k_x or k_y by solving the Floquet-Schrödinger equation [202, 203] using $H_{k_x}(t)$ or $H_{k_y}(t)$. The nontrivial topology of a Floquet band is then signaled by the presence of gapless edge states. Furthermore, as the quasienergy is defined module the driving frequency, it is possible for gapless edge modes to wind around the Floquet-Brillouin zone, a scenario absent in static systems [174, 200]. Note also that, one may intuitively prefer to inspect the edge states with open boundary condition along y, so as to plot the dispersion relation of the edge states as a function of k_x to understand the transport along the x direction. However, in terms of understanding the bulk-edge correspondence and locating the edge states in connection with the Floquet spectrum gap (exceptions to be discussed below), choosing $H_{k_y}(t)$ or $H_{k_x}(t)$ for the Floquet spectrum to digest the transport results is just a matter of taste.

2.7 Edge-state transport under harmonic driving

Using the theoretical and computational methods discussed in Section 2.2, we now investigate the transport of Floquet edge states in the two-terminal device introduced in

Section 2.5. We first look into the DC conductance of our model system in the pristine limit, where we observe a conductance quantization by the Floquet sum rule [186, 187]. Next, we introduce defects and disorder into our system, and present a detailed comparison of the robustness among three different types of gapless Floquet edge states. Finally, we consider a practical situation in which the leads have a finite bandwidth, and discuss its impact on Floquet edge state transport. In all calculations presented below, we take $J_x = 1$ as the unit of energy.

Following the discussions of Section 2.2, the DC conductance at low bias in zero temperature is given by Eq. (2.7) in units of e^2/h. Using the HDHM (Eq. 2.16) as our Hamiltonian, we now present results of DC conductance for different sets of system parameters (Figure 2.2). The curves (except black triangles) in the left panels of Figure 2.2a represent $T(E + n\hbar\Omega)$, i.e. the DC conductance in units of e^2/h *at energy* $E + n\hbar\Omega$, with different values of n. In other words, $T(E + n\hbar\Omega)$ is the contribution of the nth Floquet sideband to the DC conductance *at a given quasienergy* $\mu = E \in [-\hbar\Omega/2, \hbar\Omega/2]$.

For the self-energy of the leads, we take the wide-band approximation (WBA), which is valid when the lead has a much larger bandwidth than that of the central system [193, 204]. Under this approximation, the self energies due to the leads are independent of energy E. More explicitly, these self-energy functions satisfy $\Sigma^L_{ij} \propto -\mathrm{i}\delta_{x_i,0}\delta_{i,j}\Gamma^L/2$ and $\Sigma^R_{ij} \propto -\mathrm{i}\delta_{x_i,N_x-1}\delta_{i,j}\Gamma^R/2$, where $\Gamma^{L/R} > 0$ are constants taken to be the same as J_x. In Section 2.9, we shall discuss the consequences if this assumption is lifted. Also, in all of our calculations, we have made sure that the number of Floquet sidebands n_{F} is large enough. Specifically, $n_{\mathrm{F}} = 13$ is a truncation dimension that guarantees convergence in all our computational examples.

For the parameters used to compute Figure 2.2a, the system admits five Floquet

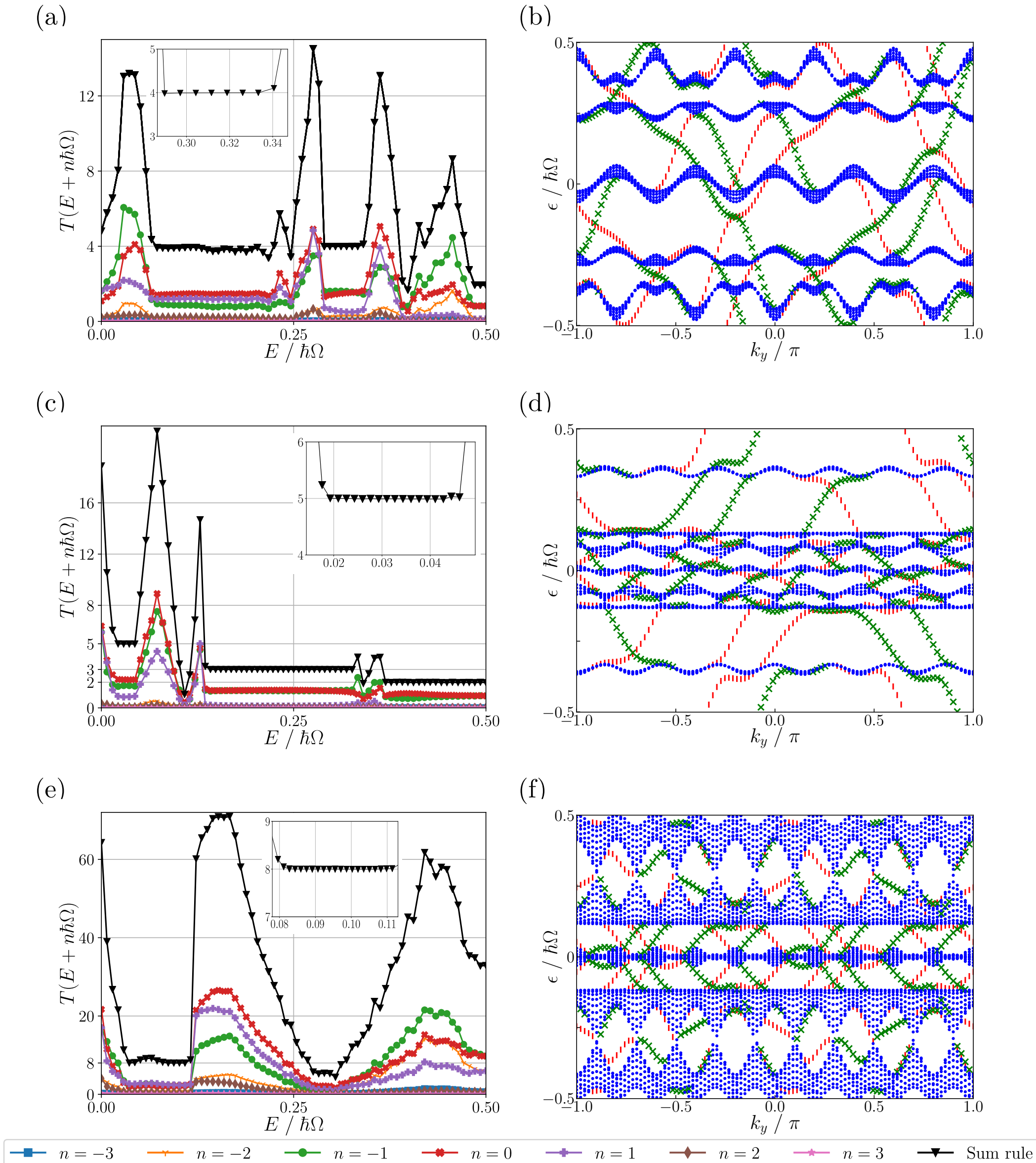

Figure 2.2: Two-terminal DC conductance of the HDHM at zero temperature. Left panels: transmission $T(E + n\hbar\Omega)$ vs. energy E of an incoming electron at different Floquet indices n, whose markers are indicated in the bottom legend. Curves with black triangles are obtained after applying the Floquet sum rule, with insets zoomed in to the plateaus of interest. Right panels: Floquet spectrum of the same model with PBC (OBC) along $y(x)$-direction. Red "|"s and green crosses denote states localized at left and right edges of the sample. System parameters are $J_y = 1.6, \alpha = 1/5, \Omega = \pi, s = 1, N_x = N_y = 100$ for panels (a) and (b), $J_y = 1.3, \alpha = 2/7, \Omega = \pi, s = 1, N_x = N_y = 80$ for panels (c) and (d), and $J_y = 1.3, \alpha = 1/5, \Omega = \pi/2, s = 0, N_x = N_y = 100$ for panels (e) and (f).

bulk bands, as shown in Figure 2.2b. In the first gap above the middle band, there are four Floquet edge states, with a net gap chirality of two. Within this quasienergy gap, the transmissions of each Floquet sideband (curves other than black triangles) form well-defined plateaus. The non-quantization of these plateaus can be understood as follows [187]. Each Floquet sideband n, corresponding to an incoming state at *energy* $E + n\hbar\Omega$, has a non-unity overlap with the Floquet edge state at *quasienergy* $\epsilon = E$ hosted by the central system, leading to a transmission smaller than the expected number of edge states. This understanding [187] provides an intuitive motivation to the so-called Floquet sum rule [186], a transport feature unique to Floquet topological phases that was not yet well recognized at the time this research was carried out.

More concretely, the Floquet sum rule dictates that, if one observes gapless edge modes in the Floquet spectrum, then quantized transmission *at a quasienergy* $\epsilon_0 = E_0 \in [-\hbar\Omega/2, \hbar\Omega/2]$ can be recovered by summing over the transmissions *at energies* $E + n\hbar\Omega$ due to different Floquet sidebands:

$$T(\epsilon_0) = \sum_{n\in\mathbb{Z}} T(E_0 + n\hbar\Omega). \tag{2.20}$$

As shown in Figure 2.2a, we found $T(\epsilon_0) = 4, 4, 2$ for ϵ_0 in the first, second and third quasienergy band gaps above the middle Floquet band, an observation fully consistent with the Floquet gap features (such as the number of edge states) shown in Figure 2.2b. In addition to several studies involving the Floquet sum rule in quantum spin Hall insulators [187] and Chern insulators [188], here we confirm it in quantum Hall insulators. Furthermore, in the first and third quasienergy gaps above $\epsilon = 0$ in Figure 2.2b, we observe counter-propagating gapless edge modes at the same edge [200, 205], which are unique to Floquet topological phases[2]. The corresponding DC conductance calculations

[2]Counter-propagating edge states may also exist in static systems, e.g. in quantum spin Hall effect

(Figure 2.2a) confirm that these counter-propagating edge modes also adhere to the Floquet sum rule.

We note that any possible observation of the Floquet sum rule would be rather challenging. One needs to prepare different initial states at chemical potentials $E + n\hbar\Omega$ to execute different experimental runs in order to measure the contributions from all Floquet sidebands to the transport at quasienergy $\epsilon = E$. Nevertheless, it would be of great interest to experimentally confirm the results in Figures 2.2c and 2.2e. There, one sees that with suitable system parameters, the DC conductances due to Floquet edge states (after applying the Floquet sum rule) can reach $5e^2/h$ and even $8e^2/h$, which surpass the largest edge state conductance ever realized experimentally in undriven systems. By contrast, for transport situations where the chemical potential is held constant and not allowed to be adjusted, the Floquet edge state transport is unlikely to be substantially larger than static systems, as indicated by the individual sidebands (curves other than black triangles) in Figures 2.2a, 2.2c and 2.2e. The robustness of such Floquet edge state transport will be studied in the next subsection.

2.8 Topological protection of Floquet edge currents

One advantage of topological edge state transport is its robustness against structural imperfections. While this has been demonstrated by the conductance plateaus in disordered quantum Hall samples [18], the robustness of Floquet topological systems are yet to be confirmed experimentally.

Here we numerically study the response of gapless Floquet edge modes to disorder

(which is spin-degenerate). However, here our system breaks time reversal symmetry and consists of spinless electrons. To our knowledge, such systems are not expected to host counter-propagating edge modes in absence of driving.

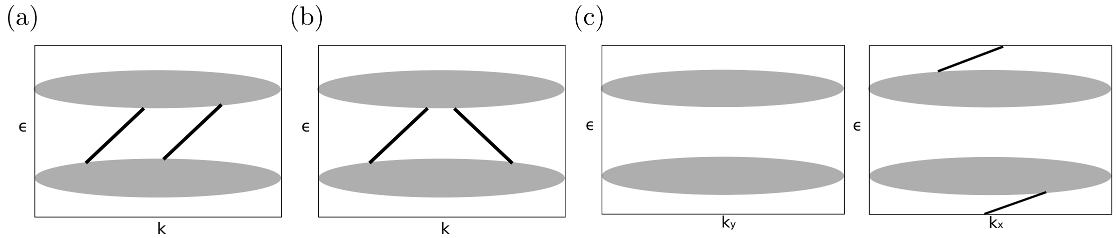

Figure 2.3: Schematic of three different types of edge states. The open boundary condition is taken along only one direction. Shaded regions represent bulk bands. Lines represent co-propagating edge bands in panel (a), counter-propagating edge bands in panel (b), and symmetry-restricted gapless edge bands in panel (c). In panel (c), only when the open (periodic) boundary condition is taken along y-direction (x-direction) does one observe the edge states.

and defects. Thanks to the richness of the harmonically-driven Hofstadter model, we are able to realize: (i) co-propagating, (ii) counter-propagating, (iii) symmetry-restricted gapless edge states, and probe their robustness with the tools we developed.

Before presenting the numerical results, we briefly describe each type of edge modes. The first kind, co-propagating Floquet edge states, are chiral in the following sense: under a stripe geometry, each edge only hosts states dispersing in a fixed direction. They have a modified bulk-edge correspondence to the nontrivial topology of the bulk bands [206] as there may exist anomalous winding edge states in Floquet systems. The second type, counter-propagating edge modes, are as the name suggests: under a stripe geometry, each edge hosts states that are moving forward and backward. If the chirality (number of left movers minus number of right movers) is zero, unlike the spin-momentum-locked helical edge states in quantum spin Hall effect, one generally does not expect protection of these counter-propagating edge modes against disorder. The third kind, dubbed symmetry-restricted edge modes, are gapless but only exist when the stripe is taken in a particular way. They may be co- or counter-propagating, but in our model the ones we found are counter-propagating. An illustration of the

Floquet spectra in presence of these edge modes is given in Figure 2.3.

Since these three types of edge modes are not mutually exclusive (i.e. two of them may simultaneously exist at different quasienergies for the same system parameters), we organize the following discussions by the type of imperfections (disorder or defect). Our computational studies are summarized in Table 2.1.

2.8.0.1 Response to on-site disorder

We introduce disorder to the HDHM by assigning to each site a random on-site potential. The resulting Hamiltonian of the disordered central system is given by:

$$H_{\text{dis}}(t) = H(t) + \sum_i \xi_i c_i^\dagger c_i. \tag{2.21}$$

The term $\sum_i \xi_i c_i^\dagger c_i$ changes the potential on each site i by ξ_i, where ξ_i is a random number uniformly distributed in $[-W, W]$, where W is the disorder strength.

Consider first the case in which the Floquet spectrum of the HDHM without disorder is shown in Figure 2.5a, where there are three co-propagating chiral edge states in the first gap above the middle Floquet band, and a pair of counter-propagating edge states winding around quasienergies $\epsilon = \pm\hbar\Omega/2$. Such counter-propagating edge states are unique to Floquet systems. To investigate their robustness to disorder, we calculate the transmission coefficients and T-LDOS at different quasienergies.

From the T-LDOS for a pristine lattice depicted in Figures 2.4a and 2.4d, we see that the chiral modes at $\epsilon = 0.25$ and the counter-propagating modes at $\epsilon = 1.3$ are indeed localized at the edges. Upon the introduction of disorder—even at a strength comparable to the size of the spectral gap—the T-LDOS still retain their edge features. At first glance, this seems to suggest that both types of edge states are favorably robust against disorder. However, if we inspect the DC conductance, where, as shown in Figure 2.5b for $\epsilon/(\hbar\Omega) \sim 0.4 - 0.5$, the conductance plateau due to counter-propagating anomalous edge

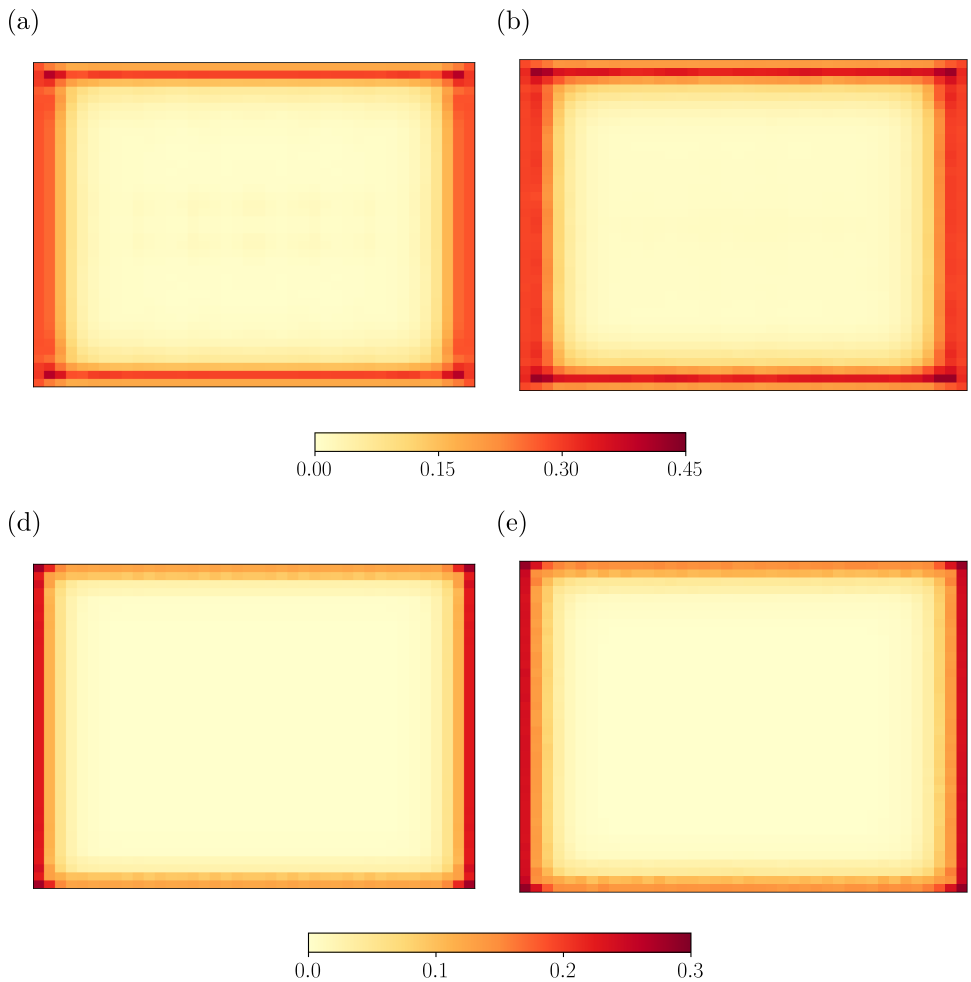

Figure 2.4: Time-averaged LDOS at quasienergy $\epsilon = 0.25$ for panels (a), (b), and $\epsilon = 1.3$ for panels (c), (d), after summing over the contributions from Floquet sidebands as in the Floquet sum rule. Panels (a) and (c) show results for pristine central systems, whereas panels (b) and (d) show results for disordered central systems, each averaged over 200 different disorder realizations. The disorder is implemented via onsite random potentials, which penetrates all four edges by a depth of three layers each. The disorder strength is $W = 0.7$. The system size is $N_x = N_y = 40$. Other system parameters are $J_y = 1.5, \alpha = 1/5, \Omega = \pi$ and $s = 0.7$.

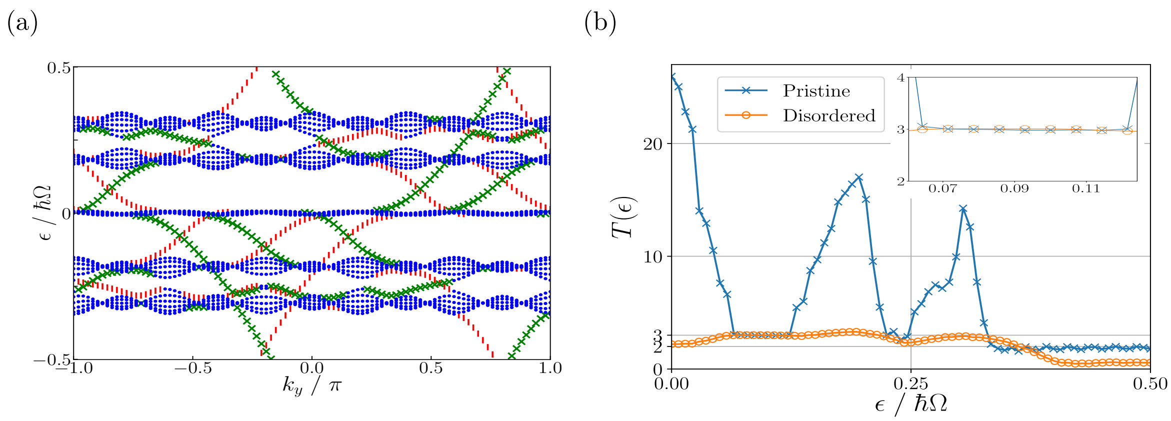

Figure 2.5: Left panel: Floquet spectrum of the HDHM with PBC (OBC) along $y(x)$-direction. Red "|"s and green crosses denote states localized at left and right edges of the sample. Right panel: transmission coefficient $T(\epsilon)$ (after applying the Floquet sum rule) at different quasienergies ϵ in the upper half of the Floquet quasienergy Brillouin zone for both pristine and disordered samples. The disorder strength $W = 1$. The results for disordered sample are averaged over 100 different disorder realizations. Other system parameters are the same as those shown in the caption of Figure 2.4.

states is appreciably pushed down by disorder from being quantized at 2. Thus from the perspective of conductance quantization, counter-propagating Floquet edge states are actually not robust. Indeed, the net winding number at quasienergies $\epsilon = \pm\hbar\Omega/2$ is zero. Therefore the corresponding edge states are topologically trivial and are generally not expected to resist disorder. This is in contrast to the anomalous Floquet edge modes with non-vanishing winding numbers studied in Ref. [206], which are robust against disorder. From Figure 2.5b one can draw two more observations. First, the plateau due to co-propagating chiral edge states remains intact in presence of disorder, akin to the static quantum Hall insulators. Of topological origin, this robustness is related to the Chern numbers of the Floquet bands which cannot change without closing the spectral gaps. Second, the very high conductance peaks are suppressed when disorder is introduced into the pristine sample. This is evidence that these peaks originate from

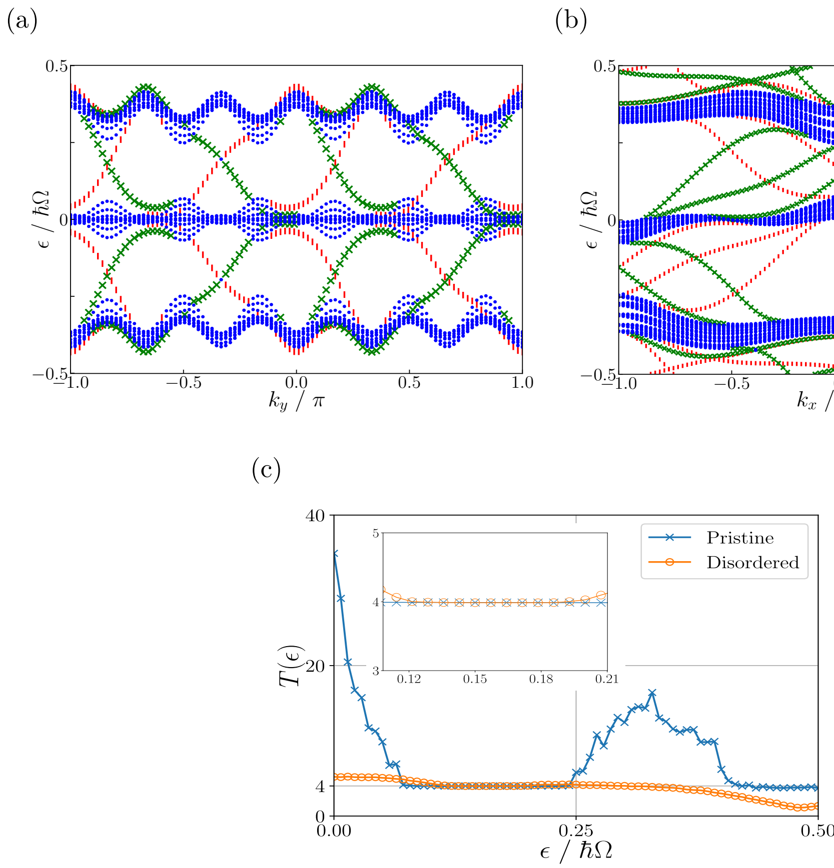

Figure 2.6: Panel (a): Floquet spectrum of the HDHM with PBC (OBC) along $y(x)$-direction. Red "|"s and green crosses denote states localized at left and right edges of the sample. Panel (b): Floquet spectrum of the HDHM with the same parameters, but with PBC (OBC) along $x(y)$-direction. Panel (c): transmission $T(\epsilon)$ (after applying the Floquet sum rule) at different quasienergies ϵ in the upper half of the Floquet quasienergy Brillouin zone for both pristine and disordered samples. The disorder strength $W = 1$. The results for disordered sample are averaged over 100 different disorder realizations. The other system parameters are $J_y = 1.25, \alpha = 1/3, \Omega = \pi/2, s = 0$ and $N_x = N_y = 45$.

Floquet bulk states and as such they are not topologically protected. This remarkable response of bulk states to disorder should allow one to clearly distinguish conductance contributions from bulk and from topological edge states.

As an aside, we consider another type of Floquet edge states restricted by the symmetry of the system. One such example is presented in Figures 2.6a and 2.6b for a 3-band case, where counter-propagating edge modes appear in quasienergy band gaps around $\pm\hbar\Omega/2$, only if the periodic boundary condition is taken along the x-direction. This is similar to graphene, where dispersionless edge states appear only in zigzag ribbons [207] but not in ribbon with armchair edges. To study the robustness of transport contributed by such kind of Floquet edge states, we resort to the DC conductance in the presence of disorder. As shown in Figure 2.6c, there are two plateaus corresponding to the same quantized conductance $4e^2/h$. The one closer to the central Floquet band (due to co-propagating Floquet edge modes) is manifestly more robust against disorder than the one further away (due to symmetry-restricted Floquet edge modes).

For the sake of completeness, we also studied the transport property of topologically trivial gapped Floquet edge states, and found that they are indeed not robust to disorder and defects. More details are presented in Appendix C.

2.8.0.2 Response to sample defects

A hallmark of quantum Hall insulators is the existence of chiral edge modes, which can move past defects located at sample boundaries and maintain their propagation directions without being scattered backward. In photonic and phononic analog of Floquet topological insulators, the robustness of edge states against sample defects have been demonstrated in Refs. [208, 209]. Here we propose the local DC profile

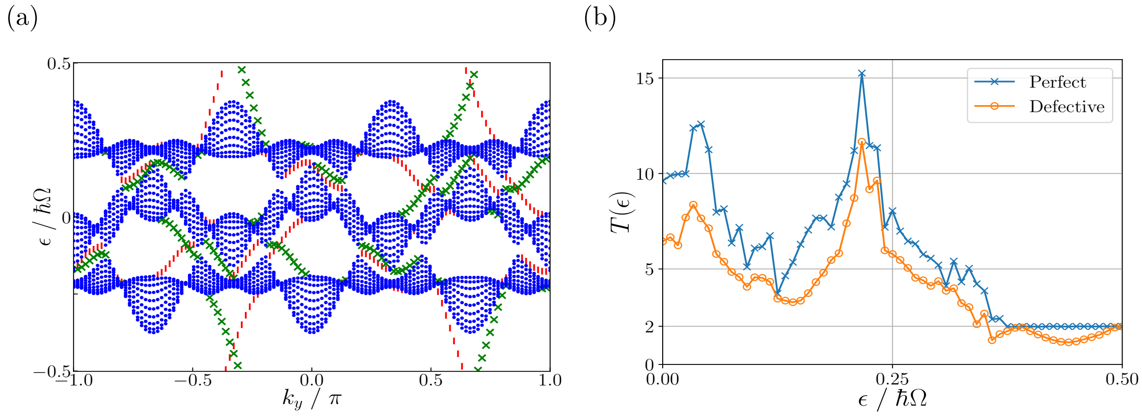

Figure 2.7: Panel (a): Floquet spectrum of the HDHM with PBC (OBC) along $y(x)$-direction. Red "|"s and green crosses denote states localized at left and right edges of the sample. Panel (b): transmission coefficient vs. quasienergy with the Floquet sum rule applied. The curve with crosses (circles) corresponds to the perfect (defective) sample shown in left (right) panels of Figure 2.8. Other system parameters are chosen as $J_x = 1,\ J_y = 1.6,\ \alpha = 1/3,\ \Omega = \pi,\ s = 1$.

(Section 2.3.2) as a tool to study the response of edge states to defects in Floquet quantum Hall insulators. We introduce a defect to the system by removing all terms coupled to the defect from the system Hamiltonian. For example, the Hamiltonian of the HDHM with a single defect at site $d \equiv (x_d, y_d)$ is given by:

$$H_{\text{def}}(t) = H(t) - \left\{ J_x c_d^\dagger c_{d\pm\hat{\mathbf{x}}} + J_y \left[s + \cos(\Omega t)\right] \mathrm{e}^{\pm \mathrm{i}2\pi\alpha x_d} c_d^\dagger c_{d\pm\hat{\mathbf{y}}} + \text{h.c.} \right\}. \tag{2.22}$$

The local DC profile is then determined as follows: at each site of the lattice, evaluate Equation 2.11 and then represent the result as an arrow. Following the rationale behind the Floquet sum rule, this will be done for not just a single energy and chemical potential at (E, μ_L, μ_R), but also for those that are at integer multiples of the driving frequency away, i.e., with chemical potentials at $(E + n\hbar\Omega, \mu_L + n\hbar\Omega, \mu_R + n\hbar\Omega)$.

We present the DC profile at energy $E = 1.5 + n\hbar\Omega$ in Figure 2.8, with the same system parameters as in Figure 2.7. The chemical potentials of the left and right leads

(a) $n = -1$

(b) $n = -1$

(c) $n = 0$

(d) $n = 0$

(e) Floquet sum rule applied

(f) Floquet sum rule applied

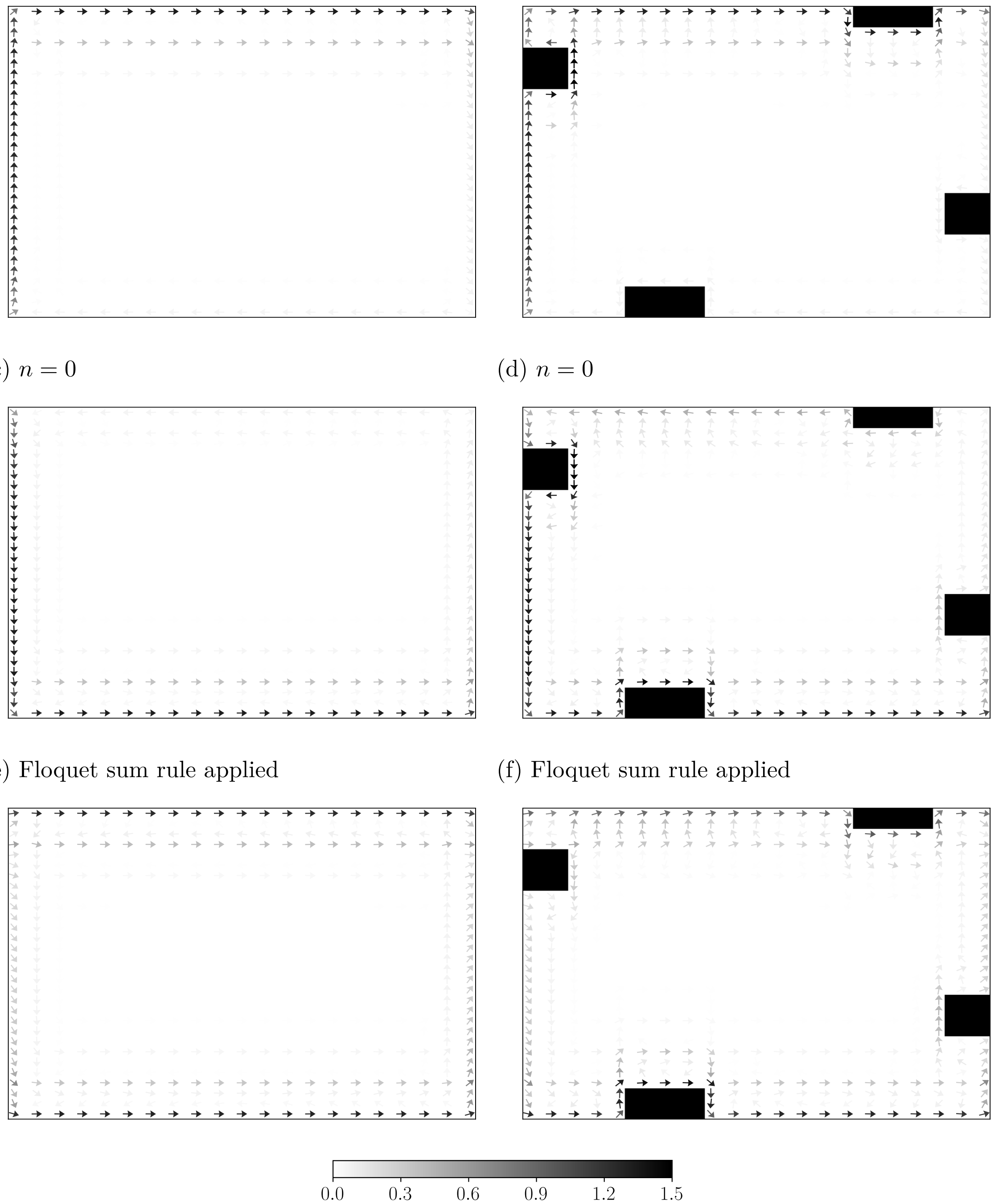

Figure 2.8: Local DC profile for perfect (left panels) and defective (right panels) samples. Arrows point along the direction of local currents, whose magnitude is indicated by the color intensity as given in the colorbar (in units of $J_x/\hbar$). The system parameters are $E = 1.5, \mu_L = 1.51, \mu_R = 1.49, N_x = 41, N_y = 30, J_y = 1.6, \alpha = 1/3, \Omega = \pi$ and $s = 1$.

are set at $\mu_L = 1.51 + n\hbar\Omega$ and $\mu_R = 1.49 + n\hbar\Omega$, both within the Floquet band gap. We introduce small blocks of defects to our sample as shown in Figure 2.8. In Figures 2.8a and 2.8c, we see that the local currents due to harmonics $n = -1$ and $n = 0$ flow mainly along the top and bottom boundaries of the sample, respectively. Contributions from other Floquet sidebands are negligible and therefore not shown. After applying the Floquet sum rule, we obtain the DC profile as shown in Figure 2.8e, which shows two edge channels propagating from the left to the right leads along the sample boundaries.

We then turn to defective samples. In Figure 2.8b, the local current associated with harmonic $n = -1$ bypasses the defects and maintains its propagation direction along the upper edge. Similarly, along the lower edge, the local current due to harmonic $n = 0$ is immune to backscattering (Figure 2.8d). Remarkably, along the upper boundary, the harmonic $n = 0$ contributes a non-vanishing current that flows against the bias. This backward-moving channel clearly indicates the sensitivity of counter-propagating edge modes to sample defects. Figure 2.8f presents the overall DC profile after summing over contributions from all Floquet sidebands at quasienergy $\epsilon = 1.5$. Here a weaker edge current signal compared to that of Figure 2.8e is observed, suggesting a deviation from conductance quantization due to defects. This is confirmed by the string of circles hanging off the plateau of crosses in the right end of the transmission characteristics shown in Figure 2.7b. For completeness, we also checked the case with co-propagating Floquet edge states, and find that they are robust against defects (C.1b and C.3d in Appendix C).

In summary, we have confirmed that counter-propagating Floquet edge states are not robust against defects, as expected from a vanishing winding number across the Floquet-Brillouin zone. Also, as a computational tool, the local DC profile carries more information than the DC conductance and T-LDOS, in that it is able to distinguish

	DC conductance		Time-averaged LDOS		Local DC profile	
	Plateau	Stable	Edge pattern	Disorder	Flows on edge	Defect
(A)	×	–	✓	×	✓	×
(B)	✓	×	✓	×	✓	×
(C)	✓	×	✓	✓	✓	✓
(D)	✓	✓	✓	✓	✓	✓

Table 2.1: Four types of edge states and their response towards disorder and defect. The check mark (cross mark) means robust (not robust) to the corresponding perturbation. (A): Gapped, (B): Symmetry-restricted gapless, (C): Counter-propagating gapless, (D): Co-propagating gapless.

the chirality of different harmonics, which all correspond to the same quasienergy.

In Table 2.1, we summarize the robustness of Floquet edge states studied in this subsection. For completeness, the robustness of topologically trivial gapped edge states is also listed here, with more details spelled out in Appendix C. The co-propagating chiral edge states in Floquet quantum Hall insulators are the most robust against local perturbations, and therefore potentially most useful in realizing high-precision electronic transport devices.

2.9 Beyond the wide-band approximation

Up to now, our calculations were done under the WBA [193, 204], where the leads are assumed to be able to accommodate uniformly all energy states of the central system. However, in Floquet topological systems, the transport *at a quasienergy* requires contributions from energies spanning several Floquet-Brillouin zones. Thus, it is all the more appealing to model the leads as having only finite bandwidths. For this purpose, it suffices to focus on a parameter regime as given in Figure 2.9a. We model the leads as square lattices with nearest-neighbor hoppings described by Equation 2.17 and compute the DC transmission. For broadband leads (dash-dotted line in Figure 2.9b),

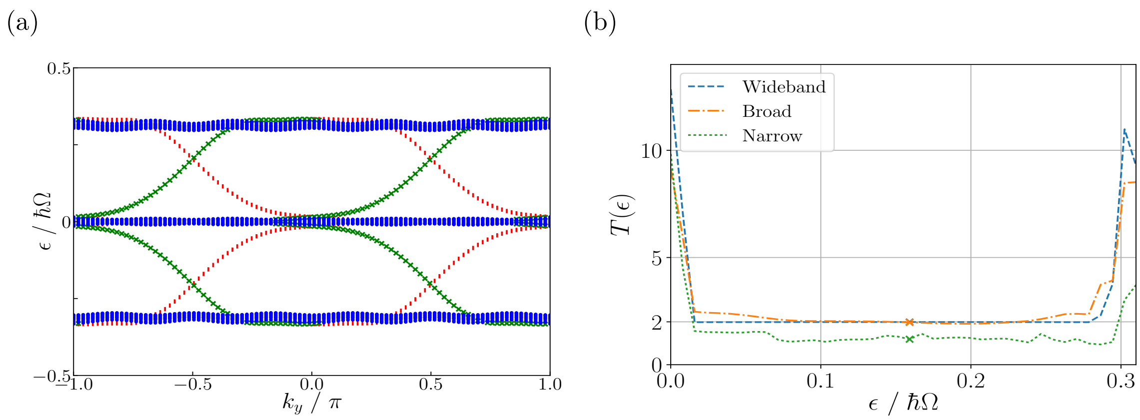

Figure 2.9: Panel (a): Floquet spectrum of the HDHM with PBC (OBC) along $y(x)$-direction. Panel (b): DC component of the transmission coefficient $T(\epsilon)$ at different quasienergies (with the Floquet sum rule applied) for leads with three types of bandwidth. The broad (narrow) bandwidth corresponds to $t_x = t_y = 3$ ($t_x = t_y = 0.5$). The crosses mark the points at which we analyze the contribution of each side-peak to $T(\epsilon)$ in Figures. 2.10 and 2.11. The systems parameters are taken as $J_y = 1.6, \alpha = 1/3, \Omega = \pi, s = 0$ and $N_x = N_y = 30$.

upon applying the Floquet sum rule, the conductance quantization remains intact for quasienergies that are close to the center of the gap. On the contrary, for the case of a narrow-band leads (dotted line in Figure 2.9b), one no longer observes conductance quantization. These two results should be compared with the ideal case under the WBA, which corresponds to the use of leads with infinitely-broad band (dashed line in Figure 2.9b).

To understand these observations, let us select a quasienergy in the middle of the gap, $\epsilon = E_0 = 1.5$ (crossed markers in Figure 2.9b). Consider now the three Floquet sidebands that contribute to a quantized conductance in the WBA [dashed rectangles in Figure 2.10(b) and Figure 2.11(b)]. When the WBA is relaxed, the leads must have non-vanishing density of states in these Floquet zones, in order for the corresponding sidebands to participate in the transport at $\epsilon = 1.5$. This is the case for

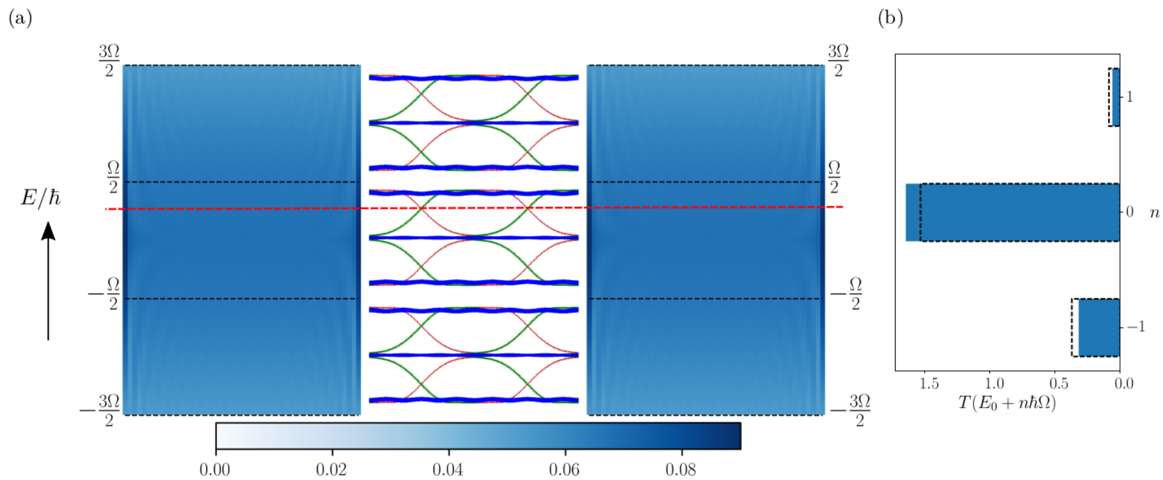

Figure 2.10: When attached to leads with a finite, yet broad enough bandwidth ($t_x = t_y = 3$), quantized transmission is observed after applying the Floquet sum rule. In (a), the color indicates the local density of states of the leads, calculated over $0, \pm 1$ Floquet zones, with energy as the vertical and y-direction as the horizontal axis. The HDHM has a quasienergy spectrum which repeats itself over integer multiples of the driving frequency Ω. The red dashed line at $E_0 = 0.5$ refers to the energy of the incoming electron. In (b), the side-peak contributions to the quantized DC conductance are shown. Dashed rectangles indicate the case of wideband limit.

the broadband leads [Figure 2.10(a)], whose DOS spreads uniformly throughout the first three $(0, \pm 1)$ Floquet zones. Hence, undeterred by a slight redistribution of the sideband weights [colored rectangles in Figure 2.10(b)], the DC conductance remains quantized as shown by the crossed marker in Figure 2.9b. Next, consider the case of narrow-band leads. Since their density of states is non-vanishing only at the $n = 0$ Floquet zone [Figure 2.11(a)], no electrons at energies $E_0 \pm \hbar\Omega$ can contribute to the transport at quasienergy $\epsilon = E_0$. Indeed, as shown in Figure 2.11(b), there is only one single colored rectangle at the center, which is, worse still, diminished compared to the case of WBA (dashed rectangle). Therefore, even the Floquet sum rule cannot salvage its conductance quantization [green cross in Figure 2.9b], because the lead bandwidths are simply too narrow for anything other than $E = E_0$ to contribute to the transport.

The above observation calls attention to the leads when studying the transport of Floquet topological systems. Suppose the central system is governed by a certain energy scale J, with the bandwidths of the leads characterized by Γ, such that $\Gamma \gg J$. In static systems, one can then simplify the problem using the WBA. But if the Floquet edge modes of interest are scattered throughout $\mathcal{N}$ dominant sidebands, such that $\mathcal{N}\Omega \gg \Gamma$, then the leads have states only within Γ, which, by the assumption $\mathcal{N}\Omega \gg \Gamma$, do not span some of the Floquet zones. It would then be inappropriate, in this case, to invoke the WBA from the get go.

In brief, unless sufficiently broad, the bandwidth of electronic leads may result in non-quantized DC edge conductances in Floquet Hall insulators. This suggests that any attempt at detecting quantized DC conductance (upon applying the Floquet sum rule) must involve electronic leads with bands wide enough to cover all contributing Floquet sidebands.

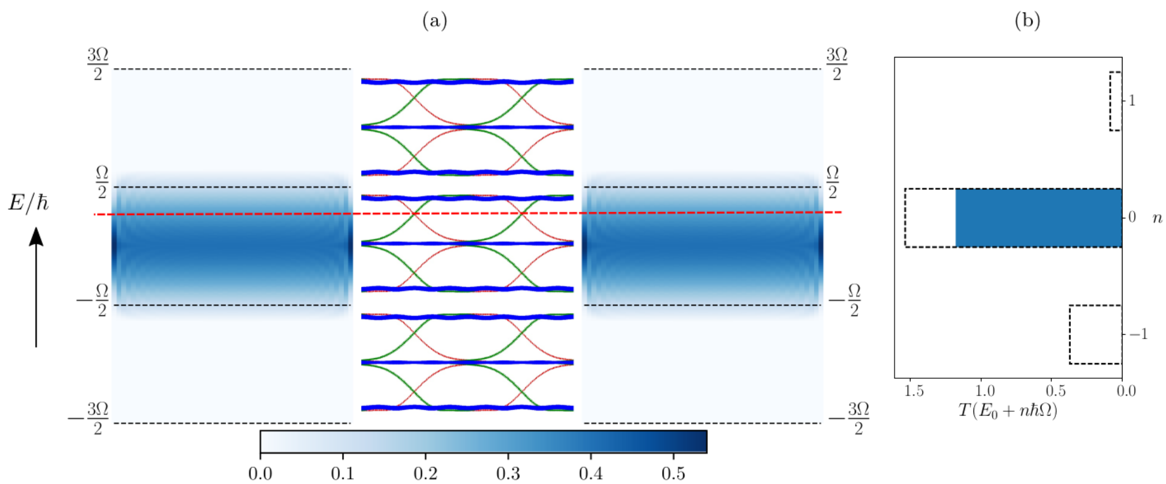

Figure 2.11: For leads with narrow bandwidth ($t_x = t_y = 0.5$), there is no quantized transmission even after performing the Floquet sum rule. This figure is plotted the same way as Figure 2.10

.

Chapter 3

Engineering topological phases with a three-dimensional nodal-loop semimetal

3.1 Preliminaries

Topological phases are often characterized by their remarkable symmetry protected surface states. A topological insulator in d dimensions harbors metallic states in its $(d-1)$-dimensional surfaces [5, 6]. In a topological semimetal, the conduction and valence bands touch in a region of co-dimension $p > 1$. For example, in nodal-point semimetals (NPSM), Fermi surfaces are zero-dimensional (0D) points connected by Fermi arcs in the surface Brillouin Zone (BZ) [210], whereas in the three-dimensional (3D) nodal-line (or loop) semimetals (NLSM) [211, 212], the touching region of bulk bands is one or several one-dimensional (1D) loops, with degenerate surface states within the projection of the loop in the two-dimensional (2D) surface BZ, commonly called "drumhead" surface states. In addition, NLSM with a plethora of loops with different topological features has been proposed [63, 69, 213]. Experimental identifications of NLSM have also been carried out in solid state systems recently [214, 215].

Connections between different topological phases have proved to be extremely helpful in the development of this research area. In particular, NLSM subject to a restricted class of gap terms opening up the bulk bands can yield familiar TI phases [167], with their topological feature characterized by a winding number defined for a gap term along the nodal loop of the original NLSM. The same winding number can be connected with the number of Dirac cones in the surface BZ. Thus, we are motivated in this chapter to seek a rich variety of topological phases under a unified scheme, namely, the introduction of an additional 2D gap term with a spin degree of freedom to 3D NLSM. Simply by tailoring the gap term whose dispersion relation can be carried over to the topological surface states, a number of intriguing topological phases can be engineered, including the previously discussed chiral insulator and those constructed recently by other means. For instance, we obtain an insulating phase with degenerate surface loop (DSL) in certain parameter regimes, and a higher-order topological insulator with 1D surface states on the hinges of two surfaces [35, 216, 217]. Since distinct topological surface states can be engineered by a tailored gap term applied to a common NLSM, studies of topological transitions between them will be fruitful. To distinguish these phases, we numerically study their two-terminal transport properties and discuss their different behaviors in transport measurements.

3.2 General approach

To illustrate how different topological phases may arise from NLSM, we consider the simplest two-band model for a 3D NLSM, the tight-binding Hamiltonian of which is given by

$$H_{\mathrm{NL}} = \left(t \sum_{i=x,y,z} \cos k_i - m \right) \tau_1 + \sin k_z \tau_3, \tag{3.1}$$

with τ the Pauli matrices acting on a pseudospin-1/2 space, e.g. a sublattice space. t is a hopping parameter, which is scaled to unity and serves as the energy scale hereafter. The dispersion relation of H_{NL} is given by $E_{\mathrm{NL}} = \sqrt{\left(\sum_{i=x,y,z}\cos k_i - m\right)^2 + \sin^2 k_z}$, which yields one or two nodal loops. Throughout, we concentrate on the case of $1 < m < 3$, with a single nodal loop $\boldsymbol{L}_0$ defined by $\cos k_x + \cos k_y = m - 1$ in the k_x–k_y plane with $k_z = 0$. This nodal loop is protected by $\mathcal{PT}$ symmetry, where $\mathcal{P}$ is the conventional parity operator and $\mathcal{T}$ represents the time-reversal operator, with $\mathcal{PT}H_{\mathrm{NL}}(\boldsymbol{k})\mathcal{T}^{-1}P^{-1} = H_{\mathrm{NL}}(\boldsymbol{k})$. A $\boldsymbol{k}$-dependent gap term $M(\boldsymbol{k})\tau_2$, if turned on, will break the $\mathcal{PT}$ symmetry, yielding a Weyl semimetal or a trivial band insulator (BI).

To systematically generate different topological phases, we introduce the following gap term on top of H_{NL},

$$H_{\mathrm{gap}} = \left[M_0(\boldsymbol{k})s_0 + \sum_{i=1,2,3} M_i(\boldsymbol{k})s_i\right]\tau_2, \tag{3.2}$$

with s_0 the 2×2 identity matrix, s_i the Pauli matrices acting on another (pseudo) spin-1/2 degree of freedom. The existence of surface states of $H = H_{\mathrm{NL}} + H_{\mathrm{gap}}$ (say along z), as well as their energy dispersion, is related to H projected on a plane in the 3D BZ perpendicular to k_z [218]. Below we take advantage of this explicit bulk-edge relation to facilitate the construction of surface states localized along the z direction. To that end we consider a gap term which is independent from k_z, so that H_{gap} is only a function of $\boldsymbol{k}_\parallel = (k_x, k_y)$. Physically, $H_{\mathrm{gap}} = H_{\mathrm{gap}}(\boldsymbol{k}_\parallel)$ may describe a 2D spin-orbit coupling. The spectrum of $H_{\mathrm{gap}}(\boldsymbol{k}_\parallel)$ itself is given by $\alpha M_{\mathrm{gap},\pm}(\boldsymbol{k}_\parallel)$, where $\alpha = \pm 1$ is the eigenvalue of τ_2, and

$$M_{\mathrm{gap},\pm}(\boldsymbol{k}_\parallel) = M_0(\boldsymbol{k}_\parallel) \pm \sqrt{\sum_i M_i^2(\boldsymbol{k}_\parallel)}. \tag{3.3}$$

The dispersion relation of the total Hamiltonian $H = H_{\mathrm{NL}} + H_{\mathrm{gap}}$ can be found accordingly, which is given by

$$E = \pm\sqrt{E_{\mathrm{NL}}^2 + M_{\mathrm{gap},\pm}^2(\boldsymbol{k}_\parallel)}. \tag{3.4}$$

The surface states of $H = H_{\mathrm{NL}} + H_{\mathrm{gap}}$ under open boundary condition (OBC) along the z direction can now be analyzed from the effective Hamiltonian $H_{\mathrm{eff},\pm} = H_{\mathrm{NL}} + M_{\mathrm{gap},\pm}(\boldsymbol{k}_\parallel)\tau_2$ as a 2×2 Dirac Hamiltonian winding with k_z [212]. Because $M_{\mathrm{gap},\pm}(\boldsymbol{k}_\parallel)$ is independent of k_z, this gap term does not affect the winding behavior of $H_{\mathrm{eff},\pm}$, and hence will not play any role in determining the existence of 2D surface states. Indeed, applying the method in Ref. [218], we arrive at the following condition (see Section D.1 for details) for surface states to exist, namely,

$$|\cos k_x + \cos k_y - m| < 1. \tag{3.5}$$

Thus, surface states of H can only appear in the region bounded by the nodal loop $\boldsymbol{L}_0$ associated with the original H_{NL}. Remarkably, under this condition, the dispersion relation of the surface states is found to be precisely $\pm M_{\mathrm{gap},\pm}(\boldsymbol{k}_\parallel)$ (see Section D.2). That is, provided that surface states do exist, the 3D Hamiltonian H directly inherits the dispersion relations of its surface states from $\pm M_{\mathrm{gap},\pm}(\boldsymbol{k}_\parallel)$, the spectrum of the gap term H_{gap} itself. It is this finding that allows us to engineer below a variety of topological phases by tailoring their surface state dispersions at our will. From Equation 3.4, it is clear that when the zero-energy surface states overlap with $\boldsymbol{L}_0$, the 3D system becomes gapless.

Before moving on to the following sections of different topological phases, we would like to point out that H_{NL} in Equation 3.1 is chosen to satisfy the $\mathcal{PT}$ symmetry, which is a key factor to realizing NLSMs in many recent studies. However, in this chapter we aim to propose a method to study diverse topological phases embedded in a nodal loop structure of the system. In other words, our method works as long as the total Hamiltonian can be divided into a NLSM-like Hamiltonian which gives the nodal loop structure, and some extra terms anticommuting with the NLSM-like Hamiltonian. In a specific system, the NLSM-like Hamiltonian may take form different from H_{NL}, provided that the extra terms are revised accordingly.

3.3 Chiral insulators

As a simple case, we discuss how a chiral-symmetry-protected topological insulator [219] can be created from our approach. We set M_0 and one of the three M_i's (say M_3) to be both zero [167]. $H = H_{\mathrm{NL}} + H_{\mathrm{gap}}$ then possesses a new $\mathcal{PT}$ symmetry with $\mathcal{P}s_2H^*(\boldsymbol{k})s_2\mathcal{P}^{-1} = H(\boldsymbol{k})$, as well as a chiral symmetry with $\mathcal{S}H(\boldsymbol{k})\mathcal{S}^{-1} = -H(\boldsymbol{k})$, where $\mathcal{S} = s_3\tau_2$. In this case, the two effective Hamiltonians $H_{\mathrm{eff},\pm} = H_{\mathrm{NL}} + M_{\mathrm{gap},\pm}(\boldsymbol{k}_\parallel)\tau_2$ yield identical spectrum, implying that H is two-fold degenerate. The surface states, if they exist, should be also two-fold degenerate. Consider a specific example with

$$H_{\mathrm{gap}} = [(\sin k_x)s_2 + (\sin k_y + \mu)s_1]\,\tau_2, \tag{3.6}$$

where $M_0 = M_3 = 0$. The spectrum of H_{gap} itself represents a 2D nodal-point semimetal. When $\mu = 0$, a four-fold degenerate 2D Dirac point at $(k_x, k_y) = (0, 0)$ lies at the center of $\boldsymbol{L}_0$ in the 2D surface BZ, as shown in Figure 3.1(a). The full system $H = H_{\mathrm{NL}} + H_{\mathrm{gap}}$ inherits this dispersion relation via its surface states. As μ is tuned, the Dirac point moves around in the surface BZ. When the Dirac point falls right on $\boldsymbol{L}_0$, the bulk gap closes and the system undergoes a topological phase transition. Consistent with this, as the Dirac point leaves $\boldsymbol{L}_0$ [Figure 3.1(b)], the system becomes a trivial insulator. Due to the chiral symmetry $\mathcal{S}$, the system belongs to either AIII or DIII class, depending on whether time-reversal symmetry (TRS) is respected. In both cases, the topological properties are characterized by an invariant in $\mathbb{Z}$, e.g. a winding number assigned to the nodal loop $\boldsymbol{L}_0$,

$$\nu = \oint_{\boldsymbol{L}_0} \frac{M_1(\boldsymbol{k}_\parallel)\mathrm{d}M_2(\boldsymbol{k}_\parallel) - M_2(\boldsymbol{k}_\parallel)\mathrm{d}M_1(\boldsymbol{k}_\parallel)}{M_1^2(\boldsymbol{k}_\parallel) + M_2^2(\boldsymbol{k}_\parallel)}. \tag{3.7}$$

This winding number is equivalent to the Chern number defined on a 2D plane containing $\boldsymbol{L}_0$ [220].

As discussed in Ref. [167], the topology of a 3D topological insulator of the Bi_2Te_3 family [168] can be characterized using a similar method, since its effective Hamiltonian near the time-reversal-invariant point can be divided into a NLSM-like Hamiltonian constructed by two Dirac matrices $\gamma_1 = \tau_s s_0$ and $\gamma_2 = \tau_x s_z$, and extra terms given by $\gamma_3 = \tau_x s_x$ and $\gamma_4 = \tau_x s_y$. However, the aforementioned study only focuses on the case with two anticommuting extra terms. In this chapter, we consider more general extra terms and show that richer topological phases can be obtained, as discussed below.

3.4 Degenerate surface loop insulator and Weyl semimetal

Next we introduce a $\boldsymbol{k}$-independent $M_0(\boldsymbol{k}) = m'$, which breaks both the $\mathcal{PT}$ symmetry and the chiral symmetry mentioned above. A simple gap term of this type with $M_3 = 0$ is given by

$$H_{\text{gap}} = \left[m' + (\sin k_x)s_2 + (\sin k_y + \mu)s_1\right]\tau_2. \tag{3.8}$$

Without loss of generality, we choose $m' \geqslant 0$ hereafter. The two-fold degenerate spectrum of the chiral insulator is lifted, so is the four-fold degenerate surface Dirac

[1]The sketches are only for small m and m', so that $\boldsymbol{L}_0$ and the DSL are both nearly perfect circles. In general, the zeros of H_{gap} give four closed loops in the surface Brillouin zone when $\mu = 0$. For larger m', each two of these loops will merge into one loop when increasing μ. Nevertheless, the topology and the structure of surface states are hardly affected, and the transition from a DSL insulator to a trivial insulator through a nodal point semimetallic phase still exists.

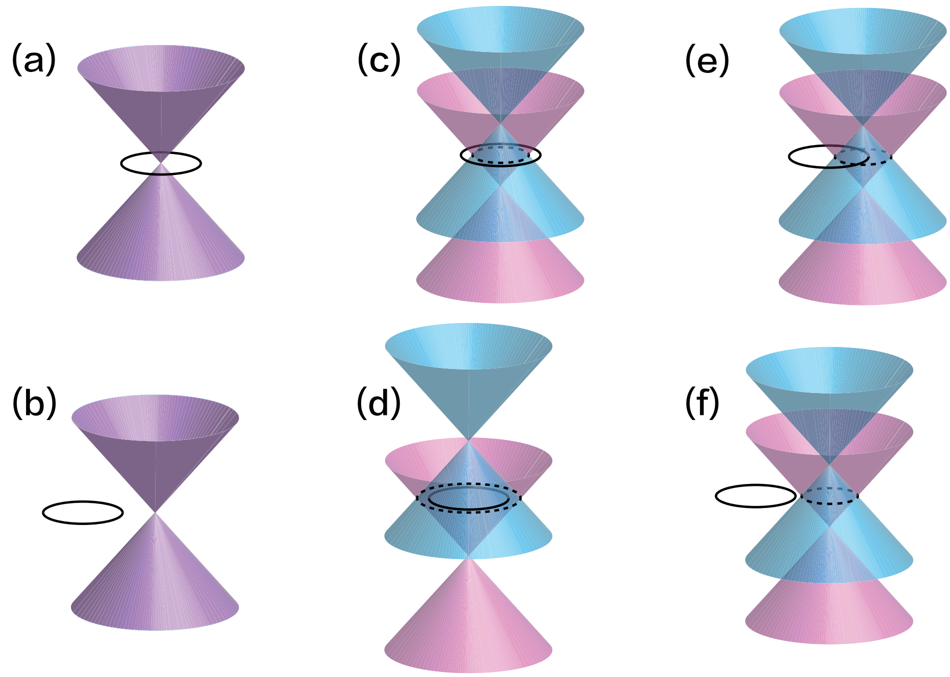

Figure 3.1: Sketches of surface Dirac cones inherited by $H = H_{\mathrm{NL}} + H_{\mathrm{gap}}$ from H_{gap} and the nodal loop $\boldsymbol{L}_0$ (black solid lines) of H_{NL}. Dashed lines represent the DSL obtained from the zero solution in Equation 3.3. A DSL exists only if it lies within the regime enclosed by $\boldsymbol{L}_0$. The Dirac cones in (a) and (b) are two-fold degenerate, whereas this degeneracy is lifted in (c)-(f) by a nonzero m'.[1]

point. Indeed, focusing on the spectrum of H_{gap}, the mere effect of a nonzero but constant $M_0 = m'$ is to shift its Dirac cones by $\pm m'$ in energy, which results in a gapless loop at zero energy as shown by the dashed lines in Figure 3.1(c)-(f). According to our general insights above, this feature is now carried over to the surface states of H and so we have degenerate surface zero modes along a 1D loop. Hence, by tuning the magnitude of m', one can engineer the size of the degenerate surface loop (DSL). We stress that the DSL is robust unless it falls outside of $\boldsymbol{L}_0$ in the surface BZ [Figure 3.1(c) and (d)]. We also note in passing that DSL here is protected by the symmetry

$$\mathcal{C}H^*(\boldsymbol{k})\mathcal{C}^{-1} = -H(\boldsymbol{k}), \tag{3.9}$$

with $\mathcal{C} = s_1\tau_2$. Such a symmetry is a combination of parity and particle-hole symmetries [79], which is ensured by $M_3 = 0$, namely, the absence of $s_3\tau_2$ in Equation 3.8.

Further, a nonzero μ in H_{gap} depicted in Equation 3.8 shifts the DSL center, yielding more topological phases [Figure 3.1(e) and (f)] as we tune μ. Indeed, as the DSL center moves and touches $\boldsymbol{L}_0$, the spectrum of $H = H_{\text{NL}} + H_{\text{gap}}$ becomes gapless and a topological phase transition occurs. Specifically, one finds the following gap closing conditions,

$$\begin{aligned} &k_z = 0, \quad \cos k_x + \cos k_y - (m-1) = 0, \\ &\sin^2 k_x + (\sin k_y + \mu)^2 = (m')^2. \end{aligned} \tag{3.10}$$

For $m = 2$, H describes an insulator with DSL under the condition $\mu + m' < 1$, and a trivial band insulator otherwise.

Because the winding number ν defined in Equation 3.7 is unrelated to $M_0(\boldsymbol{k}_\parallel) = m'$, and yet changing m' can close the bulk gap, we see that the topological invariant ν does not suffice to characterize different types of insulator phases with DSL. To find a second topological invariant, we return to the effective Hamiltonians $H_{\text{eff},\pm} = H_{\text{NL}} + M_{\text{gap},\pm}(\boldsymbol{k}_\parallel)\tau_2$ defined earlier. The two effective Hamiltonians $H_{\text{eff},\pm}$ depict a nodal-loop semimetal H_{NL} subject to a gap term $M_{\text{gap},+}(\boldsymbol{k}_\parallel)\tau_2$ or $M_{\text{gap},-}(\boldsymbol{k}_\parallel)\tau_2$. In either case, the surface loop due to $M_{\text{gap},+}(\boldsymbol{k}_\parallel)\tau_2$ or $M_{\text{gap},-}(\boldsymbol{k}_\parallel)\tau_2$ alone is not protected by a bulk gap because it can shrink to a point and disappear altogether without closing the bulk gap of $H_{\text{eff},\pm}$. However, our DSL phase must be described by the two effective Hamiltonians at the same time. Indeed, what is protected by a nonzero bulk gap is the intersection of the two pairs of surface Dirac cones, given by $\alpha M_{\text{gap},\pm}$ with $\alpha = \pm 1$ respectively. This motivates us to seek a topological invariant based on both surface

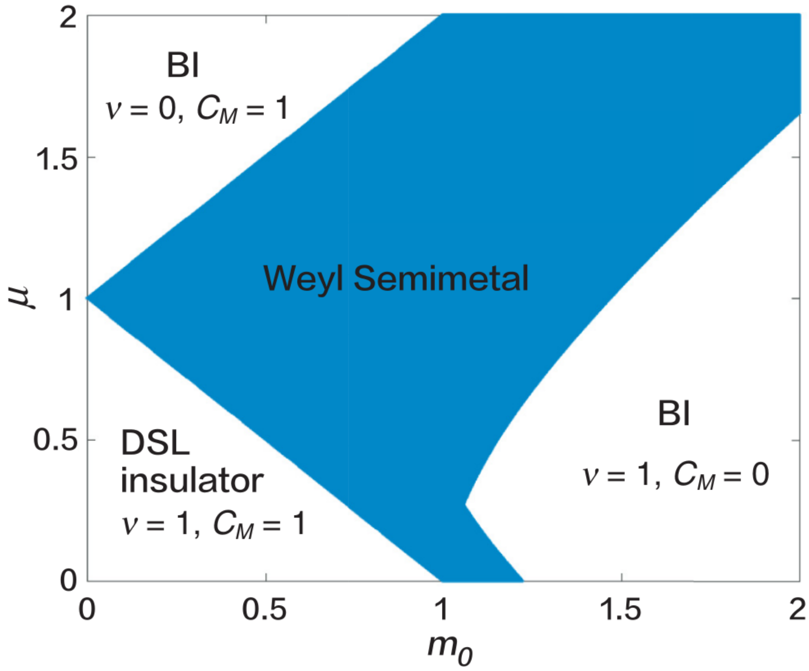

Figure 3.2: A topological phase diagram with $m = 2$, with the phase boundary determined from Equation 3.10. Different insulating phases are characterized by two topological invariants ν and C_M defined in the main text, which are ill-defined in the semimetallic NPSM phase.

Dirac cones. Specifically, consider the Berry curvature along the loop $\boldsymbol{L}_0$,

$$\boldsymbol{V}_{\pm}^{\boldsymbol{L}_0} = \boldsymbol{\nabla}_{\boldsymbol{k}} \times \boldsymbol{A}_{\pm}^{\boldsymbol{L}_0} = \frac{\mathrm{sgn}(M_{\mathrm{gap},\pm}^{\boldsymbol{L}_0})}{4\pi |M_{\mathrm{gap},\pm}^{\boldsymbol{L}_0}|^2} (\sin k_y, -\sin k_x, 0), \tag{3.11}$$

with $\boldsymbol{A}_{\pm}^{\boldsymbol{L}_0}$ being the Berry connection on the lower band of Hamiltonians $H_{\mathrm{eff},\pm}$, evaluated along $\boldsymbol{L}_0$. So long as the bulk is gapped, $M_{\mathrm{gap},+}(\boldsymbol{k}_\parallel)$ and $M_{\mathrm{gap},-}(\boldsymbol{k}_\parallel)$ must be nonzero along $\boldsymbol{L}_0$, and hence cannot change their respective signs. Thus, either the Berry curvatures $\boldsymbol{V}_{+}^{\boldsymbol{L}_0}$ and $\boldsymbol{V}_{-}^{\boldsymbol{L}_0}$ always point in the same direction along the loop $\boldsymbol{L}_0$, or they always point in the opposite direction along the loop $\boldsymbol{L}_0$. Such a binary feature can be captured by the integer

$$C_M = [\mathrm{sgn}(M_{\mathrm{gap},+}^{\boldsymbol{L}_0}) - \mathrm{sgn}(M_{\mathrm{gap},-}^{\boldsymbol{L}_0})]/2, \tag{3.12}$$

where $C_M = 0$ for the first and $C_M = 1$ for the latter case. Consider now $m' = 0$ (which yields $C_M = 1$). For each fixed k_x, k_y on the nodal loop $\boldsymbol{L}_0$, $M^{\boldsymbol{L}_0}_{\text{gap},-}$ increases with m', and changes sign after the DSL intersects $\boldsymbol{L}_0$ (and then the DSL vanishes as m' is further increased). This topological phase transition is captured by a jump in C_M from $C_M = 1$ to $C_M = 0$. On the other hand, changing μ can move the DSL center out of the loop $\boldsymbol{L}_0$, thus turning the DSL insulator into a trivial BI without affecting C_M. Thus both ν and C_M are needed to characterize the topological properties of gapless surface states. A full phase diagram based on this insight as well as the conditions listed in Equation 3.10 is presented in Figure 3.2. In the (blue) shaded region of Figure 3.2, the DSL and $\boldsymbol{L}_0$ touch at discrete points, yielding a NPSM (Weyl) semimetal. That there is no fine-tuning needed for the NPSM phase can also be understood by inspecting the ways for $\boldsymbol{L}_0$ and the DSL to touch, which span a continuous parameter regime. The Fermi arcs connecting different Weyl points are given by the portion of the DSL that stays inside $\boldsymbol{L}_0$, as illustrated in Figure 3.1(e). Since the calculations of both ν and C_M require a nonzero gap along $\boldsymbol{L}_0$, they are not defined in the NPSM phase.

In Figure 3.3 we present the zero-energy modes with open boundary condition (OBC) along the z direction, and their corresponding bulk spectra. The zero-energy surface states form a single point, a closed ring, or one or several arcs in the surface BZ [Figure 3.3(a1)-(d1)], corresponding to a 3D chiral insulator, a DSL insulator, or a Weyl semimetal respectively. In Figure 3.3(d) there are four Fermi arcs connecting eight Weyl oints. This is because for $\mu = 0$, although both the DSL and $\boldsymbol{L}_0$ are centered at $k_x = k_y = 0$, neither of them is a perfect circle, and they cannot fully overlap. Instead, the DSL and the loop $\boldsymbol{L}_0$ cross each other at multiple Weyl points in the momentum space. By tuning parameters, these Weyl points can move in the BZ and annihilate with each other, while the Fermi arcs may shrink into points and disappear, or extend into

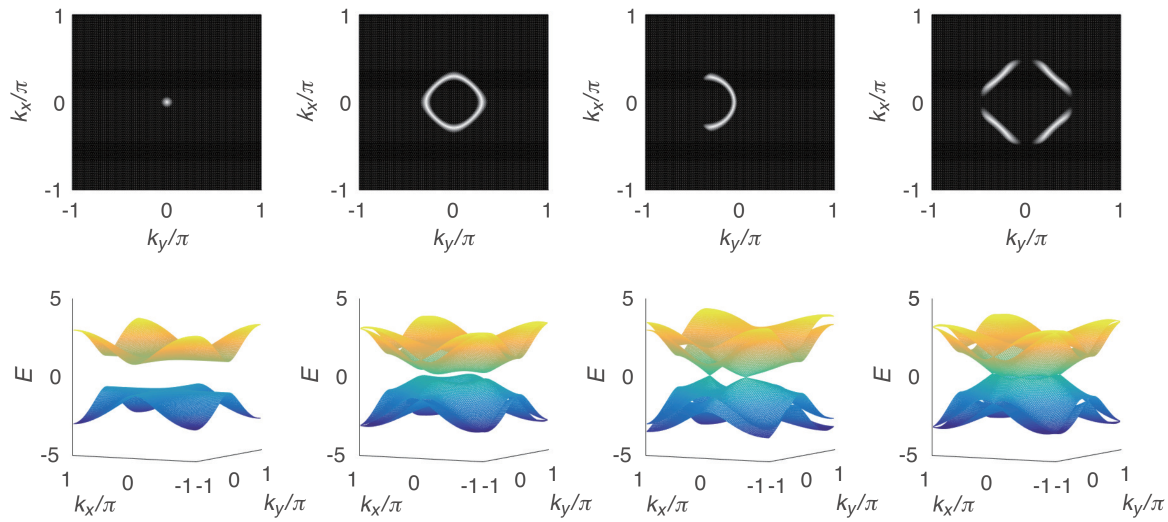

Figure 3.3: The surface zero modes with $m = 2$, and their corresponding bulk spectra with $k_z = 0$ in (a2)-(d2). The zero modes are indicated by the bright markers in (a1)-(d1). The parameters are (a) $m' = 0$, $\mu = 0$; (b) $m' = 0.8$, $\mu = 0$; (b) $m' = 0.8$, $\mu = 1$; (d) $m' = 1.1$, $\mu = 0$.

a closed loop as in the DSL insulator phase, depending how the transition-associated parameter varies. These processes describe transitions between a Weyl semimetal to a trivial insulator or a topological one respectively, and the latter has been predicted in the material Ta_3S_2 [221].

3.5 Second-order insulators

As the final topological phase created by our general approach, we consider a nonzero $M_3(\boldsymbol{k}_\parallel)$. In this case, H_{gap} itself in general depicts a 2D insulating system that can be topologically nontrivial. The presence of the $s_3\tau_2$ term in $H = H_{\text{NL}} + H_{\text{gap}}$ breaks the symmetry $\mathcal{C}$ previously discussed, and as a result the 2D surface states are fully gapped.

As an example, we consider

$$H_{\text{gap}} = [\sin k_x s_2 + \sin k_y s_1 + (\mu' - \cos k_x - \cos k_y)s_3]\,\tau_2. \tag{3.13}$$

H_{gap} above is similar to a Chern insulator model [20], with two topologically nontrivial phases for $-2 < \mu' < 0$ and $0 < \mu' < 2$, with a 2D Chern number $C = \pm 1$. For $|\mu'| > 2$, H_{gap} itself describes a 2D trivial BI. Below we only consider positive values of μ'.

The surface states of H under OBC along z, which inherit their dispersion relations from that of H_{gap}, should be fully gapped in the 2D k_x–k_y surface BZ. Because H_{gap} itself can be topologically nontrivial, it is anticipated that upon opening another direction, gapless edges can emerge. This is confirmed in Figure 3.4(c), where we show the spectrum versus k_y, with OBCs in both x and z. We observe gapless states localized in the 1D edges of a 3D sample along the y direction for $1 < \mu' < 2$, thus realizing a second-order topological insulator [35, 216, 217], a subject of great interest recently. Such intriguing "edge states of surface states" are obtained here using exactly the same philosophy as how we engineer other interesting topological phases discussed above.

We now explain the criterion ($1 < \mu' < 2$) for the generation of a second-order topological insulator. Following [220], we consider the gap term as a 2D nodal loop semimetal, $(\mu' - \cos k_x - \cos k_y)s_3$, gapped by $\sin k_x s_2 + \sin k_y s_1$. The topological property of H_{gap} can then be characterized by a chirality assigned to the 2D loop $\boldsymbol{l}_0 : \cos k_x + \cos k_y = \mu'$. Hence, for this nontrivial topology to manifest as surface states of the 3D system H, the parent 3D loop $\boldsymbol{L}_0$ must be able to capture the chirality of $\boldsymbol{l}_0$, i.e. $\boldsymbol{L}_0$ must enclose $\boldsymbol{l}_0$, whence the condition $\mu' > 1$. To understand the upper bound, it suffices to notice that, for $\mu' > 0$, the gap term H_{gap} admits non-zero Chern number only if $\mu' < 2$.

It has been argued that crystal symmetries, e.g. reflection symmetries [35, 216] or the combination of a C_4 rotation symmetry and the TRS [217], play crucial roles in the existence of higher-order topological phases when OBCs are chosen in directions that respect the symmetries. In our model, the TRS is already broken in H_{NL}, and the chiral symmetry is broken when H_{gap} of Equation 3.13 is introduced. It is important that H_{gap} breaks the chiral symmetry of H_{NL} without destroying its winding with k_z, because then the topological nature of H_{gap} will determine the topological nature of the surface spectrum. Therefore our system falls in class A of the ten-fold way of symmetry classification [79], which has been discussed in Ref. [216]. In contrast to their reflection-symmetric second-order topological phases, our model satisfies anti-reflection symmetries in all three directions, i.e.

$$\mathcal{R}_i H_{\mathrm{HO}}(k_i)\mathcal{R}_i^{-1} = -H_{\mathrm{HO}}(-k_i), \tag{3.14}$$

with $i = x$, y or z, H_{HO} the total Hamiltonian of our second-order insulator, $\mathcal{R}_x = s_2\tau_2$, $\mathcal{R}_y = s_1\tau_2$, and $\mathcal{R}_z = \tau_3$. On the other hand, our system has a $\mathcal{C}_4$ rotation symmetry, as

$$\mathcal{C}_4^z H_{\mathrm{HO}}(k_x, k_y, k_z)(\mathcal{C}_4^z)^{-1} = H_{\mathrm{HO}}(-k_y, k_x, k_z), \tag{3.15}$$

where $\mathcal{C}_4^z = \tau_0 \exp\{-\mathrm{i}\pi s_z/4\}$. In comparison, our numerical results show no surface states when OBC is taken in any of the three directions, while hinge states exist only for OBCs taken in z direction and one of the rest two direcitons, as long as the system falls into a topologically nontrivial phase ($1 < \mu' < 2$).

3.6 Transport properties

To conclude our study, we now examine how the surface states in each class of topological phase may lead to different transport properties. We consider a 3D sample

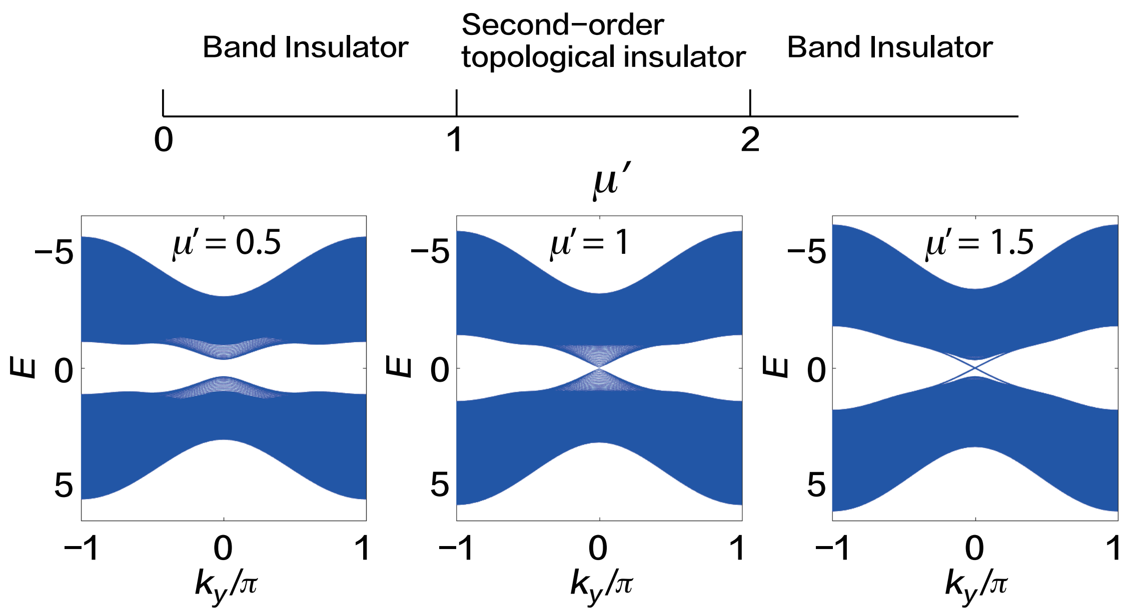

Figure 3.4: Spectrum versus k_y with open boundary condition in x and z directions, for the gap terms as in Equation 3.13. The parameters are $m = 2$, and $\mu' = 0.5, 1, 1.5$ for the three panels, respectively.

of our model with metallic leads (in the wide band limit) attached along the y direction, and computationally investigate the differential conductance T (in units of e^2/h) using the Caroli formula [222]: $T(E_F) = \mathrm{Tr}[G\Gamma_R G^\dagger \Gamma_L]$. Here E_F is the Fermi energy, $G = (E_F - H - \Sigma_L - \Sigma_R)^{-1}$ is the retarded Green's function, $\Sigma_{L/R}$ is the self energy due to the left (right) lead (taken in the wideband limit $\Sigma_{L/R} = -i\delta_{ss'}\delta_{\tau\tau'}\delta_{ij}/2$ for simplicity), $\Gamma_{L/R} = i(\Sigma_{L/R} - \Sigma_{L/R}^\dagger)$ is the line-width function, and $\mathrm{Tr}[\dots]$ is a trace over both the spin and pseudospin subspaces. For efficient simulations of large systems we employ the method of recursive Green's functions [197] which reduces the complexity from $O(N_x^3 N_y^3 N_z^3)$ to $O(N_x^3 N_y N_z^3)$.

In Figure 3.5(a) we illustrate T versus Fermi energy E_F for the four topological phases engineered from our general approach. For the chiral topological insulator, as E_F increases, the Fermi surfaces evolve from a point at $E_F = 0$ to loops of sizes proportional to E_F. Beyond a transition point at $E_F \sim 1$, one eventually arrives at the bulk bands and expects much larger conductance. The corresponding conductance behavior agrees with these insights. For the Weyl semimetal phase, the system is always metallic for finite E_F, which is reflected by the steady increase of the conductance. For the DSL insulator, it is curious to see that the conductance first stays around a certain value. This is because as E_F increases, the Fermi surface intersects with two Dirac cones, resulting in two 1D loops, one increasing in size and the other decreasing in size. As E_F continues to increase, the surface states merge into the bulk ($E_F \sim 0.25$), where the system becomes metallic and the conductance increases at a much faster rate. For the second-order topological insulator, we observe two transitions in the conductance. For $E_F \lesssim 0.4$, the plateau of T is due to the 1D surface states along the hinges, which are similar to the surface states of a 2D Chern insulator. For $0.4 \lesssim E_F \lesssim 1$, gapped surface states start to contribute and conductance increases with E_F. Finally, $E_F \gtrsim 1$ corresponds to bulk spectrum and the conductance also becomes that of a metal. Like in other cases, these transition values of E_F are in good agreement with our numerical results based on the system spectrum alone.

Since the DSL insulator and Weyl semimetal phases share similar conductance behavior as shown in Figure 3.5(a), we consider the responses of these two topological phases to disorder so as to distinguish between them. In Figure 3.5(b), we look into the conductance T as a function of μ, for a sample with on-site disorder, diagonal in both s and τ space, uniformly distributed in $[-W, W]$. We set $m' = 0.8$ and the Fermi energy $E_F = 0$. As discussed above, tuning μ induces a transition from a DSL insulator to a Weyl semimetal. Consistent with this, the Weyl semimetal for $(0.4 \lesssim \mu \lesssim 1.5)$ exhibits robust quantized plateaux due to the quantum anomalous Hall effect along the

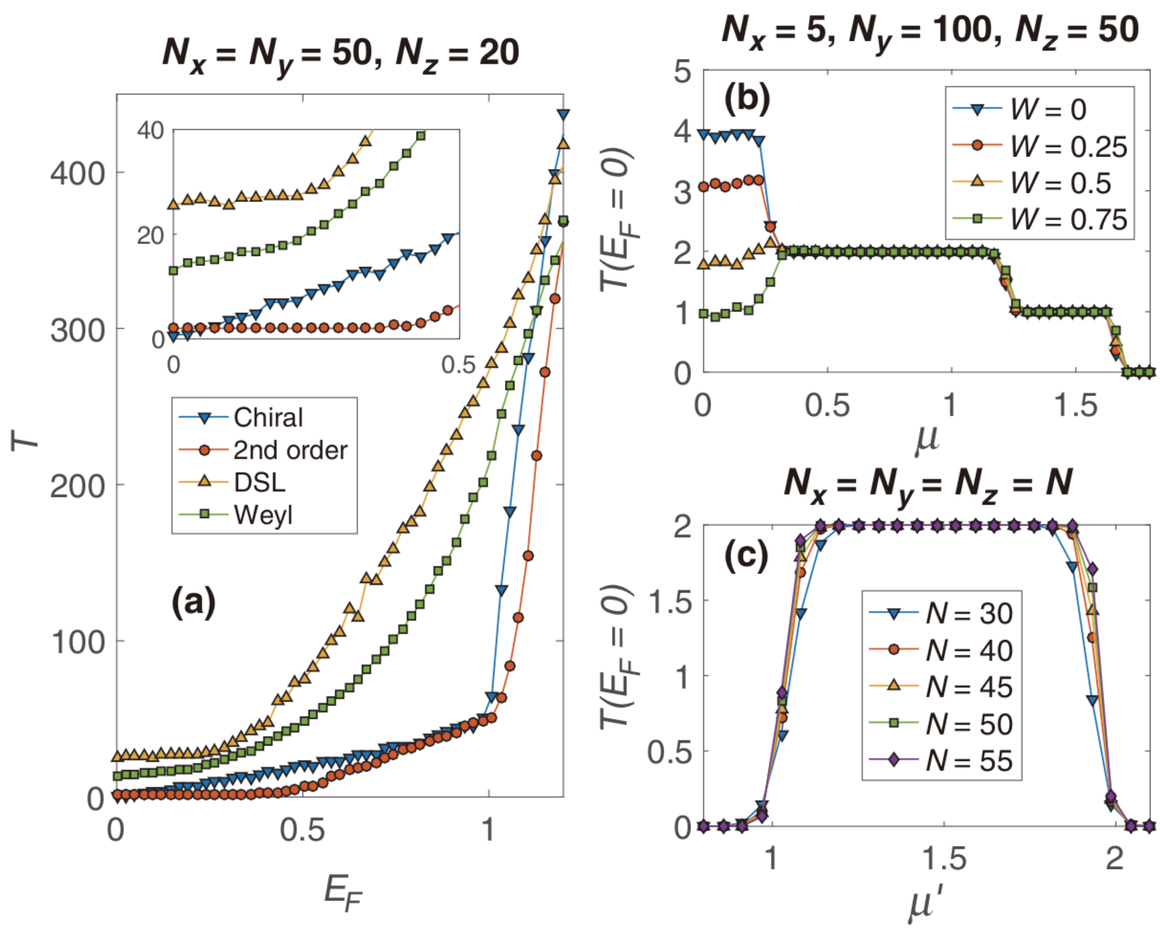

Figure 3.5: (a) Conductance T vs Fermi energy E_F for four topological phases. Inset zooms in to $0 < E_F < 0.5$. (b) T versus μ at $E_F = 0$ for a disordered sample with different strengths W, with the gap term given by Equation 3.8 and $m' = 0.8$, averaged over 100 disorder realizations. For small μ', the system is an insulator with DSL and T is not robust. For larger μ', the system is a Weyl semimetal and the conductance is robust and quantized due to edge state conductance on the Fermi arc. (c) T versus μ' at $E_F = 0$, for a second-order topological insulator using the gap term defined in Equation 3.13, with parameters $m = 2, m' = 1.5$. The transitions at $\mu' = 1$ and $\mu' = 2$ agree with our theory.

Fermi arc connecting the Weyl points [223]. By contrast, the DSL phase is not resistant against disorder, as reflected by the curves in the leftmost part of Figure 3.5(b). This is justified since the disorder we apply is diagonal in both s and τ space, and the presence of $s_0\tau_0$ violates the symmetry (Equation 3.9) needed to protect the DSL.

Finally, we verify the criterion for the existence of second-order topological insulator. We set $m = 2$ as in Figure 3.4 for the gap term given by Equation 3.13. Figure 3.5(c) presents the conductance at $E_F = 0$ as a function of μ'. The plateau due to the hinge states is clearly observed. The phase transition points are identified at $\mu' = 1$ and $\mu' = 2$, in agreement with our previous discussion. The transition becomes more pronounced as the sample size N increases.

Chapter 4

Photoinduced half-integer quantized conductance plateaus in topological-insulator/superconductor heterostructures

4.1 Preliminaries

The search for excitations with Majorana-like properties in solid state systems is an active ongoing research topic [224]. A vast majority of efforts focuses on zero-dimensional Majorana bound states (MBS) at the ends of proximitized semiconductor nanowires [93, 104] or magnetic atom chains on superconductor substrates [105]. Another candidate in the race is the one-dimensional chiral Majorana edge modes (CMEM) on the surface of topological superconductors [87] (TSC). Recently, transport measurements [94] have been carried out in magnetic topological insulator (TI) thin films proximitized by s-wave superconductor. Half-quantized conductance plateaus were identified and interpreted as the signature of the existence of a pair of CMEM, a conclusion which has sparked vivid debates [98, 99] and inspired a number of stimulating follow-up studies [225, 226].

Such intense attention is not unwarranted for: Majorana zero modes hold promising prospects for topological quantum computation (TQC) [227], and their discovery should demonstrate the ability of table-top experiments in simulating fundamental particles not yet found in nature. With such far-reaching impacts, the pursuit of Majorana fermions naturally spans beyond the realm of solid state materials. Be it on cold atom systems [228] or photonic lattices [229], proposals towards the realizations of Majorana fermions are regularly put forward.

A recurring theme among these approaches is the manipulation of electromagnetic waves. Indeed, the revelation that light can interact with matter and give rise to nontrivial Floquet-Bloch states [113] has propelled our understanding of topological phases [165] and opened up a new avenue in the conception of novel topological matter [230]. From the surge of research activities emerges the field of Floquet topological phases [115], and rightfully so: Not only do they exhibit unusual bulk-edge correspondence with no static analog [206], the tunability of periodic driving fields also allows the generation of intriguing phases with large topological invariants [166]. Of course, ingenious engineering finds its way also in non-optical settings. Concepts of Floquet topological phases have since been extended to acoustic or mechanical systems [231, 232].

In the context of superconductors, Floquet systems have an additional bonus: Because of the torus topology of the Floquet-Brillouin zone, there is no distinction between quasienergies $\epsilon = \pm\hbar\Omega/2$ (Ω being the frequency of a periodic drive). Thus zero energy no longer reigns supreme, because excitations γ obeying the Majorana condition ($\gamma^\dagger = \gamma$) [233] can now be sought at quasienergy $\epsilon = \pm\hbar\Omega/2$ as well. In the literature, most studies have so far concentrated on dissecting the topological features [169]. While the transport properties of driven one-dimensional systems hosting MBS have also been investigated [186], studies on the quantum transport of two-dimensional

Floquet topological superconductors [234] are still scarce, not to mention the possible quantization signature of Floquet CMEMs.

Motivated by the importance of active manipulation of CMEMs, as well as the fascinating interplay between light-matter interaction and topology, we investigate the possibility of creating and detecting Floquet CMEMs in hybrid topological devices, which consist of a Floquet topological superconductor (FTSC) sandwiched between two Floquet Chern insulators (FlCI). In the literature, this type of heterostructures (without the time-periodic modulation) was studied in Refs. [94, 96], which established theoretically and experimentally that the existence of CMEM in the TSC implies half-quantized longitudinal conductance plateau. Naturally, it is tempting to ask: What happens when more than a single pair of CMEMs are present in the TSC? Do Floquet CMEMs exhibit half-integer conductance plateaus? If so, is there any additional constraint and why must it be satisfied? If there is a constraint, can one observe any sign hinting at the existence of photoinduced CMEM even if the constraint is not met? Practically, how can one model a periodically driven heterostructure, given that the left and right parts may serve either as leads or parts of the sample? In this chapter, we tackle the above questions, in part building on previous works on the Floquet sum rule [186].

Our main results are twofold: (a) the numerical observations of conductance plateaus at $\frac{1}{2}\frac{e^2}{h}$ and $\frac{3}{2}\frac{e^2}{h}$ (upon invoking the Floquet sum rule [186]), due to photoinduced CMEMs in a driven junction, and (b) the finding that in a FlCI-FTSC-FlCI hybrid device, if there is a conductance plateau, then for all Floquet sidebands, the normal and Andreev processes always share equal probabilities. While the conductance of a homogeneous sample is expected to scale up according to the number of edge modes, whether this remains the case for a heterostructure is a priori unclear, because the edge states may interfere with each other in coherent transport. The presence of periodic drives render the situation even more uncertain. Indeed, by irradiating a QAHI-TSC-QAHI sample with high-frequency light, one observes suppressed DC conductance, which might suggest some sort of light-induced interference. Here, it is shown, by means of extensive numerical results, that the nontrivial topology of an irradiated junction may still be probed by DC conductance, the value of which will be quantized upon summing over Floquet sidebands. Even without such a summation, one still observes equal Andreev-normal scattering coefficients at each sideband, implying that for photoinduced CMEMs, the property of being equal superpositions of electrons and holes extends to all Floquet sidebands.

The half-quantized conductance plateaus discovered in this work are found to be robust against static and time-periodic disorder. They are rather subtle because they emerge only after summing over contributions from all Floquet sidebands. They can thus serve as a hallmark of photoinduced CMEMs in topological insulator-superconductor junctions. In particular, the conductance plateau at $\frac{3}{2}\frac{e^2}{h}$ marks the existence of three pairs of CMEMs, indicating a possible way to simultaneously create, detect, and manipulate multiple pairs of CMEMs by light. Because to our knowledge the $\frac{3}{2}\frac{e^2}{h}$ conductance plateaus have not yet been computationally or experimentally observed in any other superconducting system, their experimental realization will be a ground-breaking progress. To that end we shall briefly discuss cold-atom systems as one possible platform to experimentally explore photoinduced CMEMs. In passing, we also elaborate on a few other aspects of transport in Floquet topological junctions. For example, we argue that in a driven device, to probe the topology by means of transport, one must also cover the two sandwiching systems by light irradiation, but not treat them as leads. These results offer more insights into the pursuit of Majorana fermions and contribute to the general understanding of transport in Floquet hybrid devices. Recently, controlling Majorana modes by magnetic writing [235], and the verification of the non-Abelian statistics of Majorana modes [236] by electrical transport have been proposed. Along the same line, we hope that the present work will further stimulate interests on class D topological superconductors in two dimension. The experimental breakthrough in Ref. [94] demonstrated that it is possible to meticulously design heterostructures for fractionalized excitations to not only emerge but also directly manifest via half-quantized conductance. Hence, in a larger context, our theoretical study illustrates that, in principle, similar approaches may also extend to optoelectronics.

This chapter is structured as follows. In Section 4.2, we propose system Hamiltonians and driving protocols modeling certain time-periodic modulations such as light-matter interaction. Various junctions consisting of FlCI and FTSC are thus constructed. In Section 4.3 we briefly discuss the DC conductance that is used to probe the topological edge states in this chapter. Section 4.4 presents our main findings on conductance plateaus with detailed supporting results, including the effects of disorder. In Section 4.5, we elaborate on several aspects of quantum transport in Floquet topological hybrid devices. In Appendix E, we outline some aspects of the transport theory of superconducting systems.

4.2 Models

We study the two-terminal quantum transport of hybrid structures consisting of a superconductor sandwiched between two [left/right (L/R)] Chern insulators, detailed below, that are attached to two metallic leads (Fig. 1). The entire sample is periodically driven at the same fundamental frequency Ω, such that Floquet theory applies, although

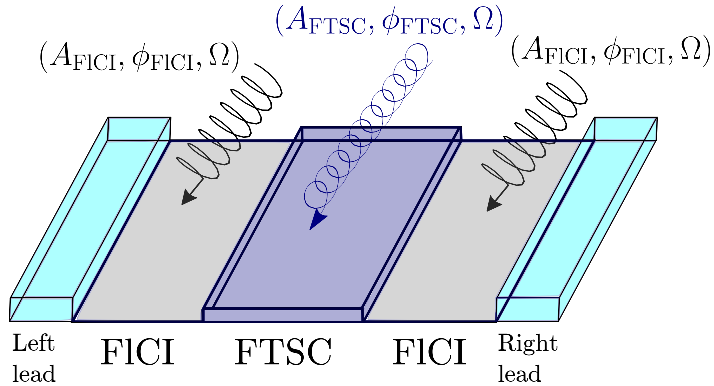

Figure 4.1: Schematic of the model studied in this chapter. The sample is composed of a Floquet topological superconductor, sandwiched between two Floquet Chern insulators which are attached to two leads. Continuous driving fields are characterized by the amplitudes $(A_{\mathrm{FlCI}}, A_{\mathrm{FTSC}})$, and polarization angles $(\phi_{\mathrm{FlCI}}, \phi_{\mathrm{FTSC}})$ for the left/right Floquet Chern insulators and the central superconductor. The frequency Ω is set to be homogeneous throughout the heterostructure.

the amplitudes of driving fields themselves need not be homogeneous throughout the sample.

The central (C) superconducting region is described by a noninteracting Hamiltonian h_{C}, proximitized by an s-wave superconductor of pairing strength Δ. The two Chern insulators on its left and right are described by noninteracting Hamiltonians $h_{\mathrm{L/R}}$. In the Bogoliubov-de Gennes (BdG) formalism, the left/central/right Hamiltonians in momentum space read $\mathcal{H}_{\mathrm{L/C/R}} = \frac{1}{2}\sum_{\boldsymbol{k}} \Psi_{\boldsymbol{k}}^{\dagger} H_{\mathrm{L/C/R}}(\boldsymbol{k})\Psi_{\boldsymbol{k}}$, with:

$$H_{\mathrm{L/R}}(\boldsymbol{k}) = \begin{bmatrix} h_{\mathrm{L/R}}(\boldsymbol{k}) & 0 \\ 0 & -h^{*}_{\mathrm{L/R}}(-\boldsymbol{k}) \end{bmatrix},\ H_{\mathrm{C}}(\boldsymbol{k}) = \begin{bmatrix} h_{\mathrm{C}}(\boldsymbol{k}) & -\mathrm{i}\Delta\sigma_y \\ \mathrm{i}\Delta\sigma_y & -h^{*}_{\mathrm{C}}(-\boldsymbol{k}) \end{bmatrix}, \tag{4.1}$$

where $\sigma_{x,y,z}$ are the Pauli matrices in sublattice or spin space, and the Nambu spinor $\Psi_{\boldsymbol{k}} = (\hat{c}_{\boldsymbol{k},\uparrow}, \hat{c}_{\boldsymbol{k},\downarrow}, \hat{c}^{\dagger}_{-\boldsymbol{k},\uparrow}, \hat{c}^{\dagger}_{-\boldsymbol{k},\downarrow})^{\mathrm{T}}$, where $\hat{c}_{\boldsymbol{k},s}$ is the annihilation operator for an electron at momentum $\boldsymbol{k}$ with spin $s(=\uparrow,\downarrow)$. Since we study junctions, in actual calculations the Hamiltonians are discretized on a lattice in real space. When the driving fields are switched on, the left and right Hamiltonians describe the same Floquet Chern insulators, whereas the central Hamiltonian describes the Floquet topological superconductor. Below, we shall describe two specific choices for our static Chern insulator Hamiltonians $h_{\mathrm{L/R}}$, as well as two specific Floquet driving protocols (time modulations). These prototypical choices capture the essential properties of generic Chern insulators and Floquet drivings, and will be used to generate our results in Section 4.4(A–D).

4.2.1 Static Hamiltonians

We choose either the Haldane [10] or the QWZ [20] model as two prototype systems. We split the system into three regions (left/center/right), and turn on s-wave superconductivity in the central part. For ease of presentation, we write the Hamiltonians in momentum space, but in actual calculations we always work in real space with open boundary conditions.

4.2.1.1 Haldane model

The Haldane model is the first proposed model for a quantum anomalous Hall insulator (QAHI), and was recently realized with ultracold fermions in an optical lattice [237]. It consists of non-interacting electrons on a honeycomb lattice, with time reversal symmetry broken via phases in the second neighbor hoppings that simulate a magnetic vector potential. It is expressed as the Hamiltonian $h_{\mathrm{H}}(\boldsymbol{k}) = \boldsymbol{f}(\boldsymbol{k}) \cdot \boldsymbol{\sigma}$, where:

$$
\begin{aligned}
f_x(\boldsymbol{k}) &= t_1[1 + \cos(\boldsymbol{k} \cdot \boldsymbol{a}_1) + \cos(\boldsymbol{k} \cdot \boldsymbol{a}_2)], \\
f_y(\boldsymbol{k}) &= t_1[\sin(\boldsymbol{k} \cdot \boldsymbol{a}_1) + \sin(\boldsymbol{k} \cdot \boldsymbol{a}_2)], \\
f_z(\boldsymbol{k}) &= 2t_2 \sin\Phi \Big\{ \sin(\boldsymbol{k} \cdot \boldsymbol{a}_1) - \sin(\boldsymbol{k} \cdot \boldsymbol{a}_2) - \sin[\boldsymbol{k} \cdot (\boldsymbol{a}_1 - \boldsymbol{a}_2)] \Big\}.
\end{aligned}
\tag{4.2}
$$

Here, $t_{1,2}$ are the first and second neighbor hopping parameters, Φ is a phase factor, $\boldsymbol{a}_1 = \sqrt{3}\hat{\boldsymbol{x}}, \boldsymbol{a}_2 = (\sqrt{3}\hat{\boldsymbol{x}} + 3\hat{\boldsymbol{y}})/2$ are the primitive vectors of honeycomb lattice with zigzag edge, a geometry chosen for convenience.

4.2.1.2 Qi-Wu-Zhang (QWZ) model

The QWZ model is another classic two-band Chern insulator (CI) model with Chern numbers ± 1. Also known as the lattice Dirac model, it is arguably the most local CI model which is symmetric in both momenta. Due to its elegant simplicity, it has also been employed in describing (half) of the Bernevig-Hughes-Zhang model for quantum spin Hall effect in CdTe/HgTe heterostructure [39]. Its Hamiltonian is given by:

$$h_{\mathrm{QWZ}}(\boldsymbol{k}) = A \sin k_1 \sigma_x + A \sin k_2 \sigma_y + \Big[m + 4B(\cos k_1 + \cos k_2)\Big]\sigma_z, \tag{4.3}$$

where m, A, B are tunable material parameters.

4.2.2 Periodic drives

With the static heterostructure described by either of the Hamiltonians above, we further subject them to driving fields. The effect of driving fields amounts to adding a periodic time dependence to the Hamiltonians. In the following, we discuss two types of driving protocols: continuous drive by elliptically polarized light and periodic quenches.

4.2.2.1 Continuous driving field

For continuously driven models, the Hamiltonians are modified by Peierls' substitution, $\boldsymbol{k} \mapsto \boldsymbol{k} + e\boldsymbol{A}(t)$, where $-e < 0$ is the electron charge, $\boldsymbol{A}(t)$ is the vector potential. On honeycomb lattices, we take the driving fields to be of the form

$$\boldsymbol{A}(t) = A\Big[\sin(\Omega t)\boldsymbol{a}_1 + \sin(\Omega t + \phi)\boldsymbol{a}_2\Big], \tag{4.4}$$

where ϕ is an angle characterizing the rotating electromagnetic waves.

4.2.2.2 Periodic quenches

A quench is an abrupt transition of a physical system. It is widely employed in experiments to study thermalization, localization, and nonlinear dynamics. When two quenches are periodically alternated, one obtains a two-cycle quench model, described by:

$$H(t) = \begin{cases} h^{(1)}, & 0 < t < T_1 \qquad\qquad \bmod \mathcal{T}, \\ \\ h^{(2)}, & T_1 < t < T_1 + T_2 \quad \bmod \mathcal{T}, \end{cases} \tag{4.5}$$

where $\mathcal{T} = T_1 + T_2 = 2\pi/\Omega$ is the period. In Section 4.4.1, Section 4.4.4 we consider periodically quenched heterostructures. Thus $h^{(1,2)}$ are given by the (superconducting) QWZ [Equation 4.3] and Haldane [Equation 4.2] model in Section 4.4.1 and Section 4.4.4 respectively, where the superscripts are appended throughout, indicating the parameters for different steps in the quench protocol.

Physically, periodic quenches of period $T_1 + T_2$ are driving fields containing many different frequencies, commensurate with $\Omega = 2\pi/(T_1 + T_2)$. This is evidenced by the Fourier series: $H(t) = \sum_{k\in\mathbb{Z}} \exp(\mathrm{i}k\Omega t) h_k$, where

$$h_k = \begin{cases} \dfrac{h^{(1)}T_1 + h^{(2)}T_2}{T_1 + T_2}, & k = 0, \\ \dfrac{1}{k\pi}\left[h^{(1)}\mathrm{e}^{-\mathrm{i}\frac{\Omega T_1}{2}} \sin\frac{k\Omega T_1}{2} + h^{(2)}\mathrm{e}^{-\mathrm{i}\frac{\Omega(T_1+T_2)}{2}} \sin\frac{k\Omega T_2}{2}\right], & k \neq 0. \end{cases} \tag{4.6}$$

Thus hypothetically one may envisage to implement approximate quenches using lights at frequencies commensurate with each other.

4.3 Method

We apply the method of recursive Floquet-Green's function for the calculations of the DC conductance at each sidebands [238]. These so-called sideband contributions are then summed to fully probe the Floquet edge modes, in accordance with the Floquet sum rule [186]. Here, we briefly sketch the ideas behind the transport calculations in this chapter (please refer to Appendix E for more elaborate descriptions). For undriven samples where superconductivity is present, one can show that if the left (right) lead is set at bias $V_{\mathrm{L/R}} = \pm V/2$, the electrical current flowing in the sample reads [239, 240]:

$$I = \frac{e}{h}\int_{-\infty}^{\infty} \mathrm{d}E\Big[g(E) + g^{\mathrm{LAR}}(E)\Big]\Big[f_{-V}(E) - f_V(E)\Big], \tag{4.7}$$

with the normal and local Andreev reflection coefficients given by:

$$\begin{aligned} g(E) &= \mathrm{Tr}\left[G(E)\Gamma_{\mathrm{R}}(E)G^{\dagger}(E)\Gamma_{\mathrm{L}}(E)\right], \\ g^{\mathrm{LAR}}(E) &= \mathrm{Tr}\left[G(E)\overline{\Gamma}_{\mathrm{L}}(E)G^{\dagger}(E)\Gamma_{\mathrm{L}}(E)\right]. \end{aligned} \tag{4.8}$$

where $G = (E - \mathcal{H} - \Xi_{\mathrm{L}} - \Xi_{\mathrm{R}})^{-1}$ is the retarded Green's function, $\Xi_{\mathrm{L/R}}$ is the left/right self energy due to coupling with metallic leads, $\Gamma = \mathrm{i}P^{\mathrm{e}}(\Xi - \Xi^{\dagger})P^{\mathrm{e}}$ and $\overline{\Gamma} = \mathrm{i}P^{\mathrm{h}}(\Xi - \Xi^{\dagger})P^{\mathrm{h}}$ are the electron- and hole-projected line-width functions, $P^{\mathrm{e/h}} = (1 \pm \tau_z)/2$ is the electron/hole projector, τ_z is the Pauli matrix acting on Nambu space, and $f_V(E) = \{\exp[\beta(E + \mathrm{e}V)] + 1\}^{-1}$ is the Fermi function at inverse temperature β. One can extract from Equation 4.7 a differential conductance by linearizing the Fermi function, assuming a small bias V. For zero-temperature, at energy E_{F}, one obtains the differential longitudinal conductance as:

$$g_{\mathrm{LR}}(E_{\mathrm{F}}) = \frac{e^2}{h}\Big[g(E_{\mathrm{F}}) + g^{\mathrm{LAR}}(E_{\mathrm{F}})\Big]. \tag{4.9}$$

In presence of time-periodic drive, the time-averaged DC conductance for normal transmission becomes [183]:

$$g_{\mathrm{DC}}(E) = \sum_{k\in\mathbb{Z}} \mathrm{Tr}\Big[\boldsymbol{G}_{k0}(\boldsymbol{\Gamma}_{\mathrm{R}})_{00}\boldsymbol{G}^{\dagger}_{0k}(\boldsymbol{\Gamma}_{\mathrm{L}})_{kk}\Big], \tag{4.10}$$

and analogously for the local Andreev reflection, where bold characters are Floquet-Green's functions, satisfying, e.g.:

$$[(E + m\Omega)\boldsymbol{\delta}_{mk} - (\boldsymbol{\mathcal{H}})_{mk} - (\boldsymbol{\Sigma}_{\mathrm{L}} + \boldsymbol{\Sigma}_{\mathrm{R}})_{mk}]\boldsymbol{G}_{kn}(E) = \delta_{mn}, \tag{4.11}$$

and the subscripts mean:

$$\boldsymbol{\mathcal{H}}_{mn} = \frac{\Omega}{2\pi}\int_0^{2\pi/\Omega} \mathrm{d}t \exp[\mathrm{i}(m-n)\Omega t]\mathcal{H}(t) \tag{4.12}$$

(see Appendix E for the definition of Green's functions in the Floquet representation). Finally, to faithfully reflect the topology of Floquet systems via transport calculations, a summation over different Floquet sidebands is performed:

$$\bar{g}(E_{\mathrm{F}}) = \sum_{n\in\mathbb{Z}} g_n(E_{\mathrm{F}}), \tag{4.13}$$

where $g_n(E_{\mathrm{F}}) = g(E_{\mathrm{F}} + n\hbar\Omega)$, applicable to both normal and Andreev processes.

4.4 Results

We first summarize our results to be presented below. We begin in Section 4.4.1, by demonstrating how Floquet engineering can achieve a desirable conductance signal by periodically alternating two static copies which when left alone will fail. Then, in Section 4.4.2, we ask the question: What happens when a normal-superconducting-normal (NSN) graphene junction is irradiated by circularly polarized light? These results set the stage for the bolder question in Section 4.4.3: What is expected of the DC conductance in a Floquet junction where the superconducting part harbors multiple pairs of photoinduced CMEMs? Finally, in Section 4.4.4, we consider how the DC conductance may help to distinguish π Floquet CMEMs and the more conventional 0 Floquet CMEMs. For a more pleasant reading experience, we illustrated these findings in Figures 4.2, 4.4, 4.6, 4.9 for each section.

We now describe the organization of our results. In panels (a) and (b) of Figures 4.3, 4.5, 4.7, 4.8, we show representative Floquet spectra [(a) for the sandwiching FlCI, (b) for the sandwiched FTSC], where chiral edge modes are highlighted in red and green for states localized at top and bottom. In panels (c) and (d) of Figures 4.3, 4.5, 4.7, 4.8, we display the DC conductances evaluated at quasienergy $\epsilon_{\mathrm{F}} = 0$, or $\epsilon_{\mathrm{F}} = \hbar\Omega/2$ in Section 4.4.4 (y axis), when two different types of parameters are swept (along the x axis). For the case of continuous driving fields (Sections 4.4.2, 4.4.3), we vary laser parameters, namely, amplitude, polarization angle, or frequency, of either the FlCI or FTSC. For the case of periodic quench (Sections 4.4.1, 4.4.4), we vary the two quench durations. The goal is to observe half-integer conductance plateaus over different drive-related parameters, which demonstrate the existence of photoinduced CMEMs over a diverse choice of wide parameter windows.

Dealing with scattering in superconducting systems, there are several transport coefficients to consider. For our purpose, we display the normal transmission (g) and the local Andreev reflection (g^{LAR}), because the longitudinal conductance is a sum of only these two. In static QAHI-TSC-QAHI junctions, theoretical and experimental studies [94, 96] showed that half-quantized longitudinal conductance may signal the existence of CMEM in the TSC (see Section 4.5.2 for an explanation of this transport signature, which is based on Refs. [94, 96]). Extrapolating from static results, one might expect the period-averaged conductance to also be quantized in the Floquet case.

It turns out that although the DC conductance enjoys stability against disorder and achieves plateaus within topologically nontrivial regimes, it is not quantized at integer [185] (or half-integer as in this work). To understand this, suppose we wish to probe a Floquet edge mode $|\psi_\epsilon(t)\rangle$ at quasienergy $\epsilon = E_{\mathrm{F}} \in [-\hbar\Omega/2, \hbar\Omega/2]$ by transport measurement. To this end, not only can we inject states at energy E_{F}, all modes

$|\phi_n(t)\rangle$ at energies $E_n = E_\mathrm{F} + n\hbar\Omega$ (with $n \in \mathbb{Z}$) are also viable candidates, thanks to the periodic drive at frequency Ω applied to the central hybrid structure. Since the incoming states $|\phi_n(t)\rangle$ are physically distinct, they cannot all have unity overlap with the Floquet mode $|\psi_\epsilon(t)\rangle$. Hence the transport measurement at E_F only probes the part of the edge modes that are not scattered to other energies, and to fully reconstruct the edge state by DC conductance, one has to sum over all sideband contributions E_n.

Therefore, in our results for DC conductance, we display the dominant sideband contributions g_n, g_n^{LAR}, typically for $n \in \{-2, \cdots, 2\}$. The purpose is to demonstrate that despite bearing little resemblance to any topological quantization, the crucial equality of local Andreev reflection and normal transmission still holds *at each sideband*. Thus, the DC conductance at any Floquet gaps actually contains topological information of the heterostructure harboring a certain number of Floquet CMEMs and chiral fermions.

4.4.1 Half-quantized plateau by quenching two devices with mismatched Chern numbers

We begin with the s-wave superconducting Qi-Wu-Zhang (QWZ) model, which was first studied in Ref. [95]. For a single CMEM to manifest as half-quantized conductance, an important topological prerequisite is that one must have Chern numbers $\mathcal{C} = 1$ and $\mathcal{N} = 1$ for the two layers of Chern insulators and the topological superconductor in the middle respectively. This is because for $\mathcal{N} = 2$, the incoming chiral ordinary fermion travels unimpeded, whereas if $\mathcal{N} = 0$, then it gets completely reflected [96].

Suppose now we periodically quench two devices with mismatched Chern numbers: $\mathcal{C} = 1, \mathcal{N} = 2$, and $\mathcal{C} = -1, \mathcal{N} = -2$. With two additional parameters, i.e. the quench durations $T_{1,2}$, the resultant device can explore a much larger topological phase diagram.

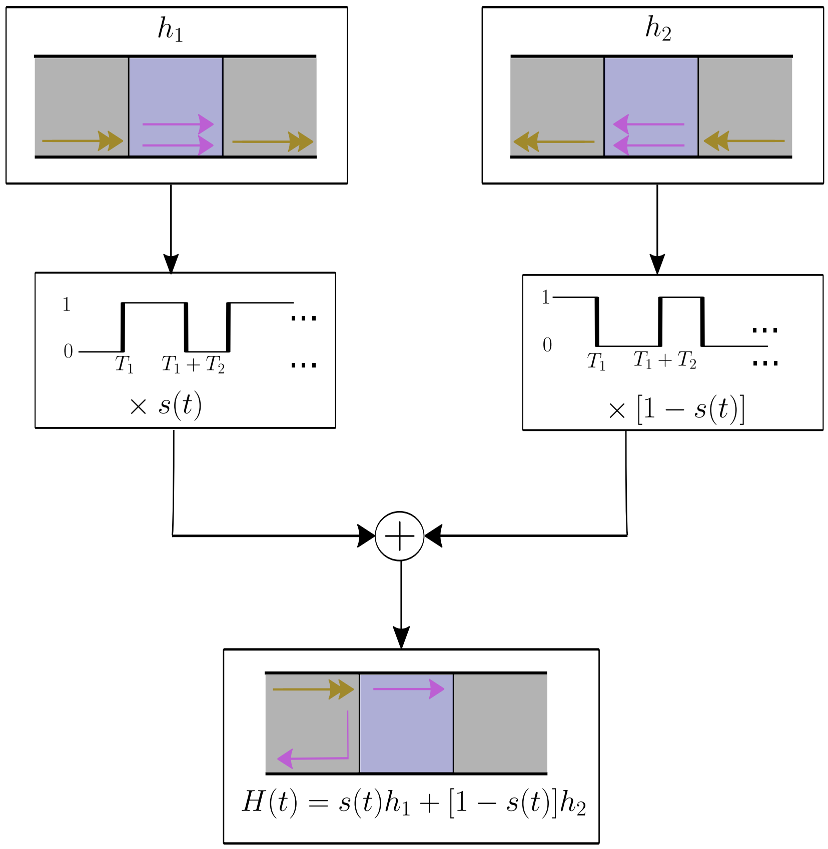

Figure 4.2: Given two copies of Chern insulator-superconductor-Chern insulator heterostructure ($h_{1,2}$), each of which does not yield equal Andreev-normal scattering, one can perform Floquet engineering and obtain a system where the CMEM in the FTSC may manifest as half-integer quantized longitudinal conductance [$H(t)$]. In the top panel, the two static heterostructures have weak superconducting pairing, so that the incoming chiral fermions travel unimpeded in the superconductor. By subjecting these two devices to square waves [$s(t)$ and $1 - s(t)$ in the middle panel], one can arrive at a time-periodic system which harbors a single Floquet CMEM in the superconductor (bottom panel), yielding half-quantized conductance.

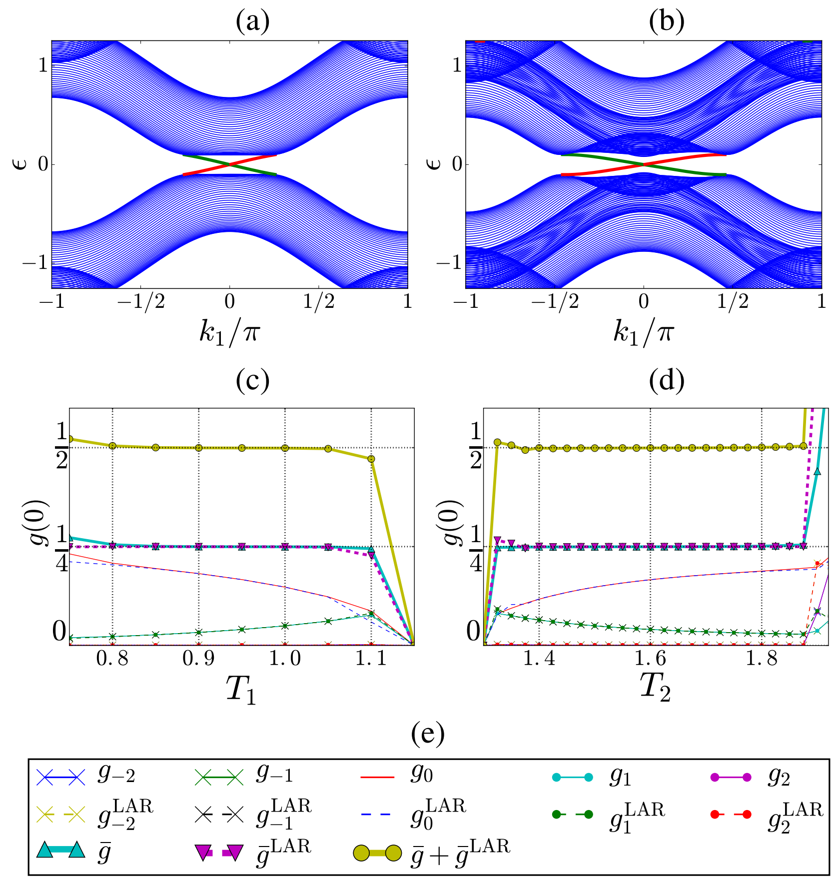

Figure 4.3: Periodic quench turns two static Chern insulator-superconductor-Chern insulator junctions with mismatched Chern numbers into a FlCI-FTSC-FlCI junction yielding half-quantized DC conductance. Top panel: Representative spectra in the Floquet hybrid device with fixed quench durations $T_1 = 1, T_2 = 1.5$, where the parameters during the quench duration T_1 are $m^{(1)} = -2.1, A^{(1)} = B^{(1)} = 1, \Delta^{(1)} = 1.6$, and the parameters during the quench duration T_2 are $m^{(2)} = 1.6, A^{(2)} = B^{(2)} = -1, \Delta^{(2)} = -1.4$, applicable to both (a) FlCIs and (b) FTSC except the pairing Δ which is present only at the FTSC. Middle panel: DC conductance of Floquet sidebands $E_n = 0 + \hbar\Omega$ due to normal transmission (g_n) and local Andreev reflection (g_n^{LAR}). When the sideband contributions are summed, half-quantized conductance plateaus are observed over different drive parameters. (c), the plateau is observed over the first quench duration T_1, when $T_2 = 1.5$ is fixed. (d): T_2 is varied for the manifestation of a plateau, when $T_1 = 1$ is held constant. Bottom panel (e): Legends of plots for (c) and (d).

In particular, with a judicious choice of $T_{1,2}$, the Floquet junction realizes a single chiral fermion at the FlCIs [Figure 4.3(a)] and a single CMEM at the FTSC [Figure 4.3(b)]. This idea is schematically illustrated in Figure 4.2. Physically, if we denote the square wave for the first quench duration as

$$s(t) = \begin{cases} 1 & 0 < t \bmod \mathcal{T} < T_1, \\ 0 & T_1 < t \bmod \mathcal{T} < T_1 + T_2, \end{cases} \tag{4.14}$$

then the Hamiltonians read:

$$\begin{aligned} H_{\mathrm{FlCI}}(\boldsymbol{k}, t) &= s(t) h^{(1)}(\boldsymbol{k}) + [1 - s(t)] h^{(2)}(\boldsymbol{k}), \\ H_{\mathrm{FTSC}}(\boldsymbol{k}, t) &= s(t) \Big[h^{(1)}(\boldsymbol{k}) + \Delta^{(1)} \sigma_y \tau_y \Big] \\ &\quad + [1 - s(t)][h^{(2)}(\boldsymbol{k}) + \Delta^{(2)} \sigma_y \tau_y], \end{aligned} \tag{4.15}$$

where $\mathcal{T} = T_1 + T_2$ is the period, σ acts on the orbital space and τ acts on Nambu space, $h^{(i)}(\boldsymbol{k})$ is given by:

$$h^{(i)}(\boldsymbol{k}) = \begin{bmatrix} h^{(i)}_{\mathrm{QWZ}}(\boldsymbol{k}) & 0 \\ 0 & -(h^{(i)})^*_{\mathrm{QWZ}}(-\boldsymbol{k}) \end{bmatrix} \tag{4.16}$$

and $h^{(i)}_{\mathrm{QWZ}}(\boldsymbol{k})$ is given by Equation 4.3, with the superscript appended to indicate the different parameters for different quench cycles ($i = 1, 2$). Hence, we perform DC conductance calculations at $E_{\mathrm{F}} = 0$ by tuning the quench durations T_1 [Figure 4.3(c)] and T_2 [Figure 4.3(d)]. We observe that the individual sidebands for both normal transmission and local Andreev reflection (g_n, g_n^{LAR}) vary, but their sums ($\bar{g}, \bar{g}^{\mathrm{LAR}}$) form plateaus of 1/4, resulting in DC longitudinal plateaus of 1/2.

4.4.2 Photoinduced CMEM in graphene hybrid structure

In the previous example, the two pre-quench junctions can actually realize a single pair of CMEM [95] with other choices of parameters. A natural question to ask is

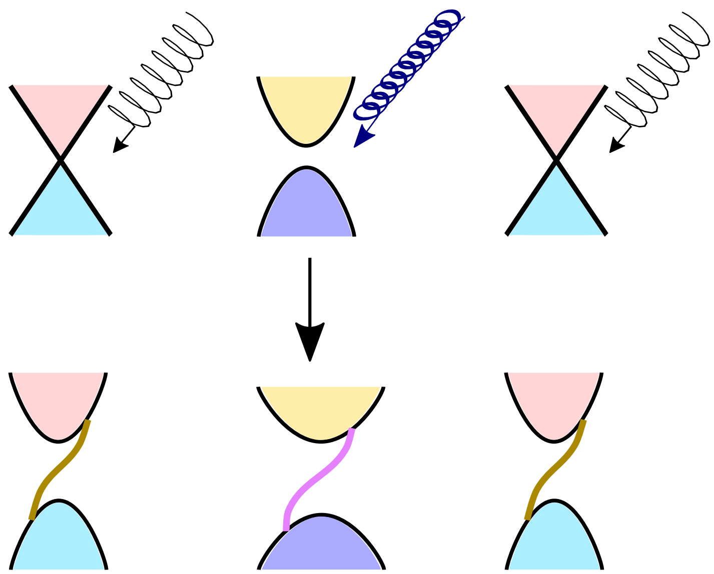

Figure 4.4: Schematic of elliptically polarized light turning a graphene normal-superconductor-normal junction into a Floquet Chern insulator-topological superconductor-Chern insulator heterostructure. Starting from Dirac cones in normal graphene (top panel, left and right) and topologically trivial superconductor (top panel, middle), light irradiation breaks time-reversal symmetry, result in chiral edge modes in both the normal and superconductor part (bottom panel).

thus: In a device where the existence of CMEM is forbidden by symmetry, can periodic driving fields lift this restriction? Inspired by Ref. [113], here we answer this question affirmatively by considering the dynamical generation of a single Floquet CMEM from a graphene NSN junction, as depicted by Figure 4.4.

More specifically, the Hamiltonians of the FlCI and FTSC are given by:

$$\begin{aligned} H_{\mathrm{FlCI}}(\boldsymbol{k},t) &= \begin{bmatrix} h_{\mathrm{H}}[\boldsymbol{k}-\boldsymbol{\mathcal{A}}_{\mathrm{FlCI}}(t)] & 0 \\ 0 & -h_{\mathrm{H}}^{*}[-\boldsymbol{k}-\boldsymbol{\mathcal{A}}_{\mathrm{FlCI}}(t)] \end{bmatrix}, \\ H_{\mathrm{FTSC}}(\boldsymbol{k},t) &= \begin{bmatrix} h_{\mathrm{H}}[\boldsymbol{k}-\boldsymbol{\mathcal{A}}_{\mathrm{FTSC}}(t)] & -\mathrm{i}\Delta\sigma_y \\ \mathrm{i}\Delta\sigma_y & -h_{\mathrm{H}}^{*}[-\boldsymbol{k}-\boldsymbol{\mathcal{A}}_{\mathrm{FTSC}}(t)] \end{bmatrix}, \end{aligned} \tag{4.17}$$

where the periodic driving fields are inhomogeneous on the FlCI and FTSC. In above, the graphene Hamiltonian h_{H} can be written as in Equation 4.2, but keeping only nearest neighbor ($t_2 = 0, \Phi = 0$). As for the driving field, on the Floquet Chern insulators one has $\boldsymbol{\mathcal{A}}_{\mathrm{FlCI}}(t) = A_{\mathrm{FlCI}}\Big[\sin(\Omega t)\boldsymbol{a}_1 + \sin(\Omega t + \phi_{\mathrm{FlCI}})\boldsymbol{a}_2\Big]$, where $\boldsymbol{a}_1 = \sqrt{3}\hat{\boldsymbol{x}}, \boldsymbol{a}_2 = (\sqrt{3}\hat{\boldsymbol{x}} + 3\hat{\boldsymbol{y}})/2$ are the primitive vectors of honeycomb lattice with zigzag edge, and we have a similar expression for the driving field on the photoinduced topological superconductor. The static device now consists of a graphene ribbon, where the center is proximitized by s-wave superconductor. Once periodic driving fields with appropriate parameters are added, we observe a $\mathcal{C} = 1$ FlCI [Figure 4.5(a)] and $\mathcal{N} = 1$ FTSC [Figure 4.5(b)] in some representative spectra.

Knowing that our Floquet device may yield a single FlCI fermion and a single CMEM at one edge of the system, we proceed to probe the DC transport.

In Figure 4.5(c), the DC conductance is calculated as a function of the polarization angle at the FlCIs. We observe that within $[0, \pi]$, almost all angles, except those at the boundary values $0, \pi$, yield half-quantized DC conductance. This is because for $\phi_{\mathrm{FlCI}} = 0, \pi$, the light is linearly polarized and does not break time-reversal symmetry. Next, we vary frequency and find that beyond a critical value [near $\Omega = 3$ in Figure 4.5(d)], one always obtains $1/4$ normal transmission and local Andreev reflection. In fact, extrapolating to the high-frequency regime and performing a Magnus expansion [113], it is expected that one can always gap the normal-superconducting graphene to generate a chiral regular fermion and a CMEM, except that the ± 1 Floquet sideband contributions tend to zero asymptotically as Ω increases.

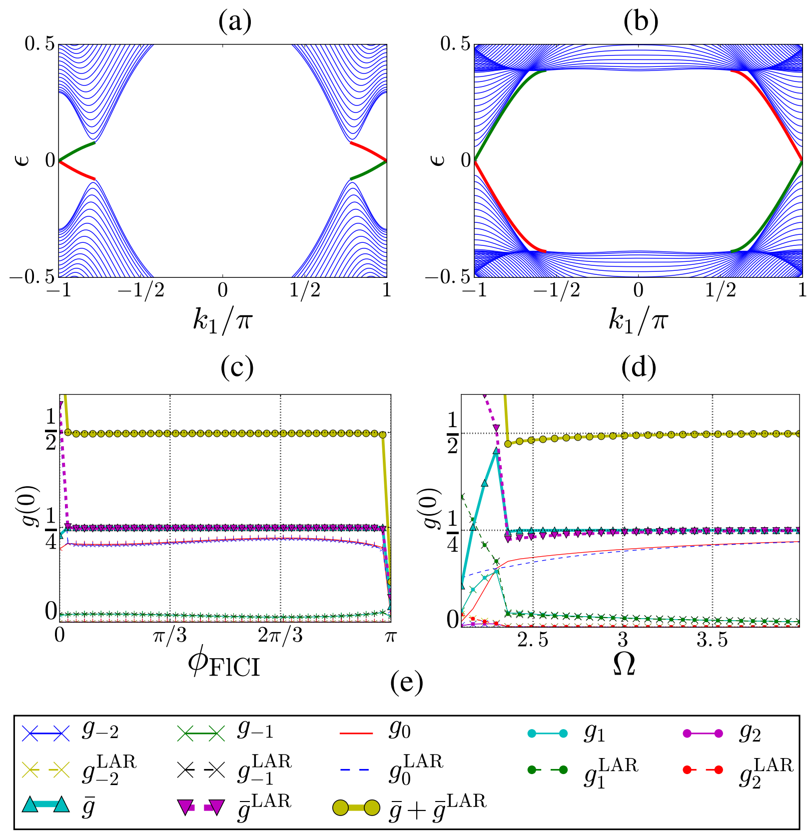

Figure 4.5: Photoinduced chiral Majorana edge mode in a graphene normal-superconductor-normal junction irradiated by elliptically polarized light. Top panel: Representative spectra in the junction, with (a) FlCI: $t_1 = 1, A_{\text{FlCI}} = 1.25, \Omega = 3.4, \phi_{\text{FlCI}} = 0.9\pi$, (b) FTSC: $t_1 = 1, \Delta = 0.5, A_{\text{FTSC}} = 1.9, \Omega = 3.4, \phi_{\text{FTSC}} = \pi/2$. Middle panel: DC conductance at different Floquet sidebands $E_n = 0 + n\hbar\Omega$, which when summed ($\bar{g} + \bar{g}^{\text{LAR}}$) yields half-quantized plateaus. Parameters are the same as in (a),(b) except the polarization angle at the FlCI and the drive frequency. (c): The polarization angle at the FlCIs, ϕ_{FlCI}, is varied when $\Omega = 3.4$ is held constant. (d): The drive frequency Ω is varied when $\phi_{\text{FlCI}} = 0.9\pi$ is fixed. Bottom panel (e): Legends of plots (c) and (d).

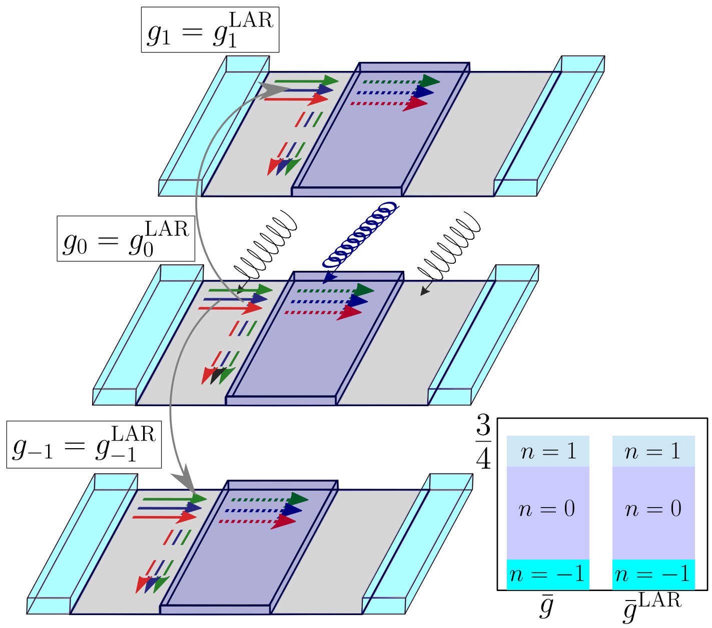

Figure 4.6: Schematic illustration of transport signature of a Floquet Chern insulator-topological superconductor-Chern insulator junction, in presence of three chiral edge modes in both the FlCIs and FTSC. The topological properties of the system are described by the three CMEMs in the FTSC and three chiral fermions in the FlCIs. If these topological edge modes do not interfere with each other, the Anantram-Datta-Landauer-Büttiker formula predicts a longitudinal conductance of $3/2$ for a static sample. In Floquet systems, edge states are distributed by photons to different sidebands ($n = -1, 0, 1$) and the DC conductance deviates from $3/2$. Remarkably, at each sideband there is equality among Andreev and normal scattering processes ($g_n = g_n^{\mathrm{LAR}}$ for example). One can recover half-integer quantized conductance by summing over the Floquet sidebands (the Floquet sum rule), as depicted by the schematic bar chart (inset), where $\bar{g}^{(\mathrm{LAR})} = \sum_n g_n^{(\mathrm{LAR})}$ and the two-terminal conductance is $g_{12} = g + g^{\mathrm{LAR}}$.

4.4.3 Higher half-quantized plateaus from a driven Haldane model

As alluded to, Floquet systems boast a wide range of phases with large topological invariants [166]. This feature is all the more appealing for the transport signature of CMEMs: While alternative mechanisms may explain half-quantized plateaus [98, 99], it is unlikely that these mechanisms, of static origin, are able to induce *higher* half-quantized plateaus from models with minimal number of bands. In addition, for the purpose of TQC, a larger number of MZMs allows more qubits to be encoded.

Therefore, we investigate the transport signature of devices harboring more than one CMEMs. The key findings and ideas are summarized in Figure 4.6. To look for light-induced large-topological-invariant phases, we choose the Haldane model with s-wave pairing potential, described by Equation 4.1 and Equation 4.2. Experimentally, by means of ultracold fermionic gases, the former was realized using ^{40}K atoms modulated in time [237], the latter via ^{6}Li hyperfine state pairs close to Feshbach resonance [241]. The left and right parts are given by the Haldane model without s-wave pairing, and the entire device is irradiated by elliptically polarized light. More precisely, the Hamiltonians are:

$$\begin{aligned} H_{\mathrm{FICI}}(\boldsymbol{k},t) &= \begin{bmatrix} h_{\mathrm{FICI}}(\boldsymbol{k},t) & 0 \\ 0 & -h^{*}_{\mathrm{FICI}}(-\boldsymbol{k},t) \end{bmatrix}, \\ H_{\mathrm{FTSC}}(\boldsymbol{k},t) &= \begin{bmatrix} h_{\mathrm{FTSC}}(\boldsymbol{k},t) & -\mathrm{i}\Delta\sigma_y \\ \mathrm{i}\Delta\sigma_y & -h^{*}_{\mathrm{FTSC}}(-\boldsymbol{k},t) \end{bmatrix}, \end{aligned} \tag{4.18}$$

where the diagonal term is given by the Haldane model. For example, on the Floquet Chern insulators one has:

$$h_{\mathrm{FICI}}(\boldsymbol{k},t) = \boldsymbol{f}_{\mathrm{FICI}}[\boldsymbol{k} - \boldsymbol{\mathcal{A}}_{\mathrm{FICI}}(t)] \cdot \boldsymbol{\sigma}, \tag{4.19}$$

where the Haldane model $\boldsymbol{f}$ is described in Equation 4.2 and elliptically polarized light given by Equation 4.4. Similar expressions hold for the FTSC, with the labels replaced accordingly.

We now discuss the anticipated transport behavior when several CMEMs are present. For the case of a single CMEM, the splitting of a chiral ordinary fermion into two CMEMs (see Section 4.5.2) is a major reason behind its half-quantized conductance. Now suppose the device hosts $2n+1$ chiral ordinary edge modes and $2n+1$ CMEMs, with $n > 0$. Guided by Occam's razor, an immediate intuition is that each of the $2n+1$ incoming chiral modes will undergo its own splitting, giving rise to 1/4 local Andreev reflection and normal transmission each, so that the conductance will be given by $(2n+1)/2$.

To verify our insight above, considering that the next entry in the hierarchy of half-quantized conductance is 3/2, we seek phases with three edge modes in both the FlCIs and the FTSC. An example is given in Figures 4.7(a-b), where the three chiral edge modes of interest occur at the central Floquet gaps. Note that the driving parameter A and Ω considered here are rather realistic, insofar as they are indeed within the range achieved in the cold-atom experiment reported in Ref. [237]. Then, we compute the DC conductance at $E_{\mathrm{F}} = 0$ by varying the vector potential at the FlCIs [Figure 4.7(c)] and the polarization angle at the FTSC [Figure 4.7(d)]. In Figure 4.7(c), the $n = \pm 1$ sidebands already constitute plateaus, with the $n = 0, \pm 2$ sidebands drifting not too far away from their respective values. In Figure 4.7(d), all sidebands form non-quantized plateaus themselves. While the exact conductance values may not bear any discernible feature, the sidebands again always have equal normal transmission and local Andreev reflection. Furthermore, when they are summed over, we obtain 3/4 plateaus $(\bar{g}, \bar{g}^{\mathrm{LAR}})$, which in turns yield 3/2 for the total longitudinal DC conductance. This

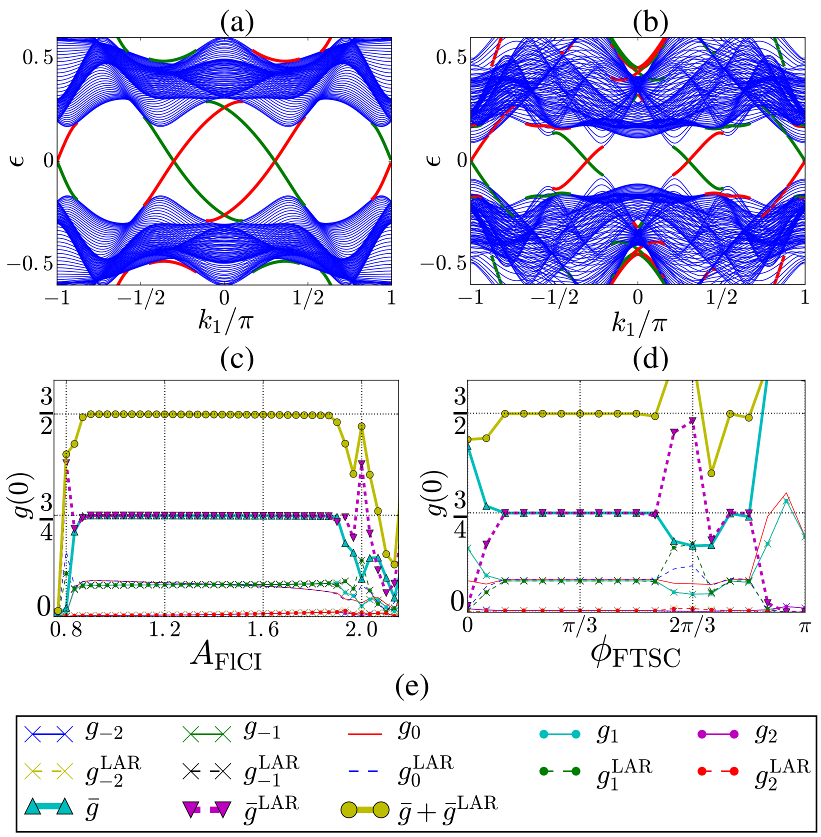

Figure 4.7: Existence of three chiral fermions in the FlCI and three CMEMs in the FTSC leads to higher half-quantized DC conductance plateau at 3/2 after the Floquet sum rule. Top panel: Representative spectra in the junction, with (a): FlCI: $t_1^{\mathrm{FlCI}} = 0.8, t_2^{\mathrm{FlCI}} = 0.3, \Phi^{\mathrm{FlCI}} = \pi/2, A_{\mathrm{FlCI}} = 1.25, \phi_{\mathrm{FlCI}} = \pi/2, \Omega = 1.5$, (b): FTSC: $t_1^{\mathrm{FTSC}} = 1, t_2^{\mathrm{FTSC}} = 0.45, \Phi^{\mathrm{FTSC}} = \pi/2, \Delta = 0.6, A_{\mathrm{FTSC}} = 1.75, \phi_{\mathrm{FTSC}} = \pi/3, \Omega = 1.5$. Middle panel: DC conductance of Floquet sidebands $E_n = 0 + n\hbar\Omega$ (where $\Omega = 1.5$) for both the normal transmission (g_n) and local Andreev reflection (g_n^{LAR}), which sum to give higher half-quantized plateaus ($\bar{g} + \bar{g}^{\mathrm{LAR}}$). The parameters are the same as in (a),(b), except the vector potential at the FlCI and polarization angle at the FTSC. (c): The vector potential at the FlCIs is varied for the manifestation of plateau, where $\phi_{\mathrm{FTSC}} = \pi/3$ is fixed. (d): The polarization angle at the FTSC, ϕ_{FTSC}, is tuned with $A_{\mathrm{FlCI}} = 1.25$ held constant. Bottom panel (e): legends of plots for (c) and (d).

result strongly supports our earlier intuition that for multiple incoming chiral fermions, if the FTSC permits formation of CMEMs with the same number and chiralities, then equal scattering processes for each incoming mode is favored, and higher half-quantized plateaus ensue.

4.4.4 π Floquet CMEMs and their transport

With a glimpse of the transport properties of multiple CMEMs, we are now ready to address the case of CMEMs that can only exist in Floquet topological phases, namely, those crossing $\epsilon = \pm\hbar\Omega/2$ in Floquet spectra. Because quasienergies $\pm\hbar\Omega/2$ correspond to eigenphases $\pm\pi$ of the Floquet operator, they are also known as Floquet π modes. Many peculiar features of Floquet systems owe their existences to these π modes, such as non-adiabatic quantized pump [206]. In the quest for Majorana fermions, the fact that quasienergies $\pm\hbar\Omega/2$ are identical implies a larger search space for their realizations [169].

To look for Floquet π modes, we consider a periodically quenched Haldane model with third-neighbor hoppings. Then, we periodically quench the parameters Φ, t_3. The Hamiltonians can be described similarly as in Eqs.Equation 4.14,Equation 4.15, but with the bare (i.e. non-superconducting) system replaced by $h_{\mathrm{H}}(\boldsymbol{k}) + V(\boldsymbol{k})$, where:

$$\begin{aligned} V(\boldsymbol{k}) = t_3\{2\cos[\boldsymbol{k}\cdot(\boldsymbol{a}_1 - \boldsymbol{a}_2)] + \cos[\boldsymbol{k}\cdot(\boldsymbol{a}_1 + \boldsymbol{a}_2)]\}\sigma_x \\ + t_3 \sin[\boldsymbol{k}\cdot(\boldsymbol{a}_1 + \boldsymbol{a}_2)]\sigma_y. \end{aligned} \tag{4.20}$$

Two representative Floquet spectra are illustrated in Figures 4.8(a-b), where the gaps at $\epsilon = \pm\hbar\Omega/2$ harbor three pairs of π modes for both the FlCIs and the FTSC.

Thus, we study the DC conductance at $E_{\mathrm{F}} = \hbar\Omega/2$, as functions of quench durations $T_{1,2}$. The explanation for $\frac{3}{2}\frac{e^2}{h}$ DC conductance in Section 4.4.3 carries over, because

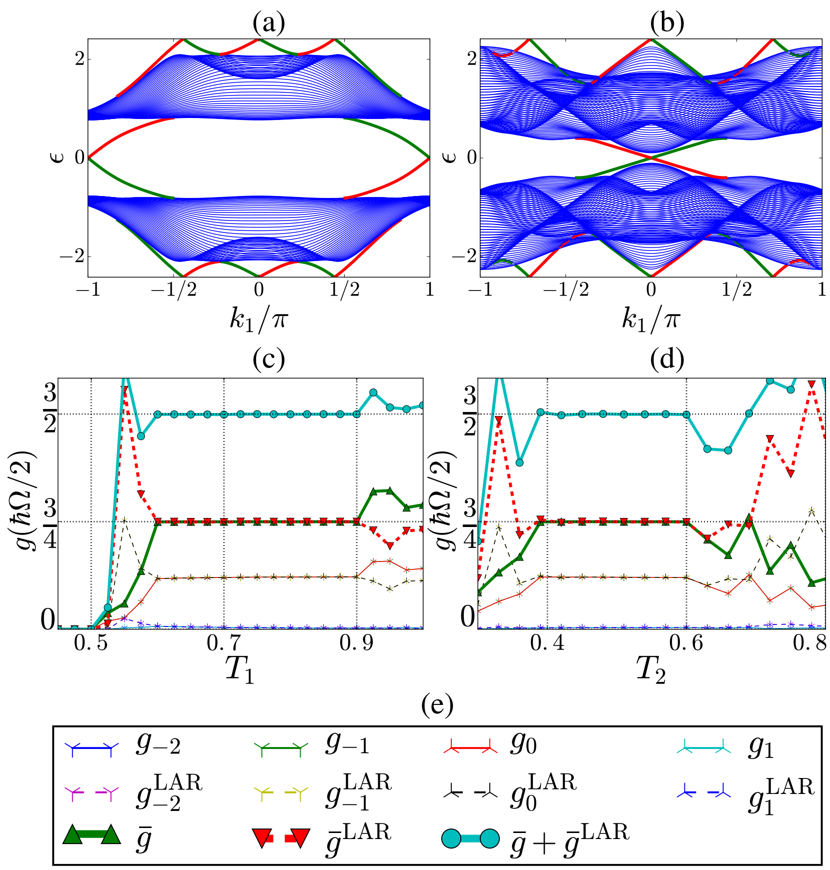

Figure 4.8: Transport signature of three winding chiral Majorana edge modes in a periodically quenched FlCI-FTSC-FlCI heterostructure, where three photoinduced chiral fermions are present in the FlCIs. Top panel: Representative spectra in the junction with fixed quench durations $T_1 = 0.7, T_2 = 0.6$, where the parameters during the first quench duration T_1 are $t_1^{(1)} = 1, t_2^{(1)} = 0.8, t_3^{(1)} = 1, \Delta^{(1)} = 1.5, \Phi^{(1)} = \pi/6$, and the parameters during the second quench duration T_2 are $t_1^{(2)} = 1, t_2^{(2)} = 0.8, t_3^{(2)} = -1, \Delta^{(2)} = 1.5, \Phi^{(2)} = -\pi/2$, applicable to both (a) FlCIs and (b) FTSC, except the pairing Δ which is present only at the FTSC. Middle panel: DC conductance of different Floquet sidebands $E_n = \hbar\Omega/2 + n\hbar\Omega/2$ [where Ω varies from points to points, since we calculate the conductance as we vary the quench durations which change Ω via $\Omega = 2\pi/(T_1 + T_2)$], for both the normal transmission (g_n) and local Andreev reflection (g_n^{LAR}), where 3/2 conductance plateaus are observed. The parameters are the same as in (a),(b) except the quench durations $T_{1,2}$. (c): The plateau manifests as the quench duration T_1 is tuned, keeping $T_2 = 0.6$ fixed. (d) A plateau is observed as T_2 varies, with $T_1 = 0.7$ held constant. Bottom panel (e): Legends of plots.

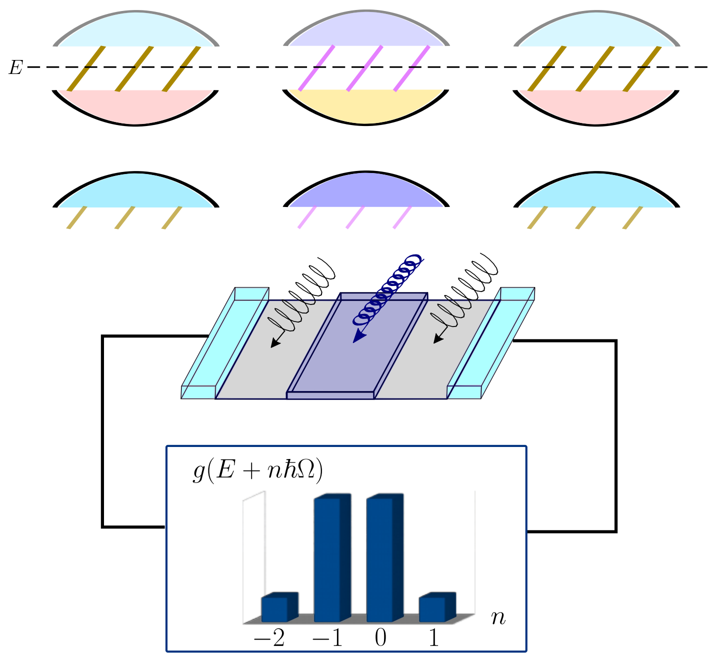

Figure 4.9: The sideband profile of Floquet π CMEMs in a FlCI-FTSC-FlCI heterostructure. The top panel depicts the Floquet spectra of the Floquet Chern insulators (left and right) and the Floquet topological superconductor (middle), where conductance is probed at energy E near the upper Floquet gap, where π Floquet chiral fermions and CMEMs are present. When one probes the DC conductance, in contrast to edge modes occuring near the central Floquet gap, for π modes, the sideband contributions towards the conductance are evenly distributed, i.e. dominated by a double peaks ($n = -1, 0$) in the bottom bar chart, instead of a single peak.

both the number and chirality of the incoming FlCI chiral fermions and CMEMs are the same, and $\epsilon = \hbar\Omega/2$ is degenerate with $\epsilon = -\hbar\Omega/2$.

Notice however that for Floquet CMEMs at $\epsilon = 0$, the sideband contributions are symmetrically distributed around a single $n = 0$ sideband, so that there is an odd number of dominant sidebands [$n = \pm 1$ around $n = 0$ in Figures 4.5-4.7(c-d)]. On the contrary, for the $\epsilon = \hbar\Omega/2$ CMEM, the non-negligible sidebands are distributed around a *twin* central sidebands [$n = -1, 0$ in Figure 4.8(c-d)], i.e. there is an even number of dominant sidebands, as illustrated in Figure 4.9. This observation is consistent with

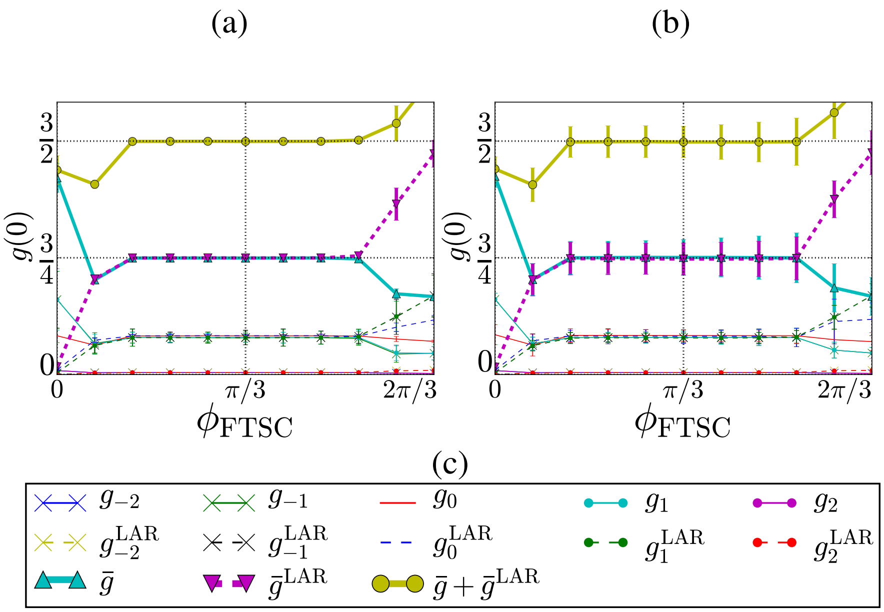

Figure 4.10: Robustness of the DC conductance against random onsite potential of a continuously driven FlCI-FTSC-FlCI junction harboring three edge modes in the central Floquet gap [Section 4.4.3], evaluated at $\epsilon_{\mathrm{F}} = 0$. The parameters used for the heterostructure are the same as in the representative spectra [panels (a),(b) in Figure 4.7]. (a): Result for static disorder. (b): Result for time-periodic disorder at frequency Ω. The disorder is uniform in sublattice space and has a box-like distribution in $[-W, W]$, where $W \approx 0.4\delta$, with δ the size of the central Floquet gap in Figure 4.7(b). The error bars are magnified by three times, and represent the standard deviation of 45 disorder realizations.

previously-reported results in Floquet quantum Hall insulators [238], and may serve as a telltale sign of distinguishing π and zero CMEMs in Floquet systems.

4.4.5 Disorder

In the first TI-based experimental realization of CMEM [94], half-quantized plateaus were observed during sweeps of magnetic field. While this induces topological phase transitions for a single CMEM to emerge, it also generates many magnetic domains [242], resulting in a highly-disordered sample. Hence, based on the theory of percolation transition, several authors have proposed alternative mechanisms [98, 99] that can give rise to half-quantized conductance in QAHI-TSC-QAHI heterostructures without CMEMs.

Considering the prominent roles that disorder may play, here we ask whether the higher half-quantized plateaus due to multiple Floquet CMEMs can survive disorder. To that end, we model disorders as random onsite potentials, uniform in spin or sublattice space, and distributed uniformly in $[-W, W]$. We consider disordered samples from Sections 4.4.3, 4.4.4, and compute the DC conductance for different Floquet sidebands at $\epsilon_{\mathrm{F}} = 0$. In Floquet systems, one may incorporate the effect of time-dependent disorder, provided the time dependence is periodic at the same fundamental frequency of the driving field. Explicitly, such a term is described by

$$H_{\mathrm{dis}}(t) = \sum_{i,s} \xi_i \cos(\Omega t) \hat{c}^{\dagger}_{i,s} \hat{c}_{i,s}, \tag{4.21}$$

where i ranges over the lattice site in both the FlCIs and FTSC, s refers to the spin or orbital degree of freedom, and ξ_i is a random number drawn uniformly from $[-W, W]$.

As shown in Figure 4.10, at $\epsilon_{\mathrm{F}} = 0$ we observe the topological protection of the three Floquet CMEMs against disorder of magnitude up to ≈ 0.4 times the superconducting gap in Figure 4.7(b). Interestingly, for static disorder, the 3/4 plateaus for both normal transmission and local Andreev reflection are robust at each realization. On the other hand, the system appears to be less resistant against time-periodic disorder, since it is only after averaging that the 3/4 plateaus remain stable.

Next, we probe the robustness of the π Floquet CMEMs Section 4.4.4 in Figure 4.11. For the sake of comparison, we similarly choose a disorder strength ≈ 0.4 the size of the $\pm\pi$ Floquet gap in spectrum 4.8(b). Remarkably, the robustness against disorder is swapped as compared with the zero modes considered previously. More precisely, the

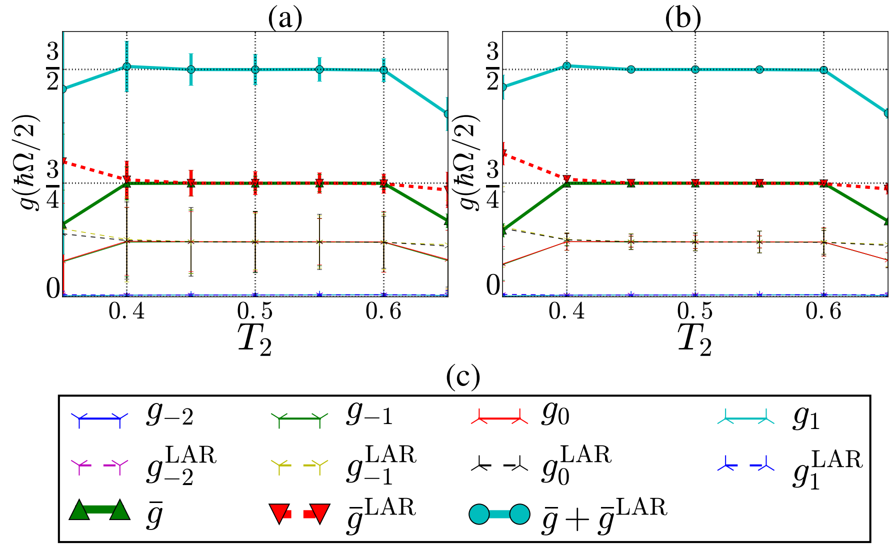

Figure 4.11: Robustness against random onsite disorder of the DC conductance due to the three winding chiral modes in a FlCI-FTSC-FlCI device [Section 4.4.4], evaluated at $\epsilon_{\mathrm{F}} = \hbar\Omega/2$. The parameters used are the same as given by the representative spectra [panels (a),(b) in Figure 4.8], except for Ω which varies from point to point since we compute the DC conductance as a function of the second quench duration T_2. (a): Result for static disorder. (b): Result for time-periodic disorder at frequency Ω. The disorder is uniform in sublattice space and has a box-like distribution in $[-W, W]$, where $W \approx 0.4\delta$, with δ the size of the ± 1 Floquet gap in Figure 4.8(b). The error bars are magnified by 10 times, and represent the standard deviation of 45 disorder realizations.

π Floquet modes are more robust to time-periodic disorder, less so to static disorder, whereas for the zero CMEMs it is the reverse. In total, the π CMEMs from Section 4.4.4 are more resistant against disorder compared with their zero analogs from Section 4.4.3, since the errorbars are magnified by 10 and 3 times respectively [Figures 4.11, 4.10].

4.5 Discussions

4.5.1 On chiral Majorana edge modes

Several authors [99, 227] have cautioned against the misuse of terminologies such as "Majorana zero modes" and "Majorana fermions". Thus we deem it necessary to explain in what context we are referring to the edge states in our systems as CMEMs.

By definition, superconductors always preserve the particle-hole symmetry, so that in two dimension with mixed boundary condition, eigenstates Ψ_k at energy E_k always have charge-conjugation partners $C\Psi^*_{-k}$ at energy E_{-k} [233], where C is the unitary part of the particle-hole symmetry. Thus, if the superconductor is gapped and yields zero or π quasienergy solutions Ψ_k, one may construct an eigenstate $\tilde{\Psi}_k = \Psi_k + C\Psi^*_{-k}$ which obeys the Majorana-like condition $C\tilde{\Psi}_{-k} = \tilde{\Psi}_k$. It is in this regard that we refer to the gapless modes in the FTSC spectra [Figures 4.5-4.8(b)] as CMEMs.

4.5.2 Origin of half-quantized conductance

The half-quantized conductance in a QAHI-TSC-QAHI heterostructure observed in Ref. [94] relies on the following facts: (i) domain wall forms as CMEM between a $\mathcal{C} = 1$ QAHI and a $\mathcal{N} = 1$ TSC, and (ii) a CMEM is an equal-weight superposition of electron and hole. Therefore, an incoming chiral regular fermion from the QAHI can be scattered into two CMEMs: γ_a on the interface between the QAHI and the TSC, or γ_b on the interface between the TSC and vacuum. Now, γ_a corresponds to normal reflection and local Andreev reflection, whereas γ_b corresponds to normal transmission and crossed Andreev reflection. These processes must occur with equal probabilities $(= 1/4)$, because $\gamma_{a,b}$ being Majorana fermions, are linear combinations of electron and hole with equal weights.

Next, working within the Anantram-Datta generalization [243] of the Landauer-Büttiker formalism, we model the sample as a three-terminal device, the three terminals being left, right, and superconductor, at voltages $V_{\rm L}, V_{\rm R}, V_{\rm sc}$ respectively. If the following conditions are met: (i) the superconductor is grounded, $V_{\rm sc} = 0$, (ii) the left and right leads are biased symmetrically, $V_{\rm L} = -V_{\rm R}$, and (iii) all normal and Andreev processes have equal probabilities, then one can show that [96], no current flows in or out the superconductor, and the only current flowing in the device is between the leads, with $I_{\rm L} = -I_{\rm R} = e^2 V_{\rm L}/h$. In this case, the longitudinal conductance $g_{\rm LR} = I_{\rm L}/(V_{\rm L} - V_{\rm R})$ yields the half-integer $\frac{1}{2}\frac{e^2}{h}$.

This justifies using the two-lead setting as discussed in Section 4.3 to study the transport of such a device: Equation 4.7 is left-right symmetric, namely, the current leaving the left lead equals the current entering the right lead. Thus even if there is superconductivity in the sample, it draws no current, so that we are exactly in the configuration as described in the previous paragraph, and the conductance in Equation 4.9 is equivalent to the one used in Ref. [96].

Importantly, Equation 4.7 has the advantage that the normal transmission g and local Andreev reflection $g^{\rm LAR}$ can be calculated separately. In fact, even the crossed Andreev reflection $g^{\rm CAR}$ can be computed. Hence, at least numerically, when conductance of $\frac{1}{2}\frac{e^2}{h}$ are found, one can inspect these scattering coefficients individually and substantiate the claim that CMEMs give rise to equal probability in all scattering processes, if all three of g, $g^{\rm LAR}$ and $g^{\rm CAR}$ are given by $1/4$. This is indeed what we find, but in order not to encumber the already saturated figures, we do not display any results for $g^{\rm CAR}$.

4.5.3 Higher half-quantized plateaus by periodic driving

Pursuing the discussion above, the picture of an incoming chiral regular fermion splitting into two CMEMs can then be generalized to the case of multiple edge modes, if complications such as momentum mismatch between edge modes and destructive interference do not occur. Working with Floquet systems, on top of this there is an additional Floquet replication in the frequency space [Figure 4.6], because the periodic driving fields open up conduction channels via photoabsorption/emission. If transport measurements involving summations over Floquet sidebands are performed, the stringent requirement that *each* sideband has equal scattering processes [Figures 4.5–4.8(c-d)] can likely rule out alternative mechanisms [98, 99] for the observation of half-quantized DC conductance.

It is now well established that periodic drives can generate phases with large topological invariants [166]. Nevertheless, the connection between topological invariants and the transport properties of such phases are not as straightforward. Above all, in a multiterminal transport setting, a Floquet sum rule is needed for quantized transport signatures to resurface. In a hybrid device, one can no longer resort to the TKNN formula that relates the conductance to Berry phase, making the Floquet sum rule indispensable should one wish to probe nontrivial topology by edge state transport. Indeed, as mentioned in Section 4.4.3, even the appropriate Floquet winding invariant cannot characterize the DC conductance, since the presence of interfaces allow edge states to interfere with each other.

In the literature, two-dimensional topological superconductor with larger Chern numbers has been discussed in a different setting [244]. By embedding ferromagnetic atoms on a superconductor with strong spin-orbit coupling, the authors showed that the resulting Hamiltonians effectively host long-range hoppings, which favor phases with large invariants. Here, we take the Floquet approach: Starting from relatively simple two-band toy models, we seek large Chern number phases by exploiting periodic driving fields, which has been shown to also result in long-range hoppings [169]. A more critical difference is that here we focus on the transport signatures of CMEMs in a driven Chern insulator-topological superconductor-Chern insulator heterostructure. Thus, one can ascertain the topology by distinctive half-quantized plateaus, and the equality of Andreev-normal scattering processes at all sidebands.

4.5.4 Perspectives on DC transport in Floquet hybrid device

When studying transport in heterostructures consisting of different Floquet topological matter, a critical requirement is that the device must be driven *in its entirety*. We shall take the FlCI-FTSC-FlCI junction to illustrate this point. If instead of FlCIs, we have static Chern insulators on the two sides, then either (i) they serve as leads, or (ii) they are parts of the sample that connect to metallic leads. For case (i), since the superconductor is driven, to completely reconstitute the edge mode at quasienergy $\epsilon = E_{\mathrm{F}} \in [-\hbar\Omega/2, \hbar\Omega/2]$, one must sum the DC conductance at different Floquet sidebands $E_n = E_{\mathrm{F}} + n\hbar\Omega$. Yet the spectrum of the CI lead does not extend beyond $n = 0$ [see Figure 4.12 where the dimly colored bands are absent]. Thus one can only retrieve the part of the CMEM lying in the $n = 0$ Floquet zone [Figure 4.12(a)], and the rest gives zero DC conductance because there are no states at sidebands $n \neq 0$ from the static lead.

Consider now case (ii). If the CIs are part of the sample, which contains a driven TSC, then Floquet theory demands that the CIs be treated as being trivially driven, i.e. they form identical copies in the Floquet space that do not couple with each other.

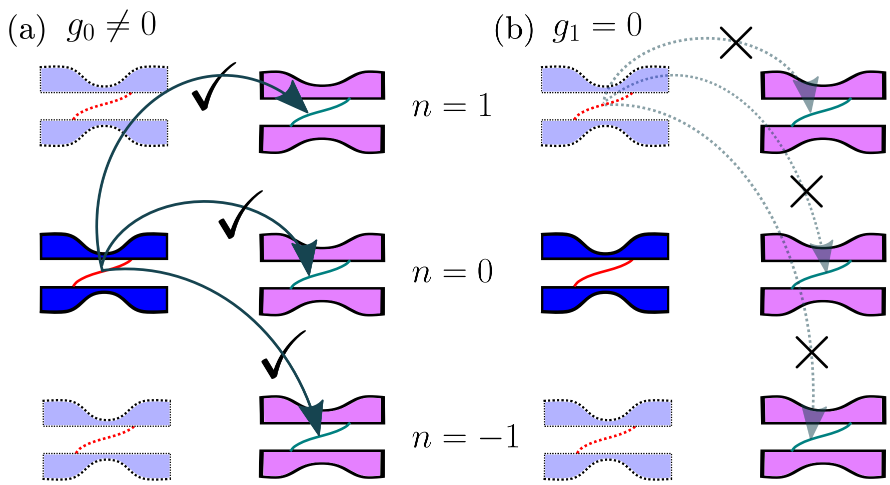

Figure 4.12: A static Chern insulator lead can only retrieve a single part of the chiral Majorana edge modes, because it is not Floquet-replicated, and there are no states beyond its static spectrum to contribute to the Floquet sum rule. For a fixed m, the DC conductance $g_m(E_\mathrm{F})$ computes the transmission of an incoming mode at energy $E_\mathrm{F} + m\hbar\Omega$ via photoabsorption/emission (curved arrows) to the right lead. However, a Floquet mode at quasienergy $\epsilon = E_\mathrm{F} \in [-\hbar\Omega/2, \hbar\Omega/2]$ is scattered to all $E_n = E_\mathrm{F} + n\hbar\Omega$. Hence, to obtain quantized transport, a summation over the DC conductance is needed, as in Equation 4.13. (a): The chiral mode injected from the CI lead to the FTSC can access the part of the CMEMs at $n = 0$, yielding a non-vanishing DC conductance $g_0 \neq 0$. (b): Because the CI lead is undriven, it is not Floquet replicated, so its spectrum only exists within the $n = 0$ Floquet zone. Hence, the part of the CMEMs scattered to $n = 1$ cannot be accessed, giving a zero contribution $g_1 = 0$ to the Floquet sum rule.

Nevertheless, the frequency term is nonzero (because the TSC is driven), so there is an infinitude of possibilities (corresponding to different frequencies) for the Floquet zone to be folded. If the frequency is much smaller than the gap, then the chiral edge states will be buried by bulk sidebands from the other Floquet zones, so that the resulting system is no longer insulating [Figure 4.13(a)]. At the other extreme of large frequency driving fields, the Chern insulator spectrum trivially repeats itself over different Floquet zones [Figure 4.13(b)], which allows the different Chern insulator sidebands to participate in transport through the driven superconductor. Yet large

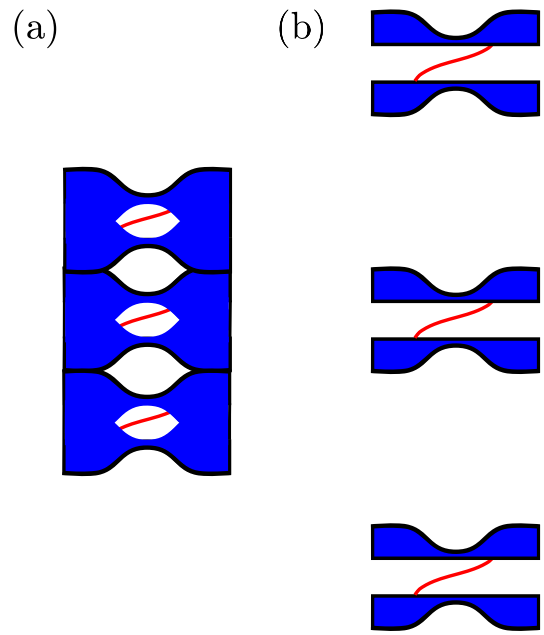

Figure 4.13: The consequences when the Chern insulators are treated as part of the sample, but are not driven. (a) For a frequency that is much smaller than the bandgap, the chiral edge modes will be buried by the Floquet bulk sidebands, so that the system becomes no longer insulating. (b) A frequency that is much larger than the band gap allows the trivially replicated sidebands to participate in transport, but the superconductor part, being driven by high frequency light, often will not exhibit remarkable Floquet physics.

frequencies only slightly renormalize some system parameters (except for gapless systems discussed in Section 4.4.2), so that truly interesting Floquet systems such as higher plateaus and π modes will not take place anyway.

Chapter 5

Enhanced higher harmonic generation from nodal topology

5.1 Preliminaries

Soon after Wan et al predicted the existence of a Weyl semimetal phase in pyrochlore iridates using first-principle calculations [52], Burkov et al presented a comprehensive study of a minimal model for Weyl and nodal line semimetal (NLSM) based on a topological-normal insulator superlattice [245]. NLSMs have since been observed in many materials, e.g. in the PbFCl-type structure ZrSiSe with Dirac-like crossings [246], and in the noncentrosymmetric superconductor $PbTaSe_2$ with Weyl-like crossings [214]. Compared to conventional topological insulators which fall into $\mathbb{Z}_2$ or $\mathbb{Z}$ classes [79], NLSMs possess far richer topology, with their nodal loops knotted or linked in unlimited topologically distinct ways [177]. Hypothetically speaking, even with only one nodal loop, the possible topologies are already infinite: The loop can cross itself from above or below any number of times, with each permutation leading to a multitude of other knotted configurations. Such is the richness of nodal-line topologies that no single invariant can unambiguously distinguish between all topologically distinct configurations.

From a single loop [247] to Hopf links [248], the quantum oscillations of NLSMs are actively investigated [249]. On the other hand, studies on the electrical transport are mostly restricted to a single loop [250, 251]. Here, by means of the semiclassical Boltzmann transport equation, we explore the effects of strong electric fields on the current response of a tight-binding model which captures the band-crossings in the room temperature magnet Co_2MnGa, arguably the most sophisticated NLSM identified to date. The topological linkages favor a sign-changing velocity profile in the Brillouin zone, leading to significant nonlinear current responses. The potential of such nodal network semimetals in nonlinear optics is further discussed.

5.2 Collisionless Boltzmann equation

From Equation 1.1, consider spatially homonegous system in the collisionless regime. Then, under an external electric field $\boldsymbol{E}(t) \sim \boldsymbol{E}(0)\mathrm{e}^{\mathrm{i}\omega t}$, the solution of the Boltzmann equation is given by:

$$f(\boldsymbol{k},t) = F\left[\epsilon\left(\boldsymbol{k} - \frac{-e}{\hbar}\int_{-\infty}^{t}\mathrm{d}t'\boldsymbol{E}(t')\right)\right] = F\left(\epsilon(\boldsymbol{k} - \frac{-e}{\hbar}\boldsymbol{A}(t))\right). \tag{5.1}$$

It expresses the nonequilibrium distribution function f as the usual Fermi distribution with wavevector shifted (minimally coupled) by an arbitrarily large impulse: $\boldsymbol{k} \to \boldsymbol{k} - (-e)\boldsymbol{A}(t)/\hbar$, where $\boldsymbol{A}(t) = \int_{-\infty}^{t}\mathrm{d}t'\boldsymbol{E}(t')$, and the electron charge is $-e < 0$. The above solution to the Boltzmann equation was used in Ref. [170] to discuss the nonlinear optical response of graphene.

Below we present a justification for neglecting the collision integral. Invoking the constant relaxation time approximation (discussed previously in Section 1.2.1), one has

$$\left(\frac{\partial}{\partial t} + \dot{\boldsymbol{p}}(t)\cdot\frac{\partial}{\partial \boldsymbol{p}}\right) f = \frac{F-f}{\tau}, \tag{5.2}$$

where f is the distribution function, $\boldsymbol{p} = \hbar \boldsymbol{k}$ the momentum. In presence of a periodic electric field of frequency Ω [which enters the equation via $\dot{\boldsymbol{p}}(t)$], it is reasonable to assume a periodic steady state, provided the driving force is not too weak and not too slow compared to the dissipative relaxing term. Then, a periodic average of the equation implies that the LHS is of the order $O(\Omega\tau)$, and the RHS of order $O(1)$, so that for $\Omega\tau \gg 1$, the collision term may be ignored altogether. This conforms to the intuition that scattering is not so relevant in presence of a fast driving field [252].

The theoretical descriptions of high harmonic generation in solids admit a spectrum of sophistication. For example, one may wish to examine the spatial distribution of the harmonics by taking a Wannier representation for the valence bands [253], or to study the contributions of interband current by adding an interband polarization term [254], or to account for the Coulomb interaction via a dephasing term [255]. For the purpose of illustrating the HHG due to topologically enforced nonlinearities in linked NLSMs, we considered only the intraband current within a non-interacting picture. This approach closely mirrors the theoretical model developed in the groundbreaking observation of HHG in bulk ZnO [256]. There, a Peierl's substitution of a continuous wave (cw) electric field is performed on a single band of ZnO. The current is computed by multiplying the velocity with the electron charge and density. Simply by taking into account longer-range hoppings, qualitative features including the linear energy cutoff of the experimental HHG can already be captured.

In our current expression,

$$\boldsymbol{J}[\boldsymbol{A}(t)] = e \int \frac{\mathrm{d}^3\boldsymbol{p}}{(2\pi\hbar)^3} F\left[\epsilon(\boldsymbol{p} - \boldsymbol{p}(t))\right] \boldsymbol{v}(\boldsymbol{p}), \tag{5.3}$$

upon a coordinate transformation, the electric field $\boldsymbol{p}(t)$ dependence turns up in the velocity, and the expression becomes similar to that in [256], with the exception that we integrate over the BZ instead of evaluating it at a certain momentum. We note that similar semi-classical approaches have subsequently been employed in [257] to discuss Bloch oscillations in HHG, as well as in [252] to study the role of Berry curvature in HHG of monolayer MoS_2.

With regards to scattering and many-body effects, rather reassuringly, they play only minor roles in HHG experiments [252, 258], in accordance with the intuition that most scattering cannot keep up with the fast driving field. Together with the fact that interactions are mostly insignificant in symmetry-protected topological materials, our approach may prove sufficient to describe HHG in nodal-line semimetals.

5.3 Nonlinear response

The magnetic Heusler compound Co_2MnGa was theoretically predicted in 2017 [136] to harbor a sophisticated network of band-crossings. In an experimental work using ARPES [71], the intricate nodal structure of Co_2MnGa was revealed to contain Hopf links, inner and outer chains at the Fermi energy, as shown in Figure 5.1, confirming the theoretical predictions in Ref. [136].

As illustrated in Figure 5.1, Co_2MnGa contains six linked NLs (red) which are shaped like flower petals (Figure 5.1(a)). They touch smaller, circular nodal loops (blue), dubbed “outer chains”, as shown in Figure 5.1(b). These blue loops are, in turn, in contact with four smaller, also circular nodal loops (green), as in Figure 5.1(c), forming another set of outer chains. Finally, the green rings touch the red flower petals, constituting an “inner chain” (Figure 5.1(d)). All these features of Co_2MnGa contribute to a strongly nonlinear response curve [Figure 5.2(a)], yielding high harmonic coefficients on par with that of graphene [Figure 5.5(a)]. These results were computed from a

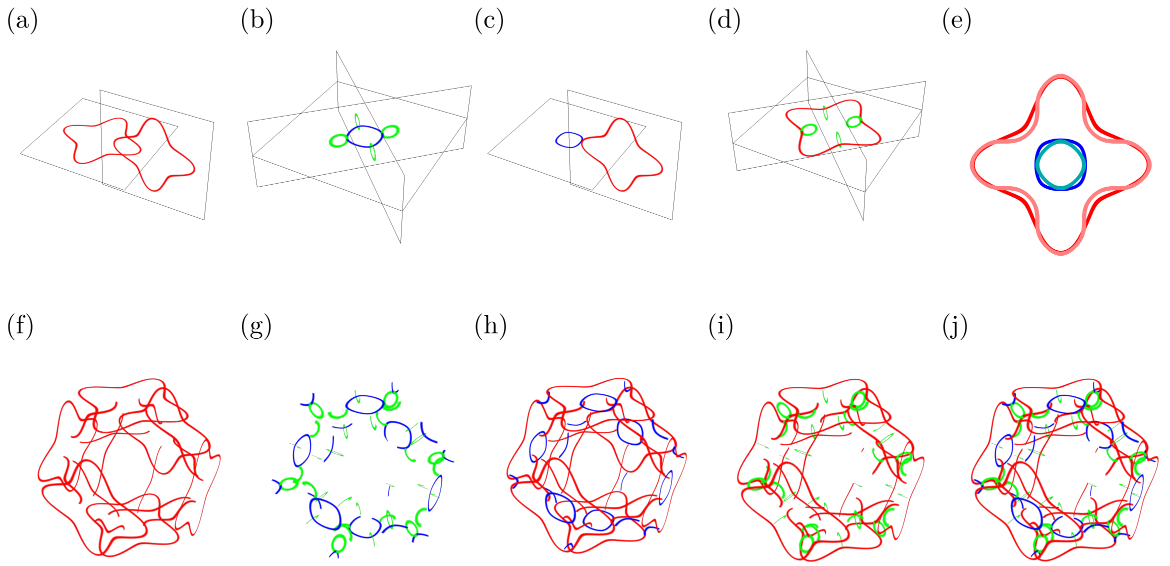

Figure 5.1: The assembly of all the nodal features of Co_2MnGa into a linked nodal network. Mostly saliently, it involves Hopf links [Figure 5.1(a),(f)], inner chains [Figure 5.1(d),(i)] and outer chains [Figure 5.1(b-c),(g-h)]. Specifically, it consists of a (a) Hopf link between red flower petals, (b) outer chain involving a blue loop and four smaller green loops, (c) outer chain formed by a blue loop and a flower petal, (d) inner chain due to a flower petal and four green rings. These features form sub-networks of linkages: (f) Network of Hopf links, (g) network of outer chains formed from blue and green loops, (h) network of outer chains formed from blue loops and red flower petals, (i) network of inner chains, which together form the full nodal network (j). Within it, the red flower petals and blue loops occupies the greatest volume and hence dominate the response. As shown in (e), their Fermi surfaces are decently approximated by our two-band model (pink flower petal and cyan loop). For simplicity, all nodal structures are displayed not in the first Brillouin zone (a truncated octahedron), but on a cube twice its size.

tight-binding model fitted to first-principle calculation results [136], which is given in Appendix F for completeness.

The characteristically kink response curve of Co_2MnGa gives rise to large odd harmonics, and can be pedagogically explained via a detailed breakdown of its various topological NL linkages. We shall focus on the six red flower petals and the six blue rings, which are the dominant current contributors (largest features in Figure 5.1(j)). Their individual contributions can be isolated through a two-band approximate model which is amenable to analytic decomposition as follows:

$$H_{\mathrm{Co_2MnGa}}(\boldsymbol{k}) = \mathrm{Re}[h(\boldsymbol{k})]\sigma_1 + \mathrm{Im}[h(\boldsymbol{k})]\sigma_3, \tag{5.4}$$

where $h(\boldsymbol{k}) = \Pi_{n=1}^{6}\{u_n(\boldsymbol{k}) + \mathrm{i}v_n(\boldsymbol{k})\}$, which is a product of constituent nodal structures described by

$$\begin{aligned} u_{\mathrm{even}}(\boldsymbol{k}) &= [\cos^3(k_x/2) + \cos^3(k_y/2) + \cos^3(k_z/2) - m], \\ u_{\mathrm{odd}}(\boldsymbol{k}) &= [\cos^3(k_x/2) + \cos^3(k_y/2) + \cos^3(k_z/2) + m]. \end{aligned} \tag{5.5}$$

and $v_{1,2}(\boldsymbol{k}) = \sin(k_x/2)$, $v_{3,4}(\boldsymbol{k}) = \sin(k_y/2)$, $v_{5,6}(\boldsymbol{k}) = \sin(k_z/2)$, the parameter $m = -0.5$ chosen so that the Fermi surface approximates that of Co_2MnGa. Remarkably, such a simple construction yields a rather accurate reconstruction of the Fermi surface of Co_2MnGa, as illustrated by its cross section comparison in Figure 5.1(e) and the 3D superimposition in Figure 5.2(c). Based on this approximate model, we can extract and compare the response contributions of the individual dominant NLs of $CoMn_2Ga$, which are the six flower petals and rings re-labeled cyan, magenta, blue, yellow, red and green in Figure 5.2(c). Interestingly, for an applied driving field along one of the rectangular coordinate axes i.e. $\hat{\boldsymbol{y}}$, all these nodal structures obey only two possible response curves (type I: yellow and blue, type II: magenta, green, red, cyan). This follows from the

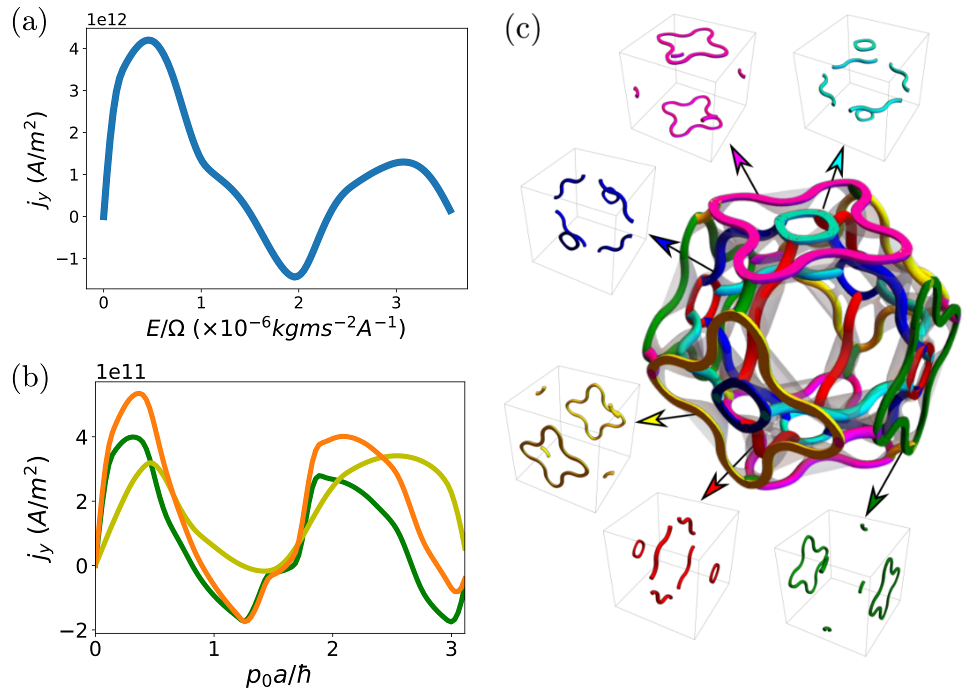

Figure 5.2: Decomposition of the current response of Co_2MnGa into those of its constituent nodal features. (c) Breakdown of its nodal structure into dominant nodal Hopf flower petals and rings whose linkages are further detailed in Figure 5.1. (a) Current response of the actual tight-binding model of Co_2MnGa. (b) Total current response (orange, scaled down by a factor of four for clarity) from the sum of green/magenta/red/cyan and yellow/blue nodal structure responses, which correspond to only two unique curves due to cubic symmetry.

cubic symmetry of Co_2MnGa, and enables a transparent reconstruction of the overall response.

The two possible responses are presented in Figure 5.3, where the green and yellow response curves correspond respectively to the contributions of the representative green and yellow nodal structures from Figure 5.2(c). Curves from the other structures are equivalent to one of these, and are omitted for brevity. Together, both response curves exhibit large kinks, with their contrasting behavior at larger fields interfering to give rise to even more pronounced non-linearity and hence HHG properties, as detailed in the

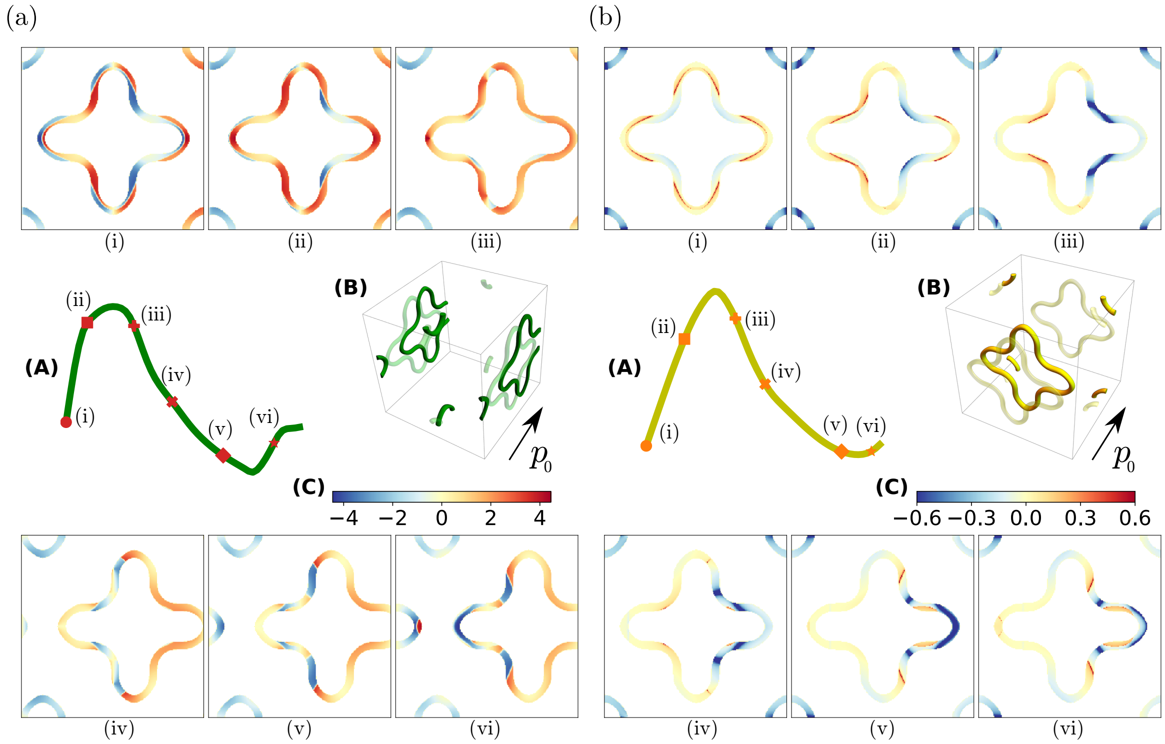

Figure 5.3: (a,b): (A) response curves of the green/yellow Hopf flower petals in the directions indicated by the impulse p_0, as illustrated in the insets (B). The response curve shapes at various impulse strengths (i-vi) can be understood through integrating the explicit electronic group velocity profiles within the petals, as illustrated in the corresponding upper and lower panels. Legend colorbars (C) for the group velocities are given in units of $\times 10^5$ ms^{-1}.

Methods. Their total contribution, plotted in Figure 5.2(b), indeed qualitatively agrees with the full response curve from Figure 5.2(a) despite considerable simplifications[1].

5.4 Velocity field

The velocity field of Co_2MnGa, as illustrated in Figure 5.4 here, is the basis of detailed analysis of the shape of its response current. We consider the current contribution of

[1]Not only are various smaller nodal features omitted from the dispersion, the matching of the Fermi surfaces are also restricted to the individual features.

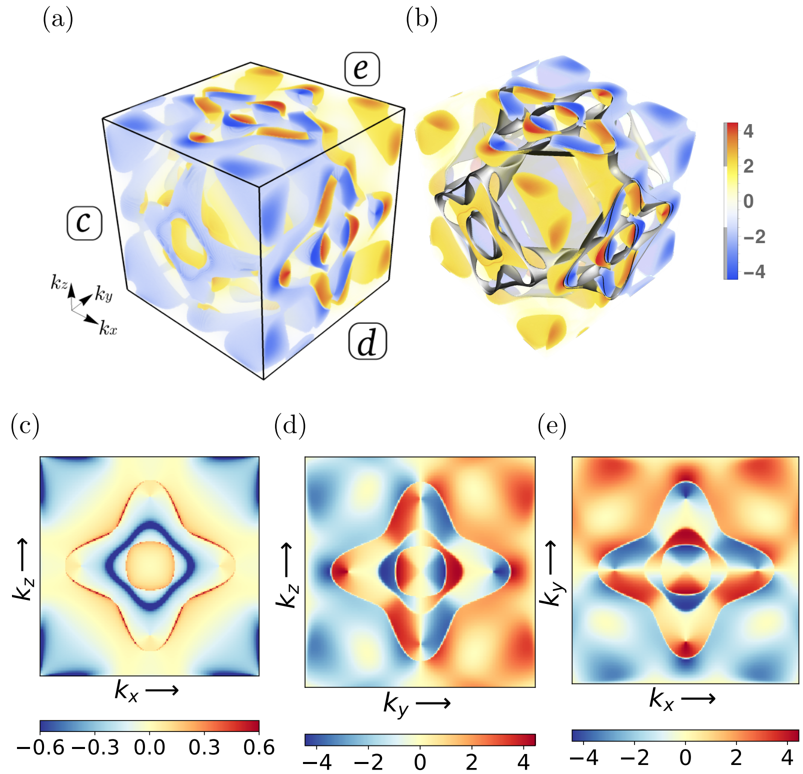

Figure 5.4: (a) The density plot of v_y, i.e. the y-component of the group velocity of the third band (ordered from high to low energies) of the tight-binding model of Co_2MnGa. The choice of the velocity component is arbitrary owing to the cubic symmetry of Co_2MnGa. The planes labeled (c-e) correspond to the cross sections on which we display v_y below. (b) A rotated view of (a), overlaid by the Fermi surface of Co_2MnGa. (c) Density plot of v_y restricted on the k_z-k_x plane at $k_y = -2\pi/a$. (d) Density plot of v_y on the k_z-k_y plane at $k_x = 2\pi/a$. (e) Density plot of v_y on the k_y-k_x plane at $k_z = 2\pi/a$. All color bars are expressed in units of $\times 10^5\,\mathrm{ms}^{-1}$.

the green and yellow nodal structures in the top panel of Figure 5.2(c). In (A) we mark several points for the drift p_0, and study the resulting drifted Fermi surface, as well as the change of the velocity occupied by it. The sharp increase from (i) to (ii) is a consequence of the rapidly varying velocity field, as soon as the Fermi surface is driven even slightly away from equilibrium. This sharp increase soon saturates and begins to fall as the flower petal is shifted away from the intense red patches situated near the touching points of the inner and outer chains [(ii) to (iv)]. Going from (iv) to (v), the current eventually changes sign because the intense blue patches are now being sampled, The current slowly becomes positive again [(v) to (vi)] when the flower petal is shifted to the outer chain [Figure 5.1(b)].

In contrast to the current due to the green nodal structure [Figure 5.3(a)(A)], the gradient of the current is not as steep for the yellow structure [Figure 5.3(b)(A)]. Furthermore, the yellow circular ring also contribute exclusively negative velocity [Figure 5.3(b)(i-vi)] within the drift considered here, unlike the green one where the regions occupied by the ring vary in sign [Figure 5.3(a)(i-vi)]. These observations, together with the evolution of the velocity field similar to that discussed in the previous paragraph, can account for the current pattern of the yellow nodal structure.

The above analysis demonstrates how the strong inhomogeneity of the velocity field, which results from the knotted links and touching loops, gives rise to its characteristic response. Indeed, on the two high symmetry planes displayed in Figure 5.4(d-e), the flower petals are clearly discernible as contours of sign-changing points. As shown in Figure 5.4(b), the Fermi surface of Co_2MnGa fits matchingly the void of the velocity field. By visualizing the velocity fields of simpler artificial nodal links (not shown), we observe that the more complicated a nodal network, the more often the velocity field switches direction. Our analysis holds best for small chemical potentials that results in thin NLs, even though the response curve usually remains qualitatively preserved as the chemical potential is increased (not shown), unless the NLs become so thick that they fuse and generate different nodal topologies.

5.5 High harmonic generation

Consider a sinusoidal time-varying applied electric field signal $\boldsymbol{E}(t) = \boldsymbol{E}_0 \cos \Omega t$, which corresponds to the vector potential $\boldsymbol{A}(t) = \boldsymbol{A} \sin \Omega t$, where $\boldsymbol{A} = \frac{\boldsymbol{E}_0}{\Omega} = \frac{\boldsymbol{p_0} a}{\hbar}$, $\boldsymbol{p}_0$ the impulse amplitude vector and a the lattice spacing of the nodal material lattice. The greater the nonlinearity of the current response function $\boldsymbol{J}(\boldsymbol{A})$, the larger is the extent of HHG. The extent of signal distortion between chosen direction components i and j can be quantified via Fourier coefficient ratios c_n describing the higher harmonics:

$$\begin{aligned} J_j(A_i(t)) &= J_j\left(A \sin \Omega t\right) \\ &\propto \sin \Omega t + \sum_{n \neq 0} c_n \sin(n\Omega t). \end{aligned} \tag{5.6}$$

The leading nonlinear response is also quantified by the third harmonic generation (3HHG) and Kerr coefficients. Expanding Equation 5.6 up to the third order and considering only the longitudinal components for simplicity, we can write the response current in a chosen direction as $J = \alpha A + \beta A^3$. The third order response, which is proportional to β, can be further classified into the 3HHG and Kerr contributions with frequencies 3Ω and Ω respectively.

The high harmonic generations of Co_2MnGa are displayed in Figure 5.5(a). For comparison, we also calculate the same quantities for graphene, based on the nearest-neighbor tight-binding model with energy dispersion:

$$\epsilon(k_x, k_y) = t_1 \sqrt{x^2(k_x, k_y) + y^2(k_x, k_y)} \tag{5.7}$$

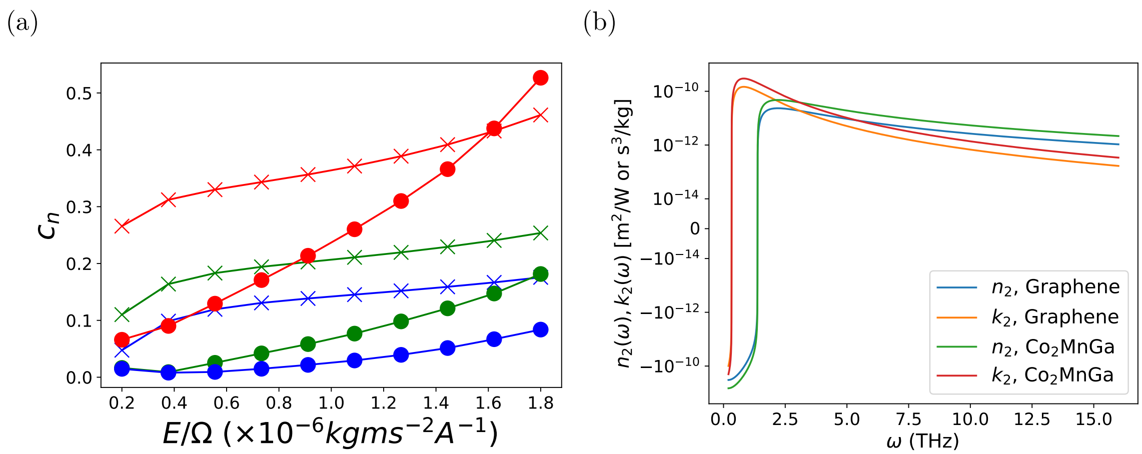

Figure 5.5: Nonlinear optics with the nodal network semimetal Co_2MnGa and graphene. (a): High harmonic generation in Co_2MnGa ($\bullet$) and graphene ($\times$), with red, green, blue denoting the $n = 3, 5, 7$ harmonics respectively. (b): Nonlinear refractive index in Co_2MnGa and graphene. For Co_2MnGa, the chemical potential is at 0.15 eV. For graphene, the chemical potential is at 0.12 eV. The temperature is at 300 K for both.

with $t_1 = 2.8\,\text{eV}$ and

$$\begin{aligned} x(k_x, k_y) &= \cos\frac{k_1 + k_2}{3} + \cos\frac{k_2 - 2k_1}{3} + \cos\frac{k_1 - 2k_2}{3}, \\ y(k_x, k_y) &= \sin\frac{k_1 + k_2}{3} + \sin\frac{k_2 - 2k_1}{3} + \sin\frac{k_1 - 2k_2}{3}, \\ k_1 &= \frac{3}{2}k_x + \frac{\sqrt{3}}{2}k_y, \\ k_2 &= \frac{3}{2}k_x - \frac{\sqrt{3}}{2}k_y. \end{aligned} \tag{5.8}$$

In Figure 5.5(a), while the high harmonic coefficients of graphene ($\times$) are superior to Co_2MnGa ($\bullet$), it is rather reassuring that they remain in the same order magnitude, at least for the third harmonic (red). At larger applied field ($E/\Omega > 1.6\times 10^{-6}\,\text{kgms}^{-2}\text{A}^{-1}$), the third harmonic of Co_2MnGa even surpasses that of graphene.

The potential of the nodal network semimetal Co_2MnGa as a nonlinear optical material is further illustrated in Figure 5.5(b), where we observe larger magnitude of the nonlinear refractive index of Co_2MnGa compared to graphene. The nonlinear refractive indices were computed using the del Coso-Solis relation [259]: From the 3HHG coefficient $\sigma^{(3)}$, define the third-order optical susceptibility:

$$\chi^{(3)}(\omega) = \frac{\mathrm{i}\sigma^{(3)}(\omega)}{3\epsilon_0\omega}. \tag{5.9}$$

Then the real and imaginary parts of the nonlinear refractive index is given by:

$$\begin{aligned} n_2(\omega) &= \frac{3}{4\epsilon_0 c[n^2(\omega)+k^2(\omega)]}\left[\mathrm{Re}\chi^{(3)}(\omega) + \frac{k(\omega)}{n(\omega)}\mathrm{Im}\chi^{(3)}(\omega)\right], \\ k_2(\omega) &= \frac{3}{4\epsilon_0 c[n^2(\omega)+k^2(\omega)]}\left[\mathrm{Im}\chi^{(3)}(\omega) - \frac{k(\omega)}{n(\omega)}\mathrm{Re}\chi^{(3)}(\omega)\right], \end{aligned} \tag{5.10}$$

where $n(\omega), k(\omega)$ are the real and imaginary parts of the refractive index:

$$n(\omega) + \mathrm{i}k(\omega) = \sqrt{1 + \frac{\mathrm{i}\sigma^{(1)}(\omega)}{\epsilon_0\omega}}, \tag{5.11}$$

and $\sigma^{(1)}(\omega)$ is the linear conductivity. To allow for comparisons between Co_2MnGa, a bulk material, with graphene, a monolayer 2D material, an artificial thickness of $d = 0.7\,\mathrm{nm}$ is assumed for graphene. The choice of chemical potentials is motivated by the requirement of $k_F\ell \ll 1$ for the validity of Boltzmann theory [260], with k_F the Fermi wavevector and ℓ the transport mean free path.

Within the same theoretical approach, the nodal semimetal Co_2MnGa is no match for graphene in terms of HHG [Figure 5.5(a)], and its nonlinear refractive index only beats graphene over a narrow margin, in particular instances of the chemical potentials. Yet the design and fabrication of 3D bulk materials are more mature than their 2D counterparts. The presence of an additional spatial dimension also allows for more flexibility, which is particularly attractive for photonic devices because electromagnetic (EM) waves respond strongly to the geometrical shapes of nanostructures. Interesting phenomena such as the self-focusing of EM waves [261] are also more easily observed in 3D systems. Taken together, it is hoped that the present study of nonlinear transport in a simple model for Co_2MnGa may motivate further investigations on the technological potential of such peculiar topological nodal chains and links semimetals.

Chapter 6

Conclusion and Outlook

6.1 Conclusion

In Chapter 2, we theoretically and computationally studied how Floquet topological phases with many edge state channels may lead to robust transport in a two-terminal setup. Under the Keldysh-NEGF framework and using the recursive Floquet-Green's function method, we have investigated the two-terminal DC conductance, time-averaged LDOS and local DC profile of a harmonically-driven Hofstadter model in several parameter regimes. Thanks to the Floquet sum rule, we are able to observe tunable and quantized Floquet edge state transport, with the largest DC conductance demonstrated in this work being $8e^2/h$. We have also presented a detailed comparison among Floquet chiral, counter-propagating and symmetric-restricted edge states regarding their robustness to disorder and defects. Our results indicate that in terms of transport, Floquet chiral edge modes are the most resistant to sample imperfections. We have also shown that, even after invoking the Floquet sum rule, one cannot guarantee quantization of the DC conductance of Floquet edge modes, if the bandwidth of the lead is not wide enough.

In Chapter 3, we proposed a general approach to generate a rich variety of topological phases. This task is made straightforward, at least in theory, by directly engineering the dispersion relations of their topological surface states. In particular, a semimetal phase with a single 3D nodal loop is subject to a gap term of various forms of 2D spin-orbit coupling. Under certain conditions, the 3D nodal-loop semimetal phase alone fully controls the existence of surface states, and the gap term we introduce takes complete charge of the dispersion relation of surface states. Not only is this insight expected to be useful in generating many interesting phases, we also highlight four intriguing phases in this work: (i) a chiral topological insulator with two-fold degenerate surface Dirac cones, (ii) an insulator with two-fold degenerate surface loop, (iii) a Weyl semimetal with four disconnected Fermi arcs, and (iv) a second-order topological insulator with 1D surface states along the hinges of a 3D system. When necessary, we have also discussed the symmetry protection and topological invariants of these phases. Two-terminal transport calculations complement and confirm our analyses, offering a possibility to distinguish between these four topological phases.

In Chapter 4, we have investigated the two-terminal transport of Floquet chiral Majorana fermions in several model topological insulator-superconductor heterostructures. The main finding is that upon invoking the Floquet sum rule, Floquet CMEMs not only admit the intriguing $\frac{1}{2}\frac{e^2}{h}$ conductance plateaus that are currently under extensive investigations [98, 99, 242], they can also yield conductance plateaus quantized at larger half-integers. This study thus makes a computational observation of higher-than-1/2 conductance plateaus in hybrid topological junctions and demonstrates the possibility, at least in principle, of creating multiple pairs of Floquet CMEMs in FTSC. While alternative mechanisms not based on CMEMs may also yield conductance plateaus at $\frac{1}{2}\frac{e^2}{h}$ [98, 99], it is unlikely that these mechanisms can produce higher half-quantized plateaus upon a subtle sum rule from models with a minimal number of bands. Other detailed results obtained in this work can also guide future quantum transport studies of Floquet topological devices. Finally, we stress that the continuous driving fields considered in this work are within experimental feasibility using cold atoms, as exemplified by the realization of Haldane insulator [237] via Floquet theory. Equally encouraging is the fact that quantum transport studies can be performed on optical lattices [262, 263]. Thus the finding that Floquet CMEMs admit equal probabilities for normal transmission and local Andreev reflection *at all Floquet sidebands* may serve as a first test in experiments prior to observing the more challenging quantized plateaus.

In Chapter 5, we uncovered a very physically measurable consequence of topological nodal linkages, namely that they enhance and protect the HHG of optical radiation, which can be useful for terahertz applications. As such, the sophisticated topology of nodal knots and link networks are no longer mere mathematical curiosities, but are in principle reconstructible from nonlinear response data in various directions. By venturing beyond the perturbative regime, we are able to access the effect of field impulses comparable to the size of NLs, and unveil the key role of nontrivial nodal linkages in enhancing the HHG already known to exist in simple nodal structures [134]. Our results rigorously hold in the ballistic limit, which correspond to the terahertz regime for scattering times expected of high mobility samples of known nodal materials. Due to the robustness of our HHG mechanism, the characteristically superior HHG from nodal linkages is likely to extend beyond the ballistic and semiclassical limits, at least until hot phonon or interband scattering dominate. Despite our semiclassical analysis, our results crucially rely on the Fermi sea condensation of electrons, which is fundamentally due to the exclusion principle. As such, they are distinct from signatures of nodal geometry proposed in purely classical settings, such as topolectrical resonances due to nodal drumhead states [264].

6.2 Outlook

Based on the results presented in Chapter 2, several directions deserve further investigations. Most important of all, we note that it remains unclear how to exploit the tunability of Floquet topological matter to *directly* realize large, robust, and quantized DC conductance at a given chemical potential (namely, without using the Floquet sum rule). Second, an asymmetry of the transmission coefficients T_{LR} and T_{RL} may result in a pumped current [185]. This aspect is not considered here but is definitely an interesting prospect. For example, under which scenarios does one obtain a non-vanishing pumped current, thereby realizing a Floquet edge state pump? Third, while the transport of Floquet chiral edge modes is immune to lattice imperfections, it is not clear whether this remains the case in presence of interactions. This constitutes a direction awaiting more studies [192, 195] in its own right.

To pursue further studies beyond Chapter 3, we recall that nodal line semimetals with gapless linked loops [248] have been introduced, which provide richer bases in engineering different topological phases. In these systems, the projection of the loops may wind around certain regions in the 2D surface BZ multiple times, resulting in higher degeneracy of the "drumhead" states. As these nodal lines are also protected by the $\mathcal{PT}$ symmetry, we can introduce gap terms in the same way, which affect only the eigenenergies of surface states, but not their existence. Therefore, our work also paves the way for future studies on the connections between the well-established topological phases and the more exotic knotted semimetals.

The physics of chiral Majorana edge modes underlying Chapter 4 remains a vibrant research area [101]. This is especially so after a recent preprint investigating the contact transparency in various magnetic TIs–Nb heterostructures suggested that the half quantized conductance may be a consequence of the superconductor shunting the QAH insulators [100]. Since QAHIs with larger Chern numbers have been experimentally found [27, 28], it is of interests to study such systems proximitized by s-wave superconductors, e.g. how the momentum separations of the multiple edge modes will affect the resulting transport profiles.

Lastly, an obvious extension of Chapter 5 will be to relax the collisionless approximation in the Boltzmann equation. One can specify a collision mechanism of interests, and explicity compute the relaxation time as was done in Ref. [265]. Doing so on the nodal semimetal Co_2MnGa requires generalizing the method to deal with anisotropic band dispersions, similar to Ref. [266] which considered directional relaxation times for a two-dimensional electron gas with spin-orbit coupling. More sophisticated treatments of HHG that take into account interband effects would also be very desirable, considering the gapless nature of the bandstructure of Co_2MnGa.

Bibliography

[1] C. L. Kane and E. J. Mele, Phys. Rev. Lett. **95**, 226801 (2005).

[2] P. Delplace, J. B. Marston, and A. Venaille, Science **358**, 1075 (2017).

[3] G. E. Volovik and V. P. Mineev, Soviet Journal of Experimental and Theoretical Physics Letters **23**, 593 (1976).

[4] D. J. Thouless, M. Kohmoto, M. P. Nightingale, and M. den Nijs, Phys. Rev. Lett. **49**, 405 (1982).

[5] M. Z. Hasan and C. L. Kane, Rev. Mod. Phys. **82**, 3045 (2010).

[6] X.-L. Qi and S.-C. Zhang, Rev. Mod. Phys. **83**, 1057 (2011).

[7] F. Reis, G. Li, L. Dudy, M. Bauernfeind, S. Glass, W. Hanke, R. Thomale, J. Schäfer, and R. Claessen, Science **357**, 287 (2017).

[8] A. Roth, C. Brüne, H. Buhmann, L. W. Molenkamp, J. Maciejko, X.-L. Qi, and S.-C. Zhang, Science **325**, 294 (2009).

[9] S. Murakami, N. Nagaosa, and S.-C. Zhang, Phys. Rev. Lett. **93**, 156804 (2004).

[10] F. D. M. Haldane, Phys. Rev. Lett. **61**, 2015 (1988).

[11] C. L. Kane and E. J. Mele, Phys. Rev. Lett. **95**, 146802 (2005).

[12] L. Fu and C. L. Kane, Phys. Rev. B **76**, 045302 (2007).

[13] M. Sakano, K. Okawa, M. Kanou, H. Sanjo, T. Okuda, T. Sasagawa, and K. Ishizaka, Nat. Commun **6**, 8595 (2015).

[14] M. König, S. Wiedmann, C. Brüne, A. Roth, H. Buhmann, L. W. Molenkamp, X.-L. Qi, and S.-C. Zhang, Science **318**, 766 (2007).

[15] S. Wu, V. Fatemi, Q. D. Gibson, K. Watanabe, T. Taniguchi, R. J. Cava, and P. Jarillo-Herrero, Science **359**, 76 (2018).

[16] K. Kandrai, G. Kukucska, P. Vancsó, J. Koltai, G. Baranka, Z. E. Horváth, Á. Hoffmann, A. Vymazalová, L. Tapasztó, and P. Nemes-Incze, (2019), arXiv:`1903.02458`.

[17] J. L. Collins, A. Tadich, W. Wu, L. C. Gomes, J. N. B. Rodrigues, C. Liu, J. Hellerstedt, H. Ryu, S. Tang, S.-K. Mo, S. Adam, S. A. Yang, M. S. Fuhrer, and M. T. Edmonds, Nature **564**, 390 (2018).

[18] K. v. Klitzing, G. Dorda, and M. Pepper, Phys. Rev. Lett. **45**, 494 (1980).

[19] E. Hall, The London, Edinburgh, and Dublin Philosophical Magazine and Journal of Science **12**, 157 (1881).

[20] X.-L. Qi, Y.-S. Wu, and S.-C. Zhang, Phys. Rev. B **74**, 085308 (2006).

[21] C.-X. Liu, X.-L. Qi, X. Dai, Z. Fang, and S.-C. Zhang, Phys. Rev. Lett. **101**, 146802 (2008).

[22] Z. Qiao, S. A. Yang, W. Feng, W.-K. Tse, J. Ding, Y. Yao, J. Wang, and Q. Niu, Phys. Rev. B **82**, 161414 (2010).

[23] C.-Z. Chang, J. Zhang, X. Feng, J. Shen, Z. Zhang, M. Guo, K. Li, Y. Ou, P. Wei, L.-L. Wang, Z.-Q. Ji, Y. Feng, S. Ji, X. Chen, J. Jia, X. Dai, Z. Fang, S.-C. Zhang, K. He, Y. Wang, L. Lu, X.-C. Ma, and Q.-K. Xue, Science **340**, 167 (2013).

[24] C. Fang, M. J. Gilbert, and B. A. Bernevig, Phys. Rev. Lett. **112**, 046801 (2014).

[25] H. Jiang, Z. Qiao, H. Liu, and Q. Niu, Phys. Rev. B **85**, 045445 (2012).

[26] S. A. Skirlo, L. Lu, Y. Igarashi, Q. Yan, J. Joannopoulos, and M. Soljačić, Phys. Rev. Lett. **115**, 253901 (2015).

[27] G. Jiang, Y. Feng, W. Wu, S. Li, Y. Bai, Y. Li, Q. Zhang, L. Gu, X. Feng, D. Zhang, C. Song, L. Wang, W. Li, X.-C. Ma, Q.-K. Xue, Y. Wang, and K. He, Chinese Physics Letters **35**, 076802 (2018).

[28] J. Ge, Y. Liu, J. Li, H. Li, T. Luo, Y. Wu, Y. Xu, and J. Wang, (2019), arXiv:`1907.09947`.

[29] G. Chen, A. L. Sharpe, E. J. Fox, Y.-H. Zhang, S. Wang, L. Jiang, B. Lyu, H. Li, K. Watanabe, T. Taniguchi, Z. Shi, T. Senthil, D. Goldhaber-Gordon, Y. Zhang, and F. Wang, (2019), arXiv:`1905.06535`.

[30] M. Serlin, C. L. Tschirhart, H. Polshyn, Y. Zhang, J. Zhu, K. Watanabe, T. Taniguchi, L. Balents, and A. F. Young, (2019), arXiv:`1907.00261`.

[31] L. Fu, *Rational design of magnetic topological insulators*, (2019) `https://doi.org/10.36471/JCCM_October_2019_03` (visited on 11/13/2019).

[32] L. Fu, Phys. Rev. Lett. **106**, 106802 (2011).

[33] T. H. Hsieh, H. Lin, J. Liu, W. Duan, A. Bansil, and L. Fu, Nat. Commun **3**, 982 (2012).

[34] Y. Tanaka, Z. Ren, T. Sato, K. Nakayama, S. Souma, T. Takahashi, K. Segawa, and Y. Ando, Nat. Phys. **8**, 800 (2012).

[35] W. A. Benalcazar, B. A. Bernevig, and T. L. Hughes, Science **357**, 61 (2017).

[36] F. Schindler, Z. Wang, M. G. Vergniory, A. M. Cook, A. Murani, S. Sengupta, A. Y. Kasumov, R. Deblock, S. Jeon, I. Drozdov, H. Bouchiat, S. Guéron, A. Yazdani, B. A. Bernevig, and T. Neupert, Nat. Phys. **14**, 918 (2018).

[37] S. Raghu, X.-L. Qi, C. Honerkamp, and S.-C. Zhang, Phys. Rev. Lett. **100**, 156401 (2008).

[38] I. Garate, Phys. Rev. Lett. **110**, 046402 (2013).

[39] B. A. Bernevig, T. L. Hughes, and S.-C. Zhang, Science **314**, 1757 (2006).

[40] J. Li, R.-L. Chu, J. K. Jain, and S.-Q. Shen, Phys. Rev. Lett. **102**, 136806 (2009).

[41] C. W. Groth, M. Wimmer, A. R. Akhmerov, J. Tworzydło, and C. W. J. Beenakker, Phys. Rev. Lett. **103**, 196805 (2009).

[42] S. Stützer, Y. Plotnik, Y. Lumer, P. Titum, N. H. Lindner, M. Segev, M. C. Rechtsman, and A. Szameit, Nature **560**, 461 (2018).

[43] E. J. Meier, F. A. An, A. Dauphin, M. Maffei, P. Massignan, T. L. Hughes, and B. Gadway, Science **362**, 929 (2018).

[44] G. W. Semenoff, Phys. Rev. Lett. **53**, 2449 (1984).

[45] E. Fradkin, E. Dagotto, and D. Boyanovsky, Phys. Rev. Lett. **57**, 2967 (1986).

[46] K. Chang, *An experiment in zurich brings us nearer to a black hole's mysteries*, (2017) `https://www.nytimes.com/2017/07/19/science/mixed-axial-gravitational-anomaly-weyl-semimetals-ibm.html` (visited on 11/15/2019).

[47] I. Johnston, *'angel particle' which is both matter and anti-matter discovered in 'landmark' quantum physics breakthrough*, (2017) `https://www.independent.co.uk/news/science/angel-particle-anti-matter-quantum-physics-discover-stanford-university-california-irvine-a7851661.html` (visited on 11/15/2019).

[48] K. S. Novoselov, A. K. Geim, S. V. Morozov, D. Jiang, M. I. Katsnelson, I. V. Grigorieva, S. V. Dubonos, and A. A. Firsov, Nature **438**, 197 (2005).

[49] Y. Zhang, Y.-W. Tan, H. L. Stormer, and P. Kim, Nature **438**, 201 (2005).

[50] Y. Yao, F. Ye, X.-L. Qi, S.-C. Zhang, and Z. Fang, Phys. Rev. B **75**, 041401 (2007).

[51] C. Dutreix, H. González-Herrero, I. Brihuega, M. I. Katsnelson, C. Chapelier, and V. T. Renard, Nature **574**, 219 (2019).

[52] X. Wan, A. M. Turner, A. Vishwanath, and S. Y. Savrasov, Phys. Rev. B **83**, 205101 (2011).

[53] A. C. Potter, I. Kimchi, and A. Vishwanath, Nat. Commun **5**, 5161 (2014).

[54] C. M. Wang, H.-P. Sun, H.-Z. Lu, and X. C. Xie, Phys. Rev. Lett. **119**, 136806 (2017).

[55] P. J. W. Moll, N. L. Nair, T. Helm, A. C. Potter, I. Kimchi, A. Vishwanath, and J. G. Analytis, Nature **535**, 266 (2016).

[56] C. Zhang, Y. Zhang, X. Yuan, S. Lu, J. Zhang, A. Narayan, Y. Liu, H. Zhang, Z. Ni, R. Liu, E. S. Choi, A. Suslov, S. Sanvito, L. Pi, H.-Z. Lu, A. C. Potter, and F. Xiu, Nature **565**, 331 (2019).

[57] Z. Wang, H. Weng, Q. Wu, X. Dai, and Z. Fang, Phys. Rev. B **88**, 125427 (2013).

[58] K. Deng, G. Wan, P. Deng, K. Zhang, S. Ding, E. Wang, M. Yan, H. Huang, H. Zhang, Z. Xu, J. Denlinger, A. Fedorov, H. Yang, W. Duan, H. Yao, Y. Wu, S. Fan, H. Zhang, X. Chen, and S. Zhou, Nat. Phys. **12**, 1105 (2016).

[59] B. Q. Lv, Z.-L. Feng, Q.-N. Xu, X. Gao, J.-Z. Ma, L.-Y. Kong, P. Richard, Y.-B. Huang, V. N. Strocov, C. Fang, H.-M. Weng, Y.-G. Shi, T. Qian, and H. Ding, Nature **546**, 627 (2017).

[60] N. B. M. Schröter, D. Pei, M. G. Vergniory, Y. Sun, K. Manna, F. de Juan, J. A. Krieger, V. Süss, M. Schmidt, P. Dudin, B. Bradlyn, T. K. Kim, T. Schmitt, C. Cacho, C. Felser, V. N. Strocov, and Y. Chen, Nat. Phys. **15**, 759 (2019).

[61] C. Fang, H. Weng, X. Dai, and Z. Fang, Chinese Physics B **25**, 117106 (2016).

[62] W. Wu, Y. Liu, S. Li, C. Zhong, Z.-M. Yu, X.-L. Sheng, Y. X. Zhao, and S. A. Yang, Phys. Rev. B **97**, 115125 (2018).

[63] C. Fang, Y. Chen, H.-Y. Kee, and L. Fu, Phys. Rev. B **92**, 081201 (2015).

[64] G. Bian, T.-R. Chang, H. Zheng, S. Velury, S.-Y. Xu, T. Neupert, C.-K. Chiu, S.-M. Huang, D. S. Sanchez, I. Belopolski, N. Alidoust, P.-J. Chen, G. Chang, A. Bansil, H.-T. Jeng, H. Lin, and M. Z. Hasan, Phys. Rev. B **93**, 121113 (2016).

[65] J. Liu and L. Balents, Phys. Rev. B **95**, 075426 (2017).

[66] A. N. Rudenko, E. A. Stepanov, A. I. Lichtenstein, and M. I. Katsnelson, Phys. Rev. Lett. **120**, 216401 (2018).

[67] S. Pezzini, M. R. van Delft, L. M. Schoop, B. V. Lotsch, A. Carrington, M. I. Katsnelson, N. E. Hussey, and S. Wiedmann, Nat. Phys. **14**, 178 (2018).

[68] S.-Y. Yang, H. Yang, E. Derunova, S. S. P. Parkin, B. Yan, and M. N. Ali, Advances in Physics: X **3**, 1414631 (2018).

[69] W. Chen, H.-Z. Lu, and J.-M. Hou, Phys. Rev. B **96**, 041102 (2017).

[70] Z. Yan, R. Bi, H. Shen, L. Lu, S.-C. Zhang, and Z. Wang, Phys. Rev. B **96**, 041103 (2017).

[71] I. Belopolski, K. Manna, D. S. Sanchez, G. Chang, B. Ernst, J. Yin, S. S. Zhang, T. Cochran, N. Shumiya, H. Zheng, B. Singh, G. Bian, D. Multer, M. Litskevich, X. Zhou, S.-M. Huang, B. Wang, T.-R. Chang, S.-Y. Xu, A. Bansil, C. Felser, H. Lin, and M. Z. Hasan, Science **365**, 1278 (2019).

[72] G. Volovik, *The universe in a helium droplet*, International Series of Monographs on Physics (OUP Oxford, 2009).

[73] D. Vollhardt and P. Wolfle, *The superfluid phases of helium 3*, Dover Books on Physics (Dover Publications, 2013).

[74] D. A. Ivanov, Phys. Rev. Lett. **86**, 268 (2001).

[75] X. G. Wen, International Journal of Modern Physics B **04**, 239 (1990).

[76] T. H. Hansson, V. Oganesyan, and S. L. Sondhi, Annals of Physics **313**, 497 (2004).

[77] Y. S. Hor, A. J. Williams, J. G. Checkelsky, P. Roushan, J. Seo, Q. Xu, H. W. Zandbergen, A. Yazdani, N. P. Ong, and R. J. Cava, Phys. Rev. Lett. **104**, 057001 (2010).

[78] L. Fu and E. Berg, Phys. Rev. Lett. **105**, 097001 (2010).

[79] A. P. Schnyder, S. Ryu, A. Furusaki, and A. W. W. Ludwig, Phys. Rev. B **78**, 195125 (2008).

[80] L. Fu, Phys. Rev. B **90**, 100509 (2014).

[81] M. Hecker and J. Schmalian, npj Quantum Materials **3**, 26 (2018).

[82] C.-w. Cho, J. Shen, J. Lyu, S. H. Lee, Y. S. Hor, M. Hecker, J. Schmalian, and R. Lortz, (2019), arXiv:1905.01702.

[83] K. Matano, M. Kriener, K. Segawa, Y. Ando, and G.-q. Zheng, Nat. Phys. **12**, 852 (2016).

[84] T. Asaba, B. J. Lawson, C. Tinsman, L. Chen, P. Corbae, G. Li, Y. Qiu, Y. S. Hor, L. Fu, and L. Li, Phys. Rev. X **7**, 011009 (2017).

[85] A. Pustogow, Y. Luo, A. Chronister, Y.-S. Su, D. A. Sokolov, F. Jerzembeck, A. P. Mackenzie, C. W. Hicks, N. Kikugawa, S. Raghu, E. D. Bauer, and S. E. Brown, Nature **574**, 72 (2019).

[86] A. P. Mackenzie and Y. Maeno, Rev. Mod. Phys. **75**, 657 (2003).

[87] L. Fu and C. L. Kane, Phys. Rev. Lett. **100**, 096407 (2008).

[88] R. Balian and N. R. Werthamer, Phys. Rev. **131**, 1553 (1963).

[89] J. Alicea, Phys. Rev. B **81**, 125318 (2010).

[90] J. D. Sau, S. Tewari, R. M. Lutchyn, T. D. Stanescu, and S. Das Sarma, Phys. Rev. B **82**, 214509 (2010).

[91] J. Wang, Q. Zhou, B. Lian, and S.-C. Zhang, Phys. Rev. B **92**, 064520 (2015).

[92] T. Stanescu and S. Tewari, J. Phys. Condens. Matter **25**, 233201 (2013).

[93] V. Mourik, K. Zuo, S. M. Frolov, S. R. Plissard, E. P. A. M. Bakkers, and L. P. Kouwenhoven, Science **336**, 1003 (2012).

[94] Q. L. He, L. Pan, A. L. Stern, E. C. Burks, X. Che, G. Yin, J. Wang, B. Lian, Q. Zhou, E. S. Choi, K. Murata, X. Kou, Z. Chen, T. Nie, Q. Shao, Y. Fan, S.-C. Zhang, K. Liu, J. Xia, and K. L. Wang, Science **357**, 294 (2017).

[95] X.-L. Qi, T. L. Hughes, and S.-C. Zhang, Phys. Rev. B **82**, 184516 (2010).

[96] S. B. Chung, X.-L. Qi, J. Maciejko, and S.-C. Zhang, Phys. Rev. B **83**, 100512 (2011).

[97] J. T. Chalker and P. D. Coddington, J. Phys. C: Solid State Physics **21**, 2665 (1988).

[98] Y. Huang, F. Setiawan, and J. D. Sau, Phys. Rev. B **97**, 100501 (2018).

[99] W. Ji and X.-G. Wen, Phys. Rev. Lett. **120**, 107002 (2018).

[100] M. Kayyalha, D. Xiao, R. Zhang, J. Shin, J. Jiang, F. Wang, Y.-F. Zhao, L. Zhang, K. M. Fijalkowski, P. Mandal, M. Winnerlein, C. Gould, Q. Li, L. W. Molenkamp, M. H. W. Chan, N. Samarth, and C.-Z. Chang, (2019), arXiv:`1904.06463`.

[101] J. Wang and B. Lian, Phys. Rev. Lett. **121**, 256801 (2018).

[102] A. Y. Kitaev, Phys.-Uspekhi **44**, 131 (2001).

[103] W. P. Su, J. R. Schrieffer, and A. J. Heeger, Phys. Rev. B **22**, 2099 (1980).

[104] H. Zhang, C.-X. Liu, S. Gazibegovic, D. Xu, J. A. Logan, G. Wang, N. van Loo, J. D. S. Bommer, M. W. A. de Moor, D. Car, R. L. M. O. het Veld, P. J. van Veldhoven, S. Koelling, M. A. Verheijen, M. Pendharkar, D. J. Pennachio, B. Shojaei, J. S. Lee, C. J. Palmstrom, E. P. A. M. Bakkers, S. Das Sarma, and L. P. Kouwenhoven, Nature **556**, 74 (2018).

[105] S. Nadj-Perge, I. K. Drozdov, J. Li, H. Chen, S. Jeon, J. Seo, A. H. MacDonald, B. A. Bernevig, and A. Yazdani, Science **346**, 602 (2014).

[106] N. Hao and J. Hu, National Science Review **6**, 213 (2018).

[107] P. Zhang, Z. Wang, X. Wu, K. Yaji, Y. Ishida, Y. Kohama, G. Dai, Y. Sun, C. Bareille, K. Kuroda, T. Kondo, K. Okazaki, K. Kindo, X. Wang, C. Jin, J. Hu, R. Thomale, K. Sumida, S. Wu, K. Miyamoto, T. Okuda, H. Ding, G. D. Gu, T. Tamegai, T. Kawakami, M. Sato, and S. Shin, Nat. Phys. **15**, 41 (2019).

[108] P. Zhang, K. Yaji, T. Hashimoto, Y. Ota, T. Kondo, K. Okazaki, Z. Wang, J. Wen, G. D. Gu, H. Ding, and S. Shin, Science **360**, 182 (2018).

[109] D. Wang, L. Kong, P. Fan, H. Chen, S. Zhu, W. Liu, L. Cao, Y. Sun, S. Du, J. Schneeloch, R. Zhong, G. Gu, L. Fu, H. Ding, and H.-J. Gao, Science (2018) 10.1126/science.aao1797.

[110] L. Fu, *Majorana in iron superconductors & pairing of spin-helical electrons*, (2019) http://online.itp.ucsb.edu/online/tpqm-c19/fu/pdf/Fu_TPQM19Conf_KITP.pdf (visited on 11/18/2019).

[111] T. Oka and S. Kitamura, Annu. Rev. Condens. Matter Phys **10**, 387 (2019).

[112] J. Wang and J. Gong, Phys. Rev. A **77**, 031405 (2008).

[113] T. Oka and H. Aoki, Phys. Rev. B **79**, 081406 (2009).

[114] N. H. Lindner, G. Refael, and V. Galitski, Nat. Phys. **7**, 490 (2011).

[115] M. S. Rudner and N. H. Lindner, (2019), arXiv:1909.02008.

[116] Y. H. Wang, H. Steinberg, P. Jarillo-Herrero, and N. Gedik, Science **342**, 453 (2013).

[117] E. J. Sie, J. W. McIver, Y.-H. Lee, L. Fu, J. Kong, and N. Gedik, Nat. Mater. **14**, 290 (2014).

[118] J. Kim, X. Hong, C. Jin, S.-F. Shi, C.-Y. S. Chang, M.-H. Chiu, L.-J. Li, and F. Wang, Science **346**, 1205 (2014).

[119] J. W. McIver, B. Schulte, F.-U. Stein, T. Matsuyama, G. Jotzu, G. Meier, and A. Cavalleri, Nat. Phys., 1 (2019).

[120] Y. Yang, Z. Gao, H. Xue, L. Zhang, M. He, Z. Yang, R. Singh, Y. Chong, B. Zhang, and H. Chen, Nature **565**, 622 (2019).

[121] F. Li, X. Huang, J. Lu, J. Ma, and Z. Liu, Nat. Phys. **14**, 30 (2017).

[122] S. Imhof, C. Berger, F. Bayer, J. Brehm, L. W. Molenkamp, T. Kiessling, F. Schindler, C. H. Lee, M. Greiter, T. Neupert, and R. Thomale, Nat. Phys. **14**, 925 (2018).

[123] C. H. Lee, S. Imhof, C. Berger, F. Bayer, J. Brehm, L. W. Molenkamp, T. Kiessling, and R. Thomale, Commun. Phys. **1**, 39 (2018).

[124] T. Hofmann, T. Helbig, C. H. Lee, M. Greiter, and R. Thomale, Phys. Rev. Lett. **122**, 247702 (2019).

[125] Z.-C. Gu and X.-G. Wen, Phys. Rev. B **80**, 155131 (2009).

[126] X.-G. Wen, Rev. Mod. Phys. **89**, 041004 (2017).

[127] X. Chen, Z.-C. Gu, Z.-X. Liu, and X.-G. Wen, Phys. Rev. B **87**, 155114 (2013).

[128] A. Kitaev, Annals of Physics **303**, 2 (2003).

[129] R. B. Laughlin, Phys. Rev. Lett. **50**, 1395 (1983).

[130] L. Boltzmann, K. Acad. Wiss.(Wein) Sitzb., II Abt **66** (1872).

[131] R. Kubo, *The boltzmann equation* (Springer, 1973), pp. 301–340.

[132] D. Xiao, M.-C. Chang, and Q. Niu, Rev. Mod. Phys. **82**, 1959 (2010).

[133] C. H. Lee, Y. Wang, Y. Chen, and X. Zhang, Phys. Rev. B **98**, 094434 (2018).

[134] T. Morimoto, S. Zhong, J. Orenstein, and J. E. Moore, Phys. Rev. B **94**, 245121 (2016).

[135] D. Shin, Y. Lee, M. Sasaki, Y. H. Jeong, F. Weickert, J. B. Betts, H.-J. Kim, K.-S. Kim, and J. Kim, Nat. Mater. **16**, 1096 (2017).

[136] G. Chang, S.-Y. Xu, X. Zhou, S.-M. Huang, B. Singh, B. Wang, I. Belopolski, J. Yin, S. Zhang, A. Bansil, H. Lin, and M. Z. Hasan, Phys. Rev. Lett. **119**, 156401 (2017).

[137] S. Adam, P. W. Brouwer, and S. Das Sarma, Phys. Rev. B **79**, 201404 (2009).

[138] B. Altshuler and A. Aronov, *Electron–electron interactions in disordered systems*, edited by A. EFROS and M. POLLAK, Vol. 10, Modern Problems in Condensed Matter Sciences (Elsevier, 1985), pp. 1–153.

[139] A. Lucas and K. C. Fong, J. Phys. Condens. Matter **30**, 053001 (2018).

[140] O. Kashuba, B. Trauzettel, and L. W. Molenkamp, Phys. Rev. B **97**, 205129 (2018).

[141] M. J. M. de Jong and L. W. Molenkamp, Phys. Rev. B **51**, 13389 (1995).

[142] C. Beenakker and H. van Houten, in *Semiconductor heterostructures and nanostructures*, Vol. 44, edited by H. Ehrenreich and D. Turnbull, Solid State Physics (Academic Press, 1991), pp. 1–228.

[143] M. Büttiker, Phys. Rev. Lett. **57**, 1761 (1986).

[144] J. Wang, B. Lian, H. Zhang, and S.-C. Zhang, Phys. Rev. Lett. **111**, 086803 (2013).

[145] I. T. Rosen, E. J. Fox, X. Kou, L. Pan, K. L. Wang, and D. Goldhaber-Gordon, npj Quantum Materials **2**, 69 (2017).

[146] A. I. Volokitin and B. N. J. Persson, Rev. Mod. Phys. **79**, 1291 (2007).

[147] H. H. Yap and J.-S. Wang, Phys. Rev. E **95**, 012126 (2017).

[148] L. Kadanoff and G. Baym, *Quantum statistical mechanics: green's function methods in equilibrium and nonequilibrium problems*, Frontiers in physics (W.A. Benjamin, 1962).

[149] L. M. Canonico, T. G. Rappoport, and R. B. Muniz, Phys. Rev. Lett. **122**, 196601 (2019).

[150] P. Haughian, H. H. Yap, J. Gong, and T. L. Schmidt, Phys. Rev. B **96**, 195432 (2017).

[151] J.-W. Jiang, J.-S. Wang, and B. Li, J. Appl. Phys **109**, 014326 (2011).

[152] G. Tang, H. H. Yap, J. Ren, and J.-S. Wang, Phys. Rev. Applied **11**, 031004 (2019).

[153] N. Nagaosa, *Quantum field theory in condensed matter physics*, Texts and monographs in physics (Springer, 1999).

[154] J. Peng, H. H. Yap, G. Zhang, and J.-S. Wang, (2017), arXiv:1703.07113.

[155] G. Tang and J.-S. Wang, Phys. Rev. B **98**, 125401 (2018).

[156] M. Brandbyge, J.-L. Mozos, P. Ordejón, J. Taylor, and K. Stokbro, Phys. Rev. B **65**, 165401 (2002).

[157] C.-C. Kaun, B. Larade, H. Mehrez, J. Taylor, and H. Guo, Phys. Rev. B **65**, 205416 (2002).

[158] B. K. Nikolić, K. Dolui, M. D. Petrović, P. Plecháč, T. Markussen, and K. Stokbro, *First-principles quantum transport modeling of spin-transfer and spin-orbit torques in magnetic multilayers* (Springer International Publishing, 2018), pp. 1–35.

[159] H. Haug and A.-P. Jauho, *Quantum kinetics in transport and optics of semiconductors* (Springer, New York, 2008).

[160] G. Stefanucci and R. van Leeuwen, *Nonequilibrium many-body theory of quantum systems: a modern introduction* (Cambridge University Press, 2013).

[161] Y. Meir and N. S. Wingreen, Phys. Rev. Lett. **68**, 2512 (1992).

[162] P. A. Khomyakov, G. Brocks, V. Karpan, M. Zwierzycki, and P. J. Kelly, Phys. Rev. B **72**, 035450 (2005).

[163] Z.-Y. Ong and G. Zhang, Phys. Rev. B **91**, 174302 (2015).

[164] D. S. Fisher and P. A. Lee, Phys. Rev. B **23**, 6851 (1981).

[165] D. Y. H. Ho and J. Gong, Phys. Rev. Lett. **109**, 010601 (2012).

[166] T.-S. Xiong, J. Gong, and J.-H. An, Phys. Rev. B **93**, 184306 (2016).

[167] L. Li, C. Yin, S. Chen, and M. A. N. Araújo, Phys. Rev. B **95**, 121107 (2017).

[168] H. Zhang, C.-X. Liu, X.-L. Qi, X. Dai, Z. Fang, and S.-C. Zhang, Nat. Phys. **5**, 438 (2009).

[169] Q.-J. Tong, J.-H. An, J. Gong, H.-G. Luo, and C. H. Oh, Phys. Rev. B **87**, 201109 (2013).

[170] S. A. Mikhailov, Europhys. Lett. **79**, 27002 (2007).

[171] R. W. Boyd, *Nonlinear optics* (Elsevier, 2003).

[172] X. Zhang, J. Wang, and S.-C. Zhang, Phys. Rev. B **82**, 245107 (2010).

[173] D. Sticlet, F. Piéchon, J.-N. Fuchs, P. Kalugin, and P. Simon, Phys. Rev. B **85**, 165456 (2012).

[174] M. S. Rudner, N. H. Lindner, E. Berg, and M. Levin, Phys. Rev. X **3**, 031005 (2013).

[175] P. Leboeuf, J. Kurchan, M. Feingold, and D. P. Arovas, Phys. Rev. Lett. **65**, 3076 (1990).

[176] R. Wang, B. Wang, R. Shen, L. Sheng, and D. Y. Xing, Europhys. Lett. **105**, 17004 (2014).

[177] L. Li, C. H. Lee, and J. Gong, Phys. Rev. Lett. **121**, 036401 (2018).

[178] F. Nathan, D. Abanin, E. Berg, N. H. Lindner, and M. S. Rudner, Phys. Rev. B **99**, 195133 (2019).

[179] A. Altland and M. R. Zirnbauer, Phys. Rev. B **55**, 1142 (1997).

[180] R. Webb, New Scientist **224**, 38 (2014).

[181] C. Bruder and H. Schoeller, Phys. Rev. Lett. **72**, 1076 (1994).

[182] M. Moskalets and M. Büttiker, Phys. Rev. B **66**, 205320 (2002).

[183] S. Kohler, J. Lehmann, and P. Hänggi, Phys. Rep. **406**, 379 (2005).

[184] S. Datta, *Electronic transport in mesoscopic systems* (Cambridge University Press, UK, 1995).

[185] L. E. F. Foa Torres, P. M. Perez-Piskunow, C. A. Balseiro, and G. Usaj, Phys. Rev. Lett. **113**, 266801 (2014).

[186] A. Kundu and B. Seradjeh, Phys. Rev. Lett. **111**, 136402 (2013).

[187] A. Farrell and T. Pereg-Barnea, Phys. Rev. B **93**, 045121 (2016).

[188] M. Fruchart, P. Delplace, J. Weston, X. Waintal, and D. Carpentier, Physica E Low Dimens. Syst. Nanostruct. **75**, 287 (2016).

[189] I. C. Fulga and M. Maksymenko, Phys. Rev. B **93**, 075405 (2016).

[190] Z. Gu, H. A. Fertig, D. P. Arovas, and A. Auerbach, Phys. Rev. Lett. **107**, 216601 (2011).

[191] H. Dehghani, T. Oka, and A. Mitra, Phys. Rev. B **91**, 155422 (2015).

[192] H. Aoki, N. Tsuji, M. Eckstein, M. Kollar, T. Oka, and P. Werner, Rev. Mod. Phys. **86**, 779 (2014).

[193] A.-P. Jauho, N. S. Wingreen, and Y. Meir, Phys. Rev. B **50**, 5528 (1994).

[194] J.-S. Wang, J. Wang, and J. T. Lü, Eur. Phys. J. B **62**, 381 (2008).

[195] N. Tsuji, T. Oka, and H. Aoki, Phys. Rev. B **78**, 235124 (2008).

[196] J. C. Cuevas and E. Scheer, *Molecular electronics: an introduction to theory and experiment* (World Scientific, Singapore, 2010).

[197] C. H. Lewenkopf and E. R. Mucciolo, J. Comput. Electron. **12**, 203 (2013).

[198] T. Mikami, S. Kitamura, K. Yasuda, N. Tsuji, T. Oka, and H. Aoki, Phys. Rev. B **93**, 144307 (2016).

[199] T. Kitagawa, T. Oka, A. Brataas, L. Fu, and E. Demler, Phys. Rev. B **84**, 235108 (2011).

[200] Z. Zhou, I. I. Satija, and E. Zhao, Phys. Rev. B **90**, 205108 (2014).

[201] A. R. Kolovsky and G. Mantica, Phys. Rev. B **86**, 054306 (2012).

[202] J. H. Shirley, Phys. Rev. **138**, B979 (1965).

[203] H. Sambe, Phys. Rev. A **7**, 2203 (1973).

[204] G. Stefanucci and C.-O. Almbladh, Phys. Rev. B **69**, 195318 (2004).

[205] D. Y. H. Ho and J. Gong, Phys. Rev. B **90**, 195419 (2014).

[206] P. Titum, E. Berg, M. S. Rudner, G. Refael, and N. H. Lindner, Phys. Rev. X **6**, 021013 (2016).

[207] M. Fujita, K. Wakabayashi, K. Nakada, and K. Kusakabe, J. Phys. Soc. Jpn. **65**, 1920 (1996).

[208] M. C. Rechtsman, J. M. Zeuner, Y. Plotnik, Y. Lumer, D. Podolsky, F. Dreisow, S. Nolte, M. Segev, and A. Szameit, Nature **496**, 196 (2013).

[209] R. Fleury, A. B. Khanikaev, and A. Alù, Nat. Commun. **7**, 11744 (2016).

[210] X. Wan, A. M. Turner, A. Vishwanath, and S. Y. Savrasov, Phys. Rev. B **83**, 205101 (2011).

[211] R. Yu, H. Weng, Z. Fang, X. Dai, and X. Hu, Phys. Rev. Lett. **115**, 036807 (2015).

[212] A. A. Burkov, M. D. Hook, and L. Balents, Phys. Rev. B **84**, 235126 (2011).

[213] L.-K. Lim and R. Moessner, Phys. Rev. Lett. **118**, 016401 (2017).

[214] G. Bian, T.-R. Chang, R. Sankar, S.-Y. Xu, H. Zheng, T. Neupert, C.-K. Chiu, S.-M. Huang, G. Chang, I. Belopolski, et al., Nat. Commun **7**, 10556 (2016).

[215] J. Hu, Z. Tang, J. Liu, X. Liu, Y. Zhu, D. Graf, K. Myhro, S. Tran, C. N. Lau, J. Wei, and Z. Mao, Phys. Rev. Lett. **117**, 016602 (2016).

[216] J. Langbehn, Y. Peng, L. Trifunovic, F. von Oppen, and P. W. Brouwer, Phys. Rev. Lett. **119**, 246401 (2017).

[217] F. Schindler, A. M. Cook, M. G. Vergniory, Z. Wang, S. S. P. Parkin, B. A. Bernevig, and T. Neupert, Science Advances **4** (2018) `10.1126/sciadv.aat0346`.

[218] R. S. K. Mong and V. Shivamoggi, Phys. Rev. B **83**, 125109 (2011).

[219] P. Hosur, S. Ryu, and A. Vishwanath, Phys. Rev. B **81**, 045120 (2010).

[220] L. Li and M. A. N. Araújo, Phys. Rev. B **94**, 165117 (2016).

[221] G. Chang, S.-Y. Xu, D. S. Sanchez, S.-M. Huang, C.-C. Lee, T.-R. Chang, G. Bian, H. Zheng, I. Belopolski, N. Alidoust, H.-T. Jeng, A. Bansil, H. Lin, and M. Z. Hasan, Science Advances **2** (2016) `10.1126/sciadv.1600295`.

[222] C. Caroli, R. Combescot, D. Lederer, P. Nozieres, and D. Saint-James, J. Phys. C: Solid State Phys. **4**, 916 (1971).

[223] Y. Takane, Journal of the Physical Society of Japan **85**, 124711 (2016).

[224] R. M. Lutchyn, E. P. A. M. Bakkers, L. P. Kouwenhoven, P. Krogstrup, C. M. Marcus, and Y. Oreg, Nat. Rev. Mater **3**, 52 (2018).

[225] C.-Z. Chen, Y.-M. Xie, J. Liu, P. A. Lee, and K. T. Law, Phys. Rev. B **97**, 104504 (2018).

[226] Y. Zeng, C. Lei, G. Chaudhary, and A. H. MacDonald, Phys. Rev. B **97**, 081102 (2018).

[227] S. D. Sarma, M. Freedman, and C. Nayak, npj Quantum Inf. **1**, 15001 (2015).

[228] C. Laflamme, M. A. Baranov, P. Zoller, and C. V. Kraus, Phys. Rev. A **89**, 022319 (2014).

[229] J.-S. Xu, K. Sun, Y.-J. Han, C.-F. Li, J. K. Pachos, and G.-C. Guo, Nat. Commun. **7**, 13194 (2016).

[230] D. N. Basov, R. D. Averitt, and D. Hsieh, Nat. Mater. **16**, 1077 (2017).

[231] Y.-G. Peng, C.-Z. Qin, D.-G. Zhao, Y.-X. Shen, X.-Y. Xu, M. Bao, H. Jia, and X.-F. Zhu, Nat. Commun. **7**, 13368 (2016).

[232] C. H. Lee, G. Li, G. Jin, Y. Liu, and X. Zhang, Phys. Rev. B **97**, 085110 (2018).

[233] C. Chamon, R. Jackiw, Y. Nishida, S.-Y. Pi, and L. Santos, Phys. Rev. B **81**, 224515 (2010).

[234] P. D. Sacramento, Phys. Rev. B **91**, 214518 (2015).

[235] J. Wang, Phys. Rev. B **98**, 024519 (2018).

[236] B. Lian, X.-Q. Sun, A. Vaezi, X.-L. Qi, and S.-C. Zhang, PNAS **115**, 10938 (2018).

[237] G. Jotzu, M. Messer, R. Desbuquois, M. Lebrat, T. Uehlinger, D. Greif, and T. Esslinger, Nature **515**, 237 (2014).

[238] H. H. Yap, L. Zhou, J.-S. Wang, and J. Gong, Phys. Rev. B **96**, 165443 (2017).

[239] F. A. Rasmussen, “Properties and transport characteristics of majorana fermions in nanowires”, MA thesis (University of Cophenhagen, 2012).

[240] Q.-F. Sun and X. C. Xie, J. Phys. Condens. Matter **21**, 344204 (2009).

[241] J. K. Chin, D. E. Miller, Y. Liu, C. Stan, W. Setiawan, C. Sanner, K. Xu, and W. Ketterle, Nature **443**, 961 (2006).

[242] B. Lian, J. Wang, X.-Q. Sun, A. Vaezi, and S.-C. Zhang, Phys. Rev. B **97**, 125408 (2018).

[243] M. P. Anantram and S. Datta, Phys. Rev. B **53**, 16390 (1996).

[244] J. Röntynen and T. Ojanen, Phys. Rev. Lett. **114**, 236803 (2015).

[245] A. A. Burkov, M. D. Hook, and L. Balents, Phys. Rev. B **84**, 235126 (2011).

[246] J. Hu, Z. Tang, J. Liu, X. Liu, Y. Zhu, D. Graf, K. Myhro, S. Tran, C. N. Lau, J. Wei, and Z. Mao, Phys. Rev. Lett. **117**, 016602 (2016).

[247] H. Yang, R. Moessner, and L.-K. Lim, Phys. Rev. B **97**, 165118 (2018).

[248] Y. Zhou, F. Xiong, X. Wan, and J. An, Phys. Rev. B **97**, 155140 (2018).

[249] J. Hu, S.-Y. Xu, N. Ni, and Z. Mao, Annu. Rev. Mater. Res. **49**, 207 (2019).

[250] W. B. Rui, Y. X. Zhao, and A. P. Schnyder, Phys. Rev. B **97**, 161113 (2018).

[251] S. P. Mukherjee and J. P. Carbotte, Phys. Rev. B **95**, 214203 (2017).

[252] H. Liu, Y. Li, Y. S. You, S. Ghimire, T. F. Heinz, and D. A. Reis, Nat. Phys. **13**, 262 (2017).

[253] E. N. Osika, A. Chacón, L. Ortmann, N. Suárez, J. A. Pérez-Hernández, B. Szafran, M. F. Ciappina, F. Sols, A. S. Landsman, and M. Lewenstein, Phys. Rev. X **7**, 021017 (2017).

[254] G. Vampa, C. R. McDonald, G. Orlando, P. B. Corkum, and T. Brabec, Phys. Rev. B **91**, 064302 (2015).

[255] D. Golde, T. Meier, and S. W. Koch, J. Opt. Soc. Am. B **23**, 2559 (2006).

[256] S. Ghimire, A. D. DiChiara, E. Sistrunk, P. Agostini, L. F. DiMauro, and D. A. Reis, Nat. Phys. **7**, 138 (2011).

[257] O. Schubert, M. Hohenleutner, F. Langer, B. Urbanek, C. Lange, U. Huttner, D. Golde, T. Meier, M. Kira, S. W. Koch, et al., Nat. Photonics **8**, 119 (2014).

[258] G. Ndabashimiye, S. Ghimire, M. Wu, D. A. Browne, K. J. Schafer, M. B. Gaarde, and D. A. Reis, Nature **534**, 520 (2016).

[259] R. del Coso and J. Solis, J. Opt. Soc. Am. B **21**, 640 (2004).

[260] S. Adam, E. H. Hwang, V. M. Galitski, and S. Das Sarma, PNAS **104**, 18392 (2007).

[261] R. W. Boyd, S. G. Lukishova, and Y. R. Shen, *Self-focusing: past and present: fundamentals and prospects*, Vol. 114 (Springer Science & Business Media, 2008).

[262] M. Bruderer and W. Belzig, Phys. Rev. A **85**, 013623 (2012).

[263] S. Krinner, T. Esslinger, and J.-P. Brantut, J. Phys. Condens. Matter **29**, 343003 (2017).

[264] L. Li, C. H. Lee, and J. Gong, Commun. Phys. **2**, 135 (2019).

[265] D. Y. H. Ho, I. Yudhistira, N. Chakraborty, and S. Adam, Phys. Rev. B **97**, 121404 (2018).

[266] J. Schliemann and D. Loss, Phys. Rev. B **68**, 165311 (2003).

[267] L. Li and S. Chen, Europhys. Lett. **109**, 40006 (2015).

[268] U. Khanna, S. Rao, and A. Kundu, Phys. Rev. B **95**, 201115 (2017).

Appendix A

Recursive Floquet-Green's function method

The recursive Green's function method is a powerful method which speeds up calculations and reduces memory usage substantially. Here we follow Ref. [197] and extend the method to incorporate a periodic driving field. We first describe the simpler case for transmission, which involves a single, unidirectional renormalization of the left self energy. We then discuss the DC profile and the time-averaged LDOS, which involve N_x bidirectional renormalization of both left and right self energies.

A.1 DC conductance

Recall the expression for DC conductance:

$$T(E) = \sum_{k\in\mathbb{Z}} \mathrm{Tr}_\Lambda\Big[\boldsymbol{G}^r_{k0}\boldsymbol{\Gamma}^L_{00}\boldsymbol{G}^a_{0k}\boldsymbol{\Gamma}^R_{kk}\Big]. \tag{A.1}$$

This has a form that is almost identical to the static Caroli formula [162, 222], apart from the additional summation over Floquet indices. Thus consider the Floquet-Dyson equation Equation 2.13, which we write here as [199]:

$$[E\boldsymbol{I} + \hbar\boldsymbol{\Omega} - \boldsymbol{H} - \{\boldsymbol{\Sigma}^r_L(E) + \boldsymbol{\Sigma}^r_R(E)\}]\boldsymbol{G}^r(E) = \boldsymbol{I} \tag{A.2}$$

Let $n_{\mathrm{F}} = 2n_{\mathrm{H}} + 1$ be the truncation dimension (or Floquet dimension), where n_{H} is the number of harmonics. We write:

$$
\begin{aligned}
\boldsymbol{\Omega} &= \begin{bmatrix} -n_{\mathrm{H}}\Omega & & & & \\ & \ddots & & & \\ & & 0 & & \\ & & & \ddots & \\ & & & & n_{\mathrm{H}}\Omega \end{bmatrix}, \\
\boldsymbol{\Sigma}^r_{L/R}(E) &= \begin{bmatrix} \Sigma^r_{L/R}(E - n_{\mathrm{H}}\Omega) & & & & \\ & \ddots & & & \\ & & \Sigma^r_{L/R}(E) & & \\ & & & \ddots & \\ & & & & \Sigma^r_{L/R}(E + n_{\mathrm{H}}\Omega) \end{bmatrix}, \\
\boldsymbol{H} &= \begin{bmatrix} H_0 & H_1 & & & \\ H_{-1} & \ddots & H_1 & & \\ & H_{-1} & H_0 & \ddots & \\ & & \ddots & \ddots & H_1 \\ & & & H_{-1} & H_0 \end{bmatrix}, \\
\boldsymbol{G}^r(E) &= \begin{bmatrix} G^r_{-n_{\mathrm{H}},-n_{\mathrm{H}}}(E) & \cdots & \boxed{G^r_{-n_{\mathrm{H}},0}(E)} & \cdots & G^r_{-n_{\mathrm{H}},n_{\mathrm{H}}}(E) \\ \vdots & \ddots & \vdots & \cdots & \vdots \\ G^r_{0,-n_{\mathrm{H}}}(E) & \cdots & G^r_{0,0}(E) & \cdots & G^r_{0,n_{\mathrm{H}}}(E) \\ \vdots & \cdots & \vdots & \ddots & \vdots \\ G^r_{n_{\mathrm{H}},-n_{\mathrm{H}}}(E) & \cdots & G^r_{n_{\mathrm{H}},0}(E) & \cdots & G^r_{n_{\mathrm{H}},n_{\mathrm{H}}}(E) \end{bmatrix}.
\end{aligned}
\tag{A.3}
$$

where we boxed the center column of $\boldsymbol{G}^r$ to indicate the part of the Floquet-Green's function that needs to be extracted in conductance calculation, and stress that in

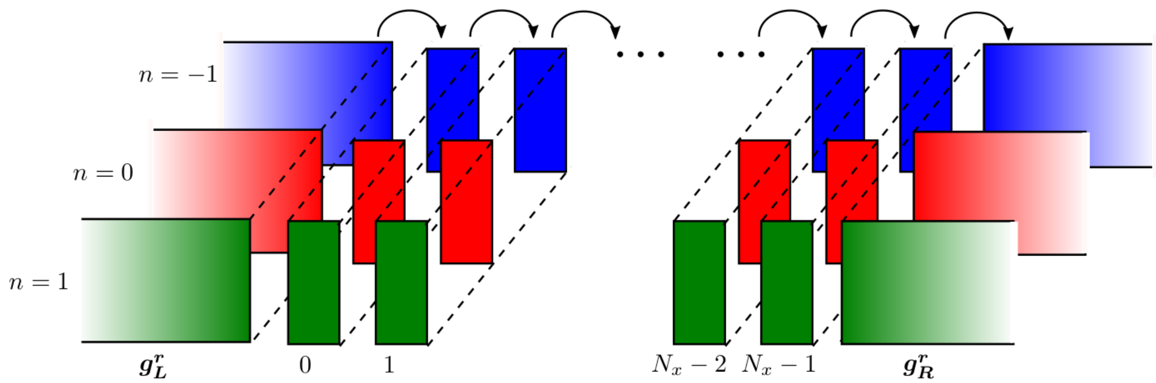

Figure A.1: Schematic of the recursive Floquet-Green's function method for DC transmission. $\boldsymbol{\mathcal{G}}^r_{x,x'}$ is the "slab-wise" Floquet-Green's function which is represented by dashed cuboids, enclosing rectangles corresponding to different harmonics n. Black arrows indicate the left-to-right sweep.

Equation A.3, each entry is itself a $N_xN_y \times N_xN_y$ matrix.

Thanks to the trace over space, the Floquet-Caroli formula for transmission Equation 2.7 requires only the "first-to-last" correlation, $\boldsymbol{G}^r_{0,N_x-1}$. Therefore we slice the lattice into slabs and consecutively couples them starting from the left. This procedure is equivalent to renormalizing the left self-energy by coupling the system to it, layer by layer, until the last system slab is arrived.

Below we denote by cursive letters the "slab-wise" Floquet-Green's function: $\boldsymbol{\mathcal{G}}^r_{x_1,x_2}$. They are indexed by a pair of x-coordinates (x_1, x_2), and, for each pair, they are matrices of size $N_yn_{\mathrm{F}} \times N_yn_{\mathrm{F}}$. The same goes for lowercase $\boldsymbol{g}^r_{xx}$, which are the slab-wise decoupled Floquet-Green's function at site x. Schematically, this process is demonstrated in Fig. A.1.

We need one more ingredient: the interslab coupling matrix $\boldsymbol{\mathcal{V}}$. It is defined by considering the Dyson equation when we couple two slabs [194]:

$$\begin{bmatrix} \boldsymbol{\mathcal{G}}_{x,x} & \boldsymbol{\mathcal{G}}_{x,x+1} \\ \boldsymbol{\mathcal{G}}_{x+1,x} & \boldsymbol{\mathcal{G}}_{x+1,x+1} \end{bmatrix} = \begin{bmatrix} \mathbf{g}_{x,x} & \mathbf{0} \\ \mathbf{0} & \mathbf{g}_{x+1,x+1} \end{bmatrix} + \begin{bmatrix} \mathbf{g}_{x,x} & \mathbf{0} \\ \mathbf{0} & \mathbf{g}_{x+1,x+1} \end{bmatrix} \begin{bmatrix} \mathbf{0} & \boldsymbol{\mathcal{V}} \\ \boldsymbol{\mathcal{V}}^\dagger & \mathbf{0} \end{bmatrix} \begin{bmatrix} \boldsymbol{\mathcal{G}}_{x,x} & \boldsymbol{\mathcal{G}}_{x,x+1} \\ \boldsymbol{\mathcal{G}}_{x+1,x} & \boldsymbol{\mathcal{G}}_{x+1,x+1} \end{bmatrix}. \tag{A.4}$$

It varies depending on the system (sublattice degree of freedom and how the lattice couples horizontally), as well as the drive protocol (whether x-hopping is driven). Let us specify to the case where x-hopping is undriven (if not, one most likely can gauge it away), and the slabs couple uniformly. In this case $\boldsymbol{\mathcal{V}}$ is simply proportional to a $N_y n_\mathrm{F} \times N_y n_\mathrm{F}$ identity matrix: $\boldsymbol{\mathcal{V}}_{(yy';mn)} = J_x \delta_{y,y'} \delta_{m,n}$. Finally, we remark that Eq.Equation A.4 is valid for contour Green's functions. Therefore one can derive from it the retarded (for time-averaged LDOS) and lesser component (for DC profile) of Green's functions using the Langreth rules [159].

Algorithm 1 Unidirectional sweep for DC transmission

$\boldsymbol{\mathcal{G}}^r_{xx} \leftarrow [(\mathbf{g}^r_{00})^{-1} - \boldsymbol{\mathcal{V}} \mathrm{g}^r_L \boldsymbol{\mathcal{V}}]^{-1}$ ▷ Initialization using left surface Green's function
$\boldsymbol{\mathcal{G}}^r_{0x} \leftarrow \boldsymbol{\mathcal{G}}^r_{xx}$
for $x \in [1, N_x - 2]$ **do**
  $\boldsymbol{\mathcal{G}}^r_{xx} \leftarrow [(\mathbf{g}^r_{xx})^{-1} - \boldsymbol{\mathcal{V}} \boldsymbol{\mathcal{G}}^r_{xx} \boldsymbol{\mathcal{V}}]^{-1}$
  $\boldsymbol{\mathcal{G}}^r_{0x} \leftarrow \boldsymbol{\mathcal{G}}^r_{0x} \boldsymbol{\mathcal{V}} \boldsymbol{\mathcal{G}}^r_{xx}$
end for
$\boldsymbol{\mathcal{G}}^r_{xx} \leftarrow [(\boldsymbol{g}^r_{N_x-1,N_x-1})^{-1} - \boldsymbol{\mathcal{V}} \boldsymbol{g}^r_R \boldsymbol{\mathcal{V}} - \boldsymbol{\mathcal{V}} \boldsymbol{\mathcal{G}}^r_{xx} \boldsymbol{\mathcal{V}}]$ ▷ Wraps the right boundary condition
$\boldsymbol{\mathcal{G}}^r_{0,x} \leftarrow \boldsymbol{\mathcal{G}}^r_{0,x} \boldsymbol{\mathcal{V}} \boldsymbol{\mathcal{G}}^r_{x,x}$

The pseudocode for the main loop of our calculation is given in Algorithm 1. It has the same structure as the static one [197]. The Floquet-Green's function thus obtained has its x-components resolved to $(0, N_x - 1)$. Next, we extract all relevant Floquet components, $\boldsymbol{\mathcal{G}}^r_{0,N_x-1}[k, 0]$, and calculate the transmission *at energy* E by multiplying the relevant Floquet components and performing a trace. This process is summarized in Algorithm 2. Here a square bracket $[m, n]$ means extracting (as a $N_y \times N_y$ matrix) the

m, n Floquet component, from a $N_y n_\mathrm{F} \times N_y n_\mathrm{F}$ Floquet matrix. Finally, Floquet sum rule is achieved by looping Algorithm 1 and then Algorithm 2 over n for $T(E + n\hbar\Omega)$ and summing them.

Algorithm 2 Extracting Floquet components to compute DC transmission at energy E

$T(E) \leftarrow 0$
$\gamma^L \leftarrow \mathrm{i}(\boldsymbol{\Sigma}_L^r - (\boldsymbol{\Sigma}_L^r)^\dagger)[0, 0]$
for $k \in [-n_\mathrm{H}, n_\mathrm{H}]$ **do**
  $g \leftarrow (\boldsymbol{\mathcal{G}}^r_{0,N_x-1})[k, 0]$
  $\gamma^R \leftarrow \mathrm{i}(\boldsymbol{\Sigma}_R^r - (\boldsymbol{\Sigma}_R^r)^\dagger)[k, k]$
  $T(E) \leftarrow T(E) + \mathrm{Tr}_\Lambda(g\gamma^L g^\dagger \gamma^R)$
end for

Algorithm 3 Bidirectional sweep for DC profile (and time-averaged LDOS)

for $x \in [0, N_x - 1]$ **do**
  $\boldsymbol{\mathcal{G}}^r_L \leftarrow \mathbf{g}^r_L$ ▷ Initialize left retarded Green's function
  $\boldsymbol{\mathcal{G}}^<_L \leftarrow -(\boldsymbol{\mathcal{G}}^r_L - (\boldsymbol{\mathcal{G}}^r_L)^\dagger) f^L$ ▷ Initialize left lesser Green's function
  for $x_L \in [0, x)$ **do** ▷ Left sweep towards x
    $\boldsymbol{\mathcal{G}}^r_L \leftarrow [(\mathbf{g}^r_{x_L x_L})^{-1} - \boldsymbol{\mathcal{V}}\boldsymbol{\mathcal{G}}^r_L\boldsymbol{\mathcal{V}}]^{-1}$ ▷ Renormalize the left retarded Green's function
    $\boldsymbol{\mathcal{G}}^<_L \leftarrow \boldsymbol{\mathcal{G}}^r_L\boldsymbol{\mathcal{V}}\boldsymbol{\mathcal{G}}^<_L\boldsymbol{\mathcal{V}}(\boldsymbol{\mathcal{G}}^r_L)^\dagger$ ▷ Renormalize the left lesser Green's function
  end for
  $\boldsymbol{\mathcal{G}}^r_R \leftarrow \mathbf{g}^r_R$ ▷ Initialize right retarded Green's function
  $\boldsymbol{\mathcal{G}}^<_R \leftarrow -(\boldsymbol{\mathcal{G}}^r_R - (\boldsymbol{\mathcal{G}}^r_R)^\dagger) f^R$ ▷ Initialize right lesser Green's function
  for $x_R \in (x, N_x - 1]$ **do** ▷ Right sweep towards x
    $\boldsymbol{\mathcal{G}}^r_R \leftarrow [(\mathbf{g}^r_{x_R x_R})^{-1} - \boldsymbol{\mathcal{V}}\boldsymbol{\mathcal{G}}^r_R\boldsymbol{\mathcal{V}}]^{-1}$ ▷ Renormalize the right retarded Green's function
    $\boldsymbol{\mathcal{G}}^<_R \leftarrow \boldsymbol{\mathcal{G}}^r_R\boldsymbol{\mathcal{V}}\boldsymbol{\mathcal{G}}^<_R\boldsymbol{\mathcal{V}}(\boldsymbol{\mathcal{G}}^r_R)^\dagger$ ▷ Renormalize the right lesser Green's function
  end for
  $\boldsymbol{\mathcal{G}}^r_{xx} \leftarrow [(\mathbf{g}^r_{xx})^{-1} - \boldsymbol{\mathcal{V}}(\boldsymbol{\mathcal{G}}^r_L + \boldsymbol{\mathcal{G}}^r_R)\boldsymbol{\mathcal{V}}]^{-1}$ ▷ Solve the retarded Green's function for slab x.
  $\text{T-LDOS}_{(x,y)}(E) \leftarrow -\frac{1}{\pi}\text{Im}(\boldsymbol{\mathcal{G}}^r_{xx})_{yy}[0,0]$ ▷ Diagonal component yy of the $0,0$ Floquet block at slab x
  $\boldsymbol{\mathcal{G}}^<_{xx} \leftarrow \boldsymbol{\mathcal{G}}^r_{xx}\boldsymbol{\mathcal{V}}(\boldsymbol{\mathcal{G}}^<_L + \boldsymbol{\mathcal{G}}^<_R)\boldsymbol{\mathcal{V}}(\boldsymbol{\mathcal{G}}^r_{xx})^\dagger$ ▷ Calculate the lesser Green's function for slab x.
  $I^\uparrow_{x,y} \leftarrow 2\text{Re}\sum_{m=-n_\text{F}}^{n_\text{F}} \left\{\hat{J}_{y-1,y}(m)(\boldsymbol{\mathcal{G}}^<_{xx})_{y,y-1}[0,m] + \hat{J}_{y,y+1}(m)(\boldsymbol{\mathcal{G}}^<_{xx})_{y+1,y}[0,m]\right\}$
  $\boldsymbol{\mathcal{G}}^<_{x+1,x} \leftarrow \boldsymbol{\mathcal{G}}^r_R\boldsymbol{\mathcal{V}}\boldsymbol{\mathcal{G}}^<_{xx} + \boldsymbol{\mathcal{G}}^<_R\boldsymbol{\mathcal{V}}(\boldsymbol{\mathcal{G}}^r_{xx})^\dagger$ ▷ Calculate the interslab $(x+1,x)$ lesser Green's function
  $I_{x+1\leftarrow x,y} = 2\text{Re}\sum_{m=-n_\text{F}}^{n_\text{F}} \left\{\hat{J}_{x,x+1}(m)(\boldsymbol{\mathcal{G}}^<_{x+1,x})_{yy}[m,0]\right\}$
  $\boldsymbol{\mathcal{G}}^<_{x-1,x} \leftarrow \boldsymbol{\mathcal{G}}^r_L\boldsymbol{\mathcal{V}}\boldsymbol{\mathcal{G}}^<_{xx} + \boldsymbol{\mathcal{G}}^<_L\boldsymbol{\mathcal{V}}(\boldsymbol{\mathcal{G}}^r_{xx})^\dagger$ ▷ Calculate the interslab $(x-1,x)$ lesser Green's function
  $I_{x-1\leftarrow x,y} \leftarrow 2\text{Re}\sum_{m=-n_\text{F}}^{n_\text{F}} \left\{\hat{J}_{x,x-1}(m)(\boldsymbol{\mathcal{G}}^<_{x,x-1})_{yy}[0,m]\right\}$
end for

A.2 DC profile

For quantities that involve spatial distributions, "local" Green's functions of the like $\boldsymbol{G}^{r/<}_{x_i,x_i}$ are needed instead, and this applies to all system slabs $x_i \in [0, N_x - 1]$. Thus the recursive method consists of N_x sweeps, each sweep being bidirectional, as shown

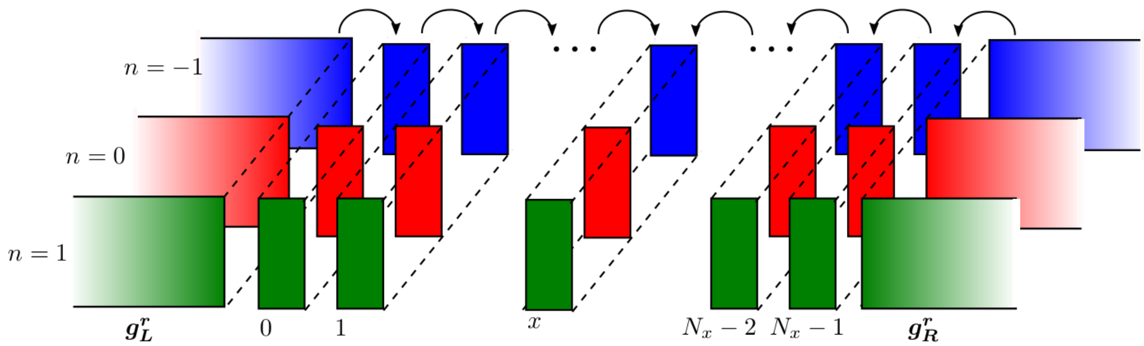

Figure A.2: Schematic of the recursive Floquet-Green's function method for local quantities (DC profile, LDOS). For each x, one performs a bidirectional sweep (black arrows), which amounts to considering slab x as the system, with all slabs to the left (including the left lead) acting as left self energy, and the same for right. Dashed lines enclose photon-dressed Green's function at different harmonics n.

in Fig. A.2.

The strategy is similar as before: promote the Green's function to Floquet space, perform recursive calculations as in the static case [197], then extract the relevant Floquet components. We first rewrite the local current at site $i=(x_i,y_i)$ given by Eq. Equation 2.11 as:

$$\begin{aligned}\vec{I}_i &= \hat{\mathbf{x}} I_i^{\rightarrow} + \hat{\mathbf{y}} I_i^{\uparrow} \\ &= \hat{\mathbf{x}}\left(I_{i+\hat{\mathbf{x}}\leftarrow i} - I_{i-\hat{\mathbf{x}}\leftarrow i}\right) + \hat{\mathbf{y}} I_i^{\uparrow} \\ &= 2\mathrm{Re}\sum_{m\in\mathbb{Z}}\Big\{\hat{\mathbf{x}}\Big[\tilde{J}_{i,i+\hat{\mathbf{x}}}(m)\boldsymbol{G}^{<}_{(i+\hat{\mathbf{x}},i;m,0)} - \tilde{J}_{i,i-\hat{\mathbf{x}}}(m)\boldsymbol{G}^{<}_{(i-\hat{\mathbf{x}},i;0,m)}\Big] \\ &+ \hat{\mathbf{y}}\Big[\tilde{J}_{i-\hat{\mathbf{y}},i}(m)\boldsymbol{G}^{<}_{(i,i-\hat{\mathbf{y}};0,m)} + \tilde{J}_{i,i+\hat{\mathbf{y}}}(m)\boldsymbol{G}^{<}_{(i+\hat{\mathbf{y}},i;0,m)}\Big]\Big\}.\end{aligned} \tag{A.5}$$

Thus, for the horizontal current, we need the interslab lesser Floquet-Green's function $\boldsymbol{\mathcal{G}}^{<}_{x+1,x}$, and for the vertical current, we need the local lesser function $\boldsymbol{\mathcal{G}}^{<}_{xx}$. From the Dyson equation Equation A.4, we apply the Langreth rule [159] for lesser projection to find:

$$\begin{aligned}\boldsymbol{\mathcal{G}}^{<}_{x+1,x} &= \mathbf{g}^{r}_{x+1,x+1}\boldsymbol{\mathcal{V}}\boldsymbol{\mathcal{G}}^{<}_{xx} + \mathbf{g}^{<}_{x+1,x+1}\boldsymbol{\mathcal{V}}\boldsymbol{\mathcal{G}}^{a}_{xx},\\ \boldsymbol{\mathcal{G}}^{<}_{x-1,x} &= \mathbf{g}^{r}_{x-1,x-1}\boldsymbol{\mathcal{V}}\boldsymbol{\mathcal{G}}^{<}_{xx} + \mathbf{g}^{<}_{x-1,x-1}\boldsymbol{\mathcal{V}}\boldsymbol{\mathcal{G}}^{a}_{xx}.\end{aligned} \tag{A.6}$$

The task then is to calculate, for each slab x, the lesser and advanced Green's function $\boldsymbol{\mathcal{G}}^{<}_{xx}, \boldsymbol{\mathcal{G}}^{a}_{xx}$. The latter is given by the Dyson equation, from which one can calculate the former using the Keldysh equation. This is implemented by Algorithm 3. The core of the algorithm is very similar to that described in Ref. [197] (despite all the Green's functions being promoted to the Floquet version). A difference arises when we calculate the time-averaged LDOS (line 15), the vertical current (line 17) and the horizontal currents (lines 19 and 21) in Algorithm 3.

A.3 Time-averaged LDOS

The calculation of the time-averaged retarded Floquet-Green's function is needed in the calculation of DC profile, hence we shall not repeat it here. If the DC profile is not needed, one simply removes all lesser-related steps in Algorithm 3. We end this section by writing explicitly again what we mean by the time-averaged LDOS:

$$\text{T-LDOS}_{(x,y)}(E) = -\frac{1}{\pi}\text{Im}\left[-\frac{\mathrm{i}}{\hbar}\theta(t-t')\langle c_{x,y}(t)c^{\dagger}_{x,y}(t')\rangle\right]_{00}(E), \tag{A.7}$$

where $[\cdots]_{00}(E)$ means the Floquet representation Eq. Equation 2.2.

Appendix B

Expressions of the local direct current of the harmonically driven Hofstadter model

The expressions of the time-averaged local current, given in Equation 2.11 and Equation A.5, are rather general. As a concrete example, here we give the corresponding expressions in the harmonically-driven Hofstadter model.

B.1 Time-averaged longitudinal current

The x-hopping is undriven in our model, so we have the longitudinal DC (longitudinal with respect to the applied bias):

$$I_i^{\rightarrow} = 2J_x \mathrm{Re}\Big[\boldsymbol{G}^<_{(i,i-\hat{\mathbf{x}};0,0)} + \boldsymbol{G}^<_{(i+\hat{\mathbf{x}},i;0,0)}\Big]. \tag{B.1}$$

B.2 Time-averaged transverse current

With the y-hopping driven and modulated over x-direction, the transverse current (transverse with respect to the applied bias) needs a bit more work. Given the y-hopping term as $J_y\left[s+\cos(\Omega t)\right]\mathrm{e}^{\mathrm{i}2\pi\alpha x_i}c_i^\dagger c_{i+\hat{\mathbf{y}}}+\mathrm{h.c.}$, we have the transverse direct current:

$$\begin{aligned}
I_i^\uparrow = J_y\Bigg\{ & s\times 2\mathrm{Re}\Big[\mathrm{e}^{\mathrm{i}2\pi\alpha x_i}\Big(\boldsymbol{G}^<_{(i+\hat{\mathbf{y}},i;0,0)}+\boldsymbol{G}^<_{(i,i-\hat{\mathbf{y}};0,0)}\Big)\Big] \\
& +\frac{1}{2}\Bigg(\mathrm{e}^{\mathrm{i}2\pi\alpha x_i}\Big[\boldsymbol{G}^<_{(i+\hat{\mathbf{y}},i;1,0)}+\boldsymbol{G}^<_{(i+\hat{\mathbf{y}},i;-1,0)}+\boldsymbol{G}^<_{(i,i-\hat{\mathbf{y}};1,0)}+\boldsymbol{G}^<_{(i,i-\hat{\mathbf{y}};-1,0)}\Big] \\
& -\mathrm{e}^{-\mathrm{i}2\pi\alpha x_i}\Big[\boldsymbol{G}^<_{(i,i+\hat{\mathbf{y}};1,0)}+\boldsymbol{G}^<_{(i,i+\hat{\mathbf{y}};-1,0)}+\boldsymbol{G}^<_{(i-\hat{\mathbf{y}},i;1,0)}+\boldsymbol{G}^<_{(i-\hat{\mathbf{y}},i;-1,0)}\Big]\Bigg)\Bigg\}.
\end{aligned} \tag{B.2}$$

Appendix C

Transport properties of co-propagating and gapped Floquet edge states

We consider the parameters $J_y = 1.6, \alpha = 1/3, \Omega = \pi$, and $s = 0$. The corresponding phase has two pairs of co-propagating edge states in the first gap and gapped edge states in the second gap, as shown in the Floquet spectrum (Figure C.1a).

C.1 DC conductance

We first present the transmission calculation for three cases: (1) perfect, (2) disordered and (3) defective lattices. As shown in Figure C.1b, be it disorder or defect, the co-propagating (gapless) Floquet edge modes are very robust, whereas the gapped edge states have no quantized conductance even in the perfect, pristine case.

C.2 Time-averaged LDOS

We probe the time-averaged local density of states at quasienergy $\epsilon = 1.4$ which lies in the second Floquet gap and thus corresponds to gapped edge states. Consistent with the Floquet spectrum (Figure C.1a), at $\epsilon = 1.4$, the states are localized on edges, albeit

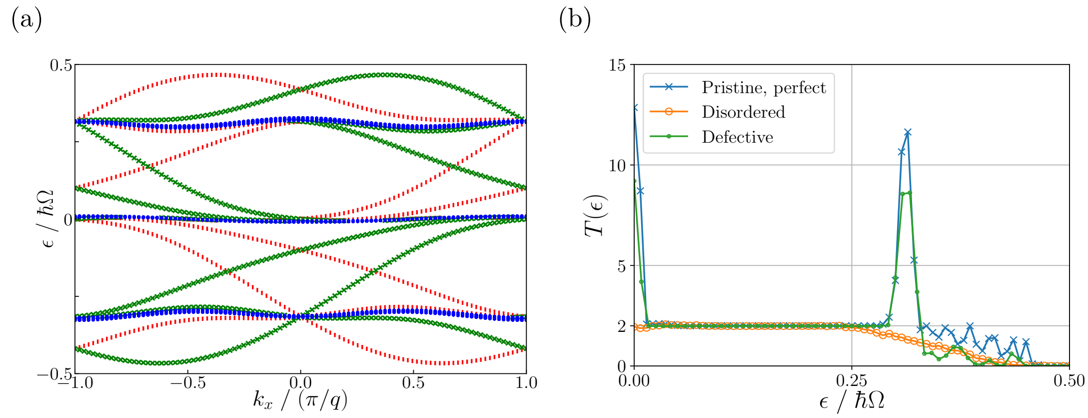

Figure C.1: (a): Floquet spectrum of the HDHM with parameters $J_y = 1.6, \alpha = 1/3, \Omega = \pi$, and $s = 0$. showing the existence of gapped edge states on the top and bottom gaps ($q = 3$). (b): DC transmission after the Floquet sum rule. For the disordered curve (cirlces), the disorder strength is $W = 1$, penetrating the whole lattice, averaged over 100 realizations. For the defective curve (dots), the defects are introduced identically to the one in Figure C.3d. System sizes are $N_x = N_y = 40,\ n_{\mathrm{F}} = 7$.

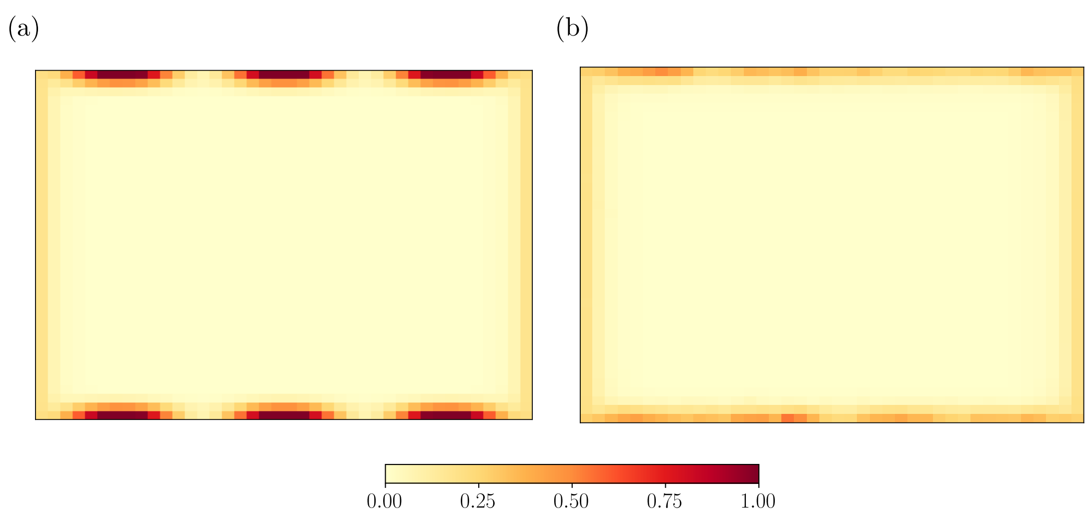

Figure C.2: Time-averaged LDOS at quasienergy $\epsilon = 1.4$ corresponding to a gapped edge state. (a): Pristine. (b): Edge disorder of strength $W = 0.5$ penetrate three layers on all four edges. System sizes are $N_x = N_y = 40,\ n_{\mathrm{F}} = 7$. Result shown is averaged over 200 disorder realizations.

not as uniformly as their gapless counterparts in Figure 2.4. Also, the presence of edge disorder destroys this “edge islands” pattern (Figure C.2b).

C.3 Local DC profile

Here we consider the local current pattern of the gapped and co-propagating edge states, as well as their responses to defects. Unlike their gapless counter-propagating analogs in Figure 2.8, the edge current profile is not as evident for gapped edge states (Figure C.3a). Upon introduction of defects, the already-weak current gets diminished further. Finally, the chiral feature of the co-propagating (gapped) edge states is evident from Figure C.3c, with their topological protection from backscattering exemplified in Figure C.3d.

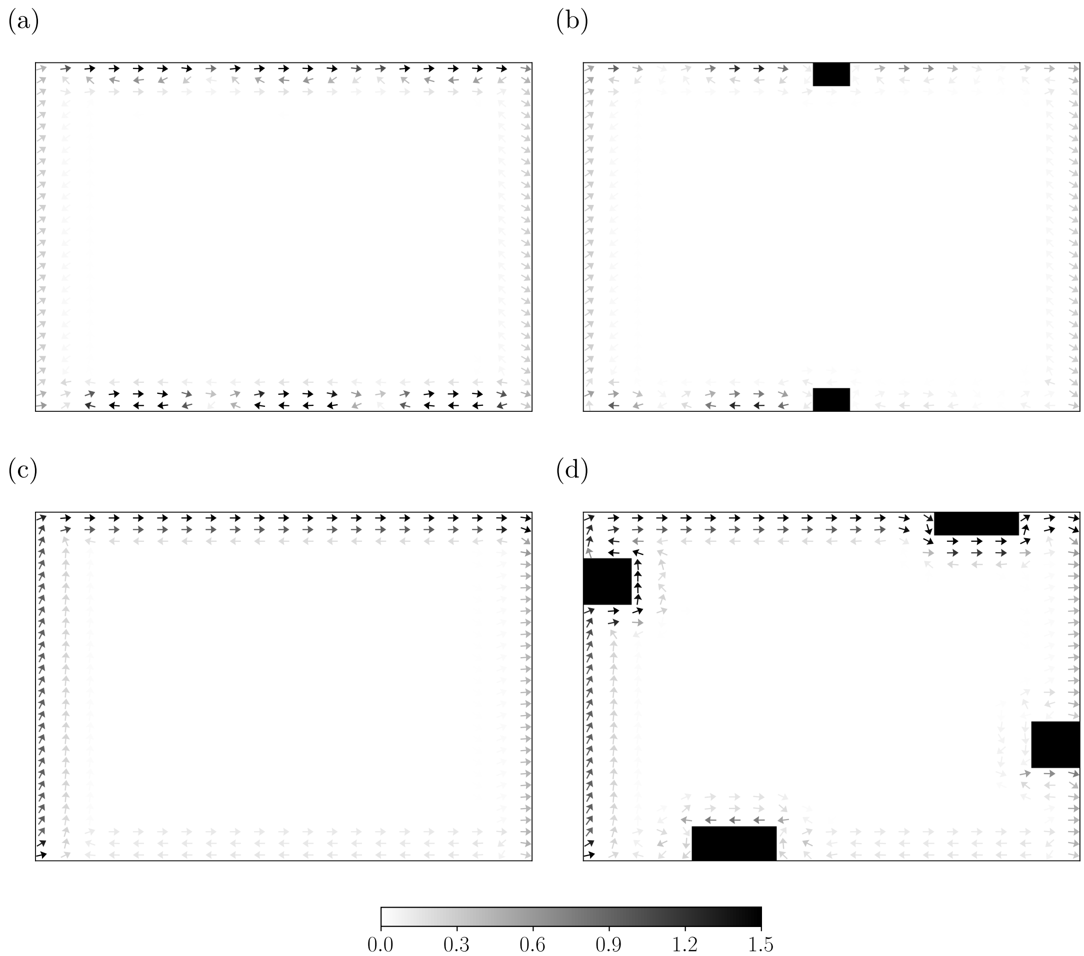

Figure C.3: DC profile of gapped and co-propagating edge states. Top panels: gapped edge states, with $E = 1.4, \mu_L = 1.41$, and $\mu_R = 1.39$. Bottom panels: co-propagating edge states, with $E = 0.5, \mu_L = 0.51$, and $\mu_R = 0.49$. Panels (a), (c): perfect lattice. Panels (b), (d): defective lattices. The Floquet sum rule is applied in all cases. Some arrows are skipped for better display. System sizes: $N_x = 41,\ N_y = 30,\ n_{\mathrm{F}} = 7$.

Appendix D

Existence and dispersion of surface states

D.1 Existence of surface states

Given the effective Hamiltonian

$$\begin{aligned} H_{\mathrm{eff},\pm}(\boldsymbol{k}) &= \left(\sum_{i=x,y,z} \cos k_i - m\right)\tau_1 + \sin k_z \tau_3 + \left(M_0(\boldsymbol{k}_\parallel) \pm \sqrt{\sum_i M_i^2(\boldsymbol{k}_\parallel)}\right)\tau_2 \\ &\stackrel{\text{def}}{=} \boldsymbol{h}_\pm(\boldsymbol{k}) \cdot \boldsymbol{\tau}, \end{aligned} \tag{D.1}$$

to study the existence of edge states localized along z, we consider the real-space version of (D.1) in a semi-infinite geometry, terminated at the x–y plane at $z = 0$. Hence translational symmetry is broken in the z direction, and surface states localized along the z direction may emerge. We assume that translational symmetry is preserved along x and y, so that the corresponding momenta k_x and k_y are good quantum numbers. In this way, one can decouple a higher dimensional system into a family of 1D problems parameterized by k_x and k_y.

The three Pauli matrices constitute a Clifford algebra and span a 3-dimensional vector space, whereas $\boldsymbol{h}_\pm$ denote some vectors in this space. For a 1D problem with fixed k_x and k_y, $\boldsymbol{h}_\pm$ is a function of k_z, and traces out a closed trajectory in the 3D vector space as k_z varies from 0 to 2π. It was shown (Ref. [218], Section II and III) that the existence of surface states and their eigenenergies are determined by the position of the trajectory. Specifically, one can find a plane that contains the trajectory, and project the origin onto this plane. Whether the trajectory encloses the projected point determines the existence of surface states, and the distance between the origin and the plane gives the absolute value of the corresponding eigenenergies.

In our model, the trajectory is in the 1–3 plane as k_z only appears in the coefficients of τ_1 and τ_3. Hence, we can write the Hamiltonian as $\boldsymbol{h}_\pm = \boldsymbol{h}^0_\pm + \boldsymbol{h}_{\pm,\parallel} + \boldsymbol{h}_{\pm,\perp}$, where

$$\begin{aligned}
\boldsymbol{h}^0_\pm &= (\cos k_z, 0, \sin k_z), \\
\boldsymbol{h}_{\pm,\parallel} &= (\cos k_x + \cos k_y - m, 0, 0), \\
\boldsymbol{h}_{\pm,\perp} &= \left(0, \left(M_0(\boldsymbol{k}_\parallel) \pm \sqrt{\sum_i M_i^2(\boldsymbol{k}_\parallel)}\right), 0\right).
\end{aligned} \tag{D.2}$$

Here $\boldsymbol{h}^0_\pm$ describes the trajectory which is a circle, while $\boldsymbol{h}_{\pm,\parallel}$ and $\boldsymbol{h}_{\pm,\perp}$ are k_z-independent, which lies in and is normal to the 1–3 plane respectively. The circular trajectory now has a radius of 1, i.e. the projection of the origin on the 1–3 plane is within the trajectory as long as

$$|\boldsymbol{h}_{\pm,\parallel}| = |\cos k_x + \cos k_y - m| < 1, \tag{D.3}$$

which is the condition for the existence of surface states. Provided that Eq.(3.5) holds, the energies of the surface states are given by

$$\epsilon_{u,\pm} = u|\boldsymbol{h}^0_{\pm,\perp}| = u\left|M_0(\boldsymbol{k}_\parallel) \pm \sqrt{\sum_i M_i^2(\boldsymbol{k}_\parallel)}\right|, \tag{D.4}$$

with $u = \pm 1$ indicating the upper and lower branches of the edge states.

Since we consider gap terms that do not depend on k_z and anticommute with the original nodal loop Hamiltonian H_0, we see that the existence of surface states is only associated with H_0, and the gap terms will modify the energies of these surface states.

D.2 Dispersion of surface states

For convenience, we rotate the pseudospin with an angle of $\pi/2$ in the 2–3 plane, thus $\tau_2 \to \tau_3$ and $\tau_3 \to -\tau_2$, and rewrite the effective Hamiltonian as

$$H_{\text{eff},\pm}(k_z) = (\Delta_1 + \cos k_z)\tau_1 - \sin k_z \tau_2 + \Delta_2^{\pm}\tau_3, \tag{D.5}$$

with $\Delta_1 = \cos k_x + \cos k_y - m$ and $\Delta_2^{\pm} = \left(M_0(\boldsymbol{k}_\parallel) \pm \sqrt{\sum_i M_i^2(\boldsymbol{k}_\parallel)}\right)$. In real space, the Hamiltonian reads

$$\begin{aligned} H_{\text{eff},\pm} &= \sum_z \Delta_1 \hat{a}_z^\dagger \hat{b}_z + \hat{a}_z^\dagger \hat{b}_{z+1} + h.c. \\ &\quad + \sum_z \Delta_2^{\pm}(\hat{a}_z^\dagger \hat{a}_z - \hat{b}_z^\dagger \hat{b}_z). \end{aligned} \tag{D.6}$$

We consider a semi-infinite system with $z = 1, 2, 3, ...$, and choose the wavefunction as $\Psi_{n,\pm} = \sum_z (\psi_{a,z}\hat{a}_z^\dagger + \psi_{b,z}\hat{b}_z^\dagger)|0\rangle$, with $|0\rangle$ the vacuum state. The eigenvalue equation $H_{\text{eff},\pm}\Psi_{n,\pm} = E_{n,\pm}\Psi_{n,\pm}$ gives:

$$\Delta_1\psi_{b,z} + \psi_{b,z+1} + \Delta_2^{\pm}\psi_{a,z} = E_n\psi_{a,z}, \tag{D.7}$$

$$\Delta_1\psi_{a,z} + \psi_{a,z-1} - \Delta_2^{\pm}\psi_{b,z} = E_n\psi_{b,z}. \tag{D.8}$$

Since z starts from 1, one has $\psi_{a,0} = 0$ for the boundary condition, and $\psi_{b,0}$ is irrelevant here because it does not appear in Equations. (D.7) and (D.8).

A solution localized near $z = 1$ can be achieved by choosing $E_n = -\Delta_2^{\pm}$. In this case, Eq. (D.8) becomes

$$\Delta_1\psi_{a,z} + \psi_{a,z-1} = 0, \tag{D.9}$$

and we have $\psi_{a,z} = 0$ for any z due to the boundary condition. Thus Equation D.7 can also be simplified as

$$\Delta_1\psi_{b,z} + \psi_{b,z+1} = 0, \tag{D.10}$$

which yields an exponentially decreasing state only if $|\Delta_1| < 1$, whence Equation 3.5 as a criterion for the existence of edge states. Notice that here we choose a semi-infinite geometry with only one edge. When the system has a finite size with two ends, edge states with non-zero a component localized at the other end can exist when $E_n = \Delta_2^{\pm}$.

Next, consider the case with a general eigenenergy $E_n \neq \pm\Delta_2^{\pm}$. Substituting Eq. (D.7) to (D.8), we have

$$\frac{\Delta_1^2 + 1}{\Delta_1}\psi_{b,z} + \psi_{b,z+1} + \psi_{b,z-1} = \frac{E_n^2 - (\Delta_2^{\pm})^2}{\Delta_1}\psi_{b,z}. \tag{D.11}$$

In the form of transfer matrix, we have

$$\begin{pmatrix} \psi_{b,z+1} \\ \psi_{b,z} \end{pmatrix} = A \begin{pmatrix} \psi_{b,z} \\ \psi_{b,z-1} \end{pmatrix}, \quad A = \begin{pmatrix} \frac{E_n^2 - (\Delta_2^{\pm})^2 - \Delta_1^2 - 1}{\Delta_1} & -1 \\ 1 & 0 \end{pmatrix}. \tag{D.12}$$

We now apply the method in Ref. [267] to determine whether the eigenstate corresponding to E_n is an edge state or not. Assuming

$$A \begin{pmatrix} a \\ b \end{pmatrix} = \epsilon_A \begin{pmatrix} a \\ b \end{pmatrix}, \tag{D.13}$$

the vector $(\psi_{b,z+1}, \psi_{b,z})^T$ can be written as a linear superposition of the two orthogonal eigenvectors of A, i.e., $(\psi_{b,z+1}, \psi_{b,z})^T = s_1(a_1, b_1)^T + s_2(a_2, b_2)^T$, with s_1 and s_2 the superposition coefficients. Thus we have

$$\begin{pmatrix} \psi_{b,z+n+1} \\ \psi_{b,z+n} \end{pmatrix} = A^n \begin{pmatrix} \psi_{b,z+1} \\ \psi_{b,z} \end{pmatrix} = s_1\epsilon_{A,1}^n \begin{pmatrix} a_1 \\ b_1 \end{pmatrix} + s_2\epsilon_{A,2}^n \begin{pmatrix} a_2 \\ b_2 \end{pmatrix}, \tag{D.14}$$

which suggests that $\psi_z = 0$ as $z \to \infty$ if both eigenvalues of A are less than unity. On the other hand, if both eigenvalues are greater than unity, it corresponds to an edge state localized at $z \to \infty$.

In our case, the eigenvalues of the transfer matrix A in Eq. (D.13) satisfy

$$\epsilon_{A,1}\epsilon_{A,2} = \det(A) = 1. \tag{D.15}$$

Therefore, the two eigenvalues cannot be both greater or less than unity simultaneously. In other words, the wavefunction of $E_n \neq \pm\Delta_2^{\pm}$ cannot localize anywhere along the 1D chain.

In conclusion, the existence of edge states (or surface states as in the main text) requires

$$|\Delta_1| = |\cos k_x + \sin k_y - m| < 1, \tag{D.16}$$

and their energies are given by

$$E = \pm\Delta_2^{\pm} = \pm\left(M_0(\boldsymbol{k}_\parallel) \pm \sqrt{\sum_i M_i^2(\boldsymbol{k}_\parallel)}\right). \tag{D.17}$$

Appendix E

Transport in superconducting systems

To compute electrical current in Bardeen-Cooper-Schrieffer (BCS) superconducting systems using Nambu-Keldysh-Green's functions, we follow Ref.[239] which studied the zero-bias conductance peak due to Majorana zero modes in semiconductor nanowire [93]. Below we highlight the key steps towards the final expression.

As before, consider a superconductor connected to two metallic leads. The starting point is to work in an extended Nambu spinor representation. Then the superconductor Hamiltonian reads $\mathcal{H} = \frac{1}{2}\sum_{i,j} \Psi_i^\dagger H_{ij} \Psi_j$, with the Nambu spinor $\Psi_j = (c_j, c_j^\dagger)^{\mathrm{T}}$, where j indicates the degrees of freedom of the sample, e.g. lattice site and spin. As constrained by fermionic anticommutation relation, the first quantized Hamiltonian H assumes the form

$$H = \begin{pmatrix} h & \Delta \\ -\Delta^* & -h \end{pmatrix}. \tag{E.1}$$

Here, h contains non-superconducting terms such as kinetic energy and spin-orbit coupling, whereas Δ is the pairing term that may be obtained non-self-consistently since the superconductivity is proximitized. The metallic contacts are incorporated via the self energies[1], hereby denoted as $\Xi_{\mathrm{L,R}}$. To calculate current, we define the electron and hole projections of the self energies, given respectively by

$$\begin{aligned}\Sigma &= \frac{1+\tau_z}{2}\Xi\frac{1+\tau_z}{2},\\ \overline{\Sigma} &= \frac{1-\tau_z}{2}\Xi\frac{1-\tau_z}{2},\end{aligned} \tag{E.2}$$

where τ is the Pauli matrix acting on Nambu spinor space. Then, it can be shown that the current reads:

$$I_{\mathrm{L}} = \frac{e}{2h}\int_{-\infty}^{\infty} \mathrm{d}E\ \mathrm{Tr}\Big[(\Sigma_{\mathrm{L}}^{>}G^{<} - \Sigma_{\mathrm{L}}^{<}G^{>}) - (\overline{\Sigma}_{\mathrm{L}}^{>}G^{<} - \overline{\Sigma}_{\mathrm{L}}^{<}G^{>})\Big]. \tag{E.3}$$

Above, the lesser and greater Green's functions satisfy the Keldysh equations $G^{</>} = G(\Sigma_{\mathrm{L}}^{</>}+\Sigma_{\mathrm{R}}^{</>})G^{\dagger}$, where the retarded Green's function satisfies $(E-\mathcal{H}-\Xi_{\mathrm{L}}-\Xi_{\mathrm{R}})G = 1$. To proceed, one invokes the fluctuation-dissipation relations for the left and right leads. For the electron projection, one has $\Sigma^{>}(E) = -\mathrm{i}\Gamma(E)[1-f(E)]$ and $\Sigma^{<}(E) = \mathrm{i}\Gamma(E)f(E)$. For the hole projection, one has $\overline{\Sigma}^{>}(E) = -\mathrm{i}\overline{\Gamma}(E)[1-\bar{f}(-E)]$ and $\overline{\Sigma}^{<}(E) = \mathrm{i}\overline{\Gamma}(E)\bar{f}(-E)$, where f is the Fermi function, $\bar{f} = 1-f$ is the "complement" of the Fermi function, and the line-width function is $\Gamma = \mathrm{i}(\Sigma - \Sigma^{\dagger})$ (similarly for the hole projection). These results are valid for both the left and right leads. One may then proceed to expand Equation E.3:

$$\begin{aligned} I_{\mathrm{L}} = \frac{e}{2h}\int_{-\infty}^{\infty}\mathrm{d}E\ \Big\{&\mathrm{Tr}\Big[G\Gamma_R G^{\dagger}\Gamma_L\Big](f_E^R - f_E^L)\\ &+ \mathrm{Tr}\Big[G\overline{\Gamma}_L G^{\dagger}\Gamma_L\Big](\bar{f}_{-E}^L - f_E^L) + \mathrm{Tr}\Big[G\overline{\Gamma}_R G^{\dagger}\Gamma_L\Big](\bar{f}_{-E}^R - f_E^L)\\ &- \mathrm{Tr}\Big[G\overline{\Gamma}_R G^{\dagger}\overline{\Gamma}_L\Big](\bar{f}_{-E}^R - \bar{f}_{-E}^L) - \mathrm{Tr}\Big[G\Gamma_L G^{\dagger}\overline{\Gamma}_L\Big](f_E^L - \bar{f}_{-E}^L)\\ &- \mathrm{Tr}\Big[G\Gamma_R G^{\dagger}\overline{\Gamma}_L\Big](f_E^R - \bar{f}_{-E}^L)\Big\}, \end{aligned} \tag{E.4}$$

[1] The self energies are frequently approximated as a constant under the wideband approximation. The exact value does not affect the quantized plateaus as long as it does not differ too much from the energy scale of the sample. This is the approach we take throughout this work to model metallic leads.

where for a more compact presentation we wrote, e.g. $\bar{f}^R(-E)$ to refer to the $\bar{f}$ function of the right lead evaluated at $-E$. With an additional relation $\mathrm{Tr}\Big[G\Gamma^{\mu}G^{\dagger}\Gamma^{\nu}\Big](E) = \mathrm{Tr}\Big[G\Gamma^{\bar{\mu}}G^{\dagger}\Gamma^{\bar{\nu}}\Big](-E)$, where μ,ν refer to electron or hole projection, and $\bar{\mu},\bar{\nu}$ their complements, one can simplify Equation E.4:

$$\begin{aligned} I_{\mathrm{L}} = \frac{e}{2h}\int_{-\infty}^{\infty} \mathrm{d}E\ & 2\mathrm{Tr}\Big[G\Gamma_R G^{\dagger}\Gamma_L\Big](f_E^R - f_E^L) \\ &+ \mathrm{Tr}\Big[G\overline{\Gamma}_L G^{\dagger}\Gamma_L\Big](\bar{f}_{-E}^L - f_E^L - f_{-E}^L + \bar{f}_E^L) \\ &+ \mathrm{Tr}\Big[G^r\overline{\Gamma}_R G^a\Gamma_L\Big](\bar{f}_{-E}^R - f_E^L - f_{-E}^R + \bar{f}_E^L). \end{aligned} \tag{E.5}$$

The coefficients $\mathrm{Tr}[\cdots]$ in the first, second, and third line can be interpreted respectively as normal transmission (electron transmitted as electron), local Andreev reflection (electron backscattered as hole), crossed Andreev reflection (electron transmitted as hole). We now make the crucial configuration of a symmetric bias of the left and right lead:$V_{\mathrm{L}} = -V_{\mathrm{R}} = V/2$. Then Equation E.5 simplifies further:

$$I_{\mathrm{L}} = \frac{e}{h}\int_{-\infty}^{\infty} \mathrm{d}E\Big[g(E) + g^{\mathrm{LAR}}(E)\Big]\Big[f_{\mathrm{R}}(E) - f_{\mathrm{L}}(E)\Big], \tag{E.6}$$

where we defined the normal transmission and local Andreev reflection coefficients:

$$\begin{aligned} g(E) &= \mathrm{Tr}\left[G(E)\Gamma_{\mathrm{R}}(E)G^{\dagger}(E)\Gamma_{\mathrm{L}}(E)\right], \\ g^{\mathrm{LAR}}(E) &= \mathrm{Tr}\left[G(E)\overline{\Gamma}_{\mathrm{L}}(E)G^{\dagger}(E)\Gamma_{\mathrm{L}}(E)\right]. \end{aligned} \tag{E.7}$$

and remark that the crossed Andreev reflection term vanishes. Linearizing the zero-temperature Fermi functions, we finally obtain the longitudinal differential conductance at energy E_{F}:

$$g_{\mathrm{LR}}(E_{\mathrm{F}}) = \frac{e^2}{h}\Big[g(E_{\mathrm{F}}) + g^{\mathrm{LAR}}(E_{\mathrm{F}})\Big]. \tag{E.8}$$

The time-periodic drive is taken into account by replacing the Nambu-Keldysh-Green's functions in Equation E.7 by the more general Floquet versions, and half-quantized conductance can be recovered by applying the same Floquet sum rule as in Equation 2.20. Lastly, we note that with appropriate modifications, the method discussed here can be applied to study SC-N-SC junctions, as was done in Ref.[268]. A key difference is that the extension to Nambu spinor description has to be performed already for the mixed Green's function, rather than for the sample Green's function, as is the case for N-SC-N junctions.

Appendix F

Tight-binding model for the nodal network semimetal Co_2MnGa

The tight-binding model of Co_2MnGa, a system hosting band-crossings in the forms of chains and links, used extensively in Chapter 5, was taken from Ref. [136]. Here we copy this tight-binding model for ease of reading. It consists of six bands: Three d-orbitals from Mn and three p-orbitals from Ga. In reciprocal space with the basis $(d_{xz}, d_{yz}, d_{xy}, p_x, p_y, p_z)$, it is given by:

$$H(\boldsymbol{k}) = \begin{pmatrix} \xi_1^d & 0 & 0 & \xi_{11}^{dp} & 0 & \xi_{13}^{dp} \\ 0 & \xi_2^d & 0 & 0 & \xi_{22}^{dp} & \xi_{23}^{dp} \\ 0 & 0 & \xi_3^d & \xi_{31}^{dp} & \xi_{32}^{dp} & 0 \\ \xi_{11}^{dp} & 0 & \xi_{31}^{dp} & \xi_1^p & \xi_{12}^p & \xi_{31}^p \\ 0 & \xi_{22}^{dp} & \xi_{32}^{dp} & \xi_{12}^p & \xi_2^p & \xi_{23}^p \\ \xi_{13}^{dp} & \xi_{23}^{dp} & 0 & \xi_{31}^p & \xi_{23}^p & \xi_3^p \end{pmatrix} (\boldsymbol{k}), \tag{F.1}$$

with:

$$\begin{aligned}
\xi_1^d(\boldsymbol{k}) &= 4t_1 \cos\frac{k_x}{2}\cos\frac{k_z}{2} + 2t_2(\cos k_x + \cos k_z) + 2t_3\cos k_y + \epsilon_d \\
\xi_2^d(\boldsymbol{k}) &= 4t_1 \cos\frac{k_y}{2}\cos\frac{k_z}{2} + 2t_2(\cos k_y + \cos k_z) + 2t_3\cos k_x + \epsilon_d \\
\xi_3^d(\boldsymbol{k}) &= 4t_1 \cos\frac{k_x}{2}\cos\frac{k_y}{2} + 2t_2(\cos k_x + \cos k_y) + 2t_3\cos k_z + \epsilon_d \\
\xi_1^p(\boldsymbol{k}) &= 4t_4 \cos\frac{k_y}{2}\cos\frac{k_z}{2} + 2t_5(\cos k_y + \cos k_z) + 2t_6\cos k_x + \epsilon_p \\
\xi_2^p(\boldsymbol{k}) &= 4t_4 \cos\frac{k_x}{2}\cos\frac{k_z}{2} + 2t_5(\cos k_x + \cos k_z) + 2t_6\cos k_y + \epsilon_p \\
\xi_3^p(\boldsymbol{k}) &= 4t_4 \cos\frac{k_x}{2}\cos\frac{k_y}{2} + 2t_5(\cos k_x + \cos k_y) + 2t_6\cos k_z + \epsilon_p \\
\xi_{12}^p(\boldsymbol{k}) &= -4t_7 \sin\frac{k_x}{2}\sin\frac{k_y}{2} \\
\xi_{23}^p(\boldsymbol{k}) &= -4t_7 \sin\frac{k_y}{2}\sin\frac{k_z}{2} \\
\xi_{31}^p(\boldsymbol{k}) &= -4t_7 \sin\frac{k_x}{2}\sin\frac{k_z}{2} \\
\xi_{11}^{dp}(\boldsymbol{k}) &= \xi_{22}^{dp}(\boldsymbol{k}) = 2t_8 \sin\frac{k_z}{2} \\
\xi_{13}^{dp}(\boldsymbol{k}) &= \xi_{32}^{dp}(\boldsymbol{k}) = 2t_8 \sin\frac{k_x}{2} \\
\xi_{23}^{dp}(\boldsymbol{k}) &= \xi_{31}^{dp}(\boldsymbol{k}) = 2t_8 \sin\frac{k_y}{2}
\end{aligned} \tag{F.2}$$

where the fitted tight-binding parameters are given (in units of eV) by: $t_1 = -0.31$, $t_2 = -0.018$, $t_3 = -0.01$, $t_4 = 0.2$, $t_5 = -0.02$, $t_6 = 0.04$, $t_7 = 0.28$, $t_8 = -0.34$, $\epsilon_d = -0.6$, $\epsilon_p = 0.6$.

Appendix G

List of publications

1. Ching Hua Lee, Han Hoe Yap, Tommy Tai, Gang Xu, Xiao Zhang, Jiangbin Gong, *Enhanced higher harmonic generation from nodal topology*, arXiv:1906.11806.

2. Gaomin Tang, Han Hoe Yap, Jie Ren, Jian-Sheng Wang, *Anomalous near-field heat transfer in carbon-based nanostructures with edge states*, Phys. Rev. Applied 11, 031004 (2019).

3. Han Hoe Yap, Longwen Zhou, Ching Hua Lee, Jiangbin Gong, *Photoinduced half-integer quantized conductance plateaus in topological-insulator/superconductor heterostructures*, Phys. Rev. B 97, 165142 (2018).

4. Linhu Li, Han Hoe Yap, Miguel A. N. Araújo, and Jiangbin Gong, *Engineering topological phases with a three-dimensional nodal-loop semimetal*, Phys. Rev. B 96, 235424 (2017).

5. Patrick Haughian, Han Hoe Yap, Jiangbin Gong, and Thomas L. Schmidt, *Charge pumping in strongly coupled molecular quantum dots*, Phys. Rev. B 96, 195432 (2017).

6. Han Hoe Yap, Longwen Zhou, Jian-Sheng Wang and Jiangbin Gong, *Computational study of the two-terminal transport of Floquet quantum Hall insulators*, Phys. Rev. B 96, 165443 (2017).

7. Han Hoe Yap and Jian-Sheng Wang, *Radiative heat transfer as a Landauer-Büttiker problem*, Phys. Rev. E 95, 012126 (2017).